**Dissertation**

# The role of Si on the microstructure of Al casting alloys and short fibre composites

ausgeführt zum Zwecke der Erlangung des akademischen Grades eines Doktors der technischen Wissenschaften unter der Leitung von

o. Univ. Prof. Dr. H. Peter Degischer
E308
Institut für Werkstoffwissenschaft und Werkstofftechnologie, TU-Wien

Zweitbegutachter: Prof. Dr. Enrique Louis
Instituto Universitario de Materiales de Alicante, Alicante University

eingereicht an der Technischen Universität Wien
**Fakultät für Maschinenwesen und Betriebswissenschaften**

von

Dipl. Ing. Fernando Adrián Lasagni
Matr. Nr. 327184
Denglergasse 9/19
A-1150 Wien

Wien, Oktober 2006

Fernando A. Lasagni

a mi “*nonna*” Emma
to my grandmother Emma

## Acknowledgements

The present work was carried out at the Institute of Materials Science and Technology of the Vienna University of Technology in Austria, in collaboration with the Leichtmetallkompetenzzentrum (LKR) Ranshofen, Austria. The work was partially financed by the Austrian Non Kplus-programme and the ADEMAT-Network (EU-Alfa II Programme).

At first, I am very indebted with my supervisor, Prof. H. Peter Degischer, for giving me the opportunity of carrying out a doctoral thesis. The numerous stimulating discussions and his dedication make the road of developing a PhD thesis easier, always with a great sense of mood and never-ending energy.

A big thank goes to Peter Schulz and Maria Papakyriacou of LKR Ranshofen for providing the materials and continuous support, as well as Prof. Enrique Louis of the Alicante University (Spain) for acting as co-examiner of this work.

I am grateful to Prof. Mücklich and Andrés Lasagni of the Saarland University for assisting and performing the 3D-reconstruction of materials. A personal thank goes to my brother Andrés for his unconditional support, advices and enriching conversation about the simple life. *Gracias hermanito!* You are simply the best.

I would like to thank Dr. Bernhard Mingler of the Institute of Materials Physic (Vienna University) for performing TEM investigations and Dr. Myriam Dumont (TECSEN - Faculté des Sciences et Techniques de St-Jérôme, Marseille) for calorimetry measurements and modelling, and also for the enthusiastic discussions.

I want also to thank my colleagues and friends of the institute for their assistance and collaboration with the different tests performed in this thesis, and also for creating a very pleasant atmosphere. Thank you Warcho, Guillermo, Cecilia, Christian, Jana, Heidi, Hamid, Ahmad, Stephan, Thomas, Tanja and Silvia.

Last but not at least, I would like to express my deep gratitude to my parents and grandmother, Norberto, Renata and *nonna* Emma, for their love and for teaching me the most important science: the life. I owe and special thank to my sisters Renata and Viviana for their unconditional love and support (also for five wonderful nieces and nephew!). You all are always on my heart, although the long distance between us.

Finally, I would like to thank my beloved *Inma* for making my day by day better in all aspects. She is the one who had to lead with the stress after a long working day. Thank you for supporting and helping me every time, thank you for make me so happy. *Gracias mi amor*.

# Kurzfassung

Die thermomechanischen Eigenschaften von Al-Si Legierungen sind für deren Einsatz als Komponenten für Verbrennungsmotoren und Bremsen von Bedeutung. Diesbezügliche Verbesserungen sind gefragt, da die Anforderungsprofile stetig anspruchsvoller werden. Mit gesteigerter Präzision in der Fertigung erhält die Formstabilität der Werkstoffe erhöhte Aufmerksamkeit. Die neuen Untersuchungsmethoden zur dreidimensionalen Gefüge-Architektur heterogener Werkstoffe eröffnen weitere Entwicklungsmöglichkeiten sowohl der konventionellen Legierungen als auch der Metallmatrix-Verbundwerkstoffe.

Hierfür werden hier grundlegende Untersuchungen der Legierungen AlSi1.1, 1.7, 7, und 12 beschrieben, sowie der 20 vol% Saffil($\delta$-$Al_2O_3$)-kurzfaserverstärkten Matrixlegierungen AlSi1.1, 7, 12, und 18 (SFRM). Die thermische Ausdehnung dieser Legierungen und dieser SFRM nimmt mit zunehmendem Si-Gehalt ab. Die in den Proben in einer Ebene statistisch verteilt orientierten Kurzfasern reduzieren die thermische Ausdehnung besonders stark in der Faserebene. Senkrecht zur Faserorientierung steigt jedoch der physikalische, thermische Ausdehnungskoeffizient mit steigender Temperatur über den der unverstärkten Matrix.

Bis zu 1.6 % Si sind in Aluminium löslich, jedoch sinkt die Löslichkeit bis 300°C stark ab, sodass in lösungsgeglühten, abgeschreckten Proben Si-Ausscheidungen erzeugt werden können. Die Ausscheidungskinetik wird mittels Differential Scanning Calorimetry (DSC) untersucht und mit Ausdehnungseffekten, die dilatometrisch gemessen werden korreliert. Die Ausscheidung bewirkt einen zusätzlichen Expansionseffekt wegen der vom Al unterschiedlichen Kristallstruktur der Si-Ausscheidungen, während deren Auflösung zu einer Reduktion der thermischen Expansion führt. Plättchenförmige und globulare Si-Ausscheidungen wurden mittels Transmissionselektronenmikroskopie (TEM) identifiziert, die auf unterschiedliche Keimbildungsmechanismen zurückgeführt werden. Mit diesen Gefügekorrelationen kann die Dilatometrie zur Bestimmung der Ausscheidungskinetik herangezogen werden.

Um die Wirkung der eutektisch gebildeten Si-Strukturen zu studieren, wurde die dreidimensionale Anordnung und deren Stabilität an AlSi 7 und AlSi12 Legierungen mit und ohne Sr-Veredelung untersucht. Mittels Tiefätzung bzw. chemischer Auflösung der $\alpha$-Al-Phase wird gezeigt, dass die eutektischen Si-Strukturen im Gusszustand der Proben dreidimensional zusammenhängende Netzwerke bilden. Die Veredelung durch Sr verfeinert das eutektische Gefüge wesentlich und es sind korallenartige Strukturen erkennbar. Durch eine Lösungsglühung bei 540°C formen sich die Si-Strukturen ein und verlieren den dreidimensionalen Zusammenhang. Im Detail werden die Si-Strukturen mittels einer schichtweisen Abtragung mit einem Focussed Ion Beam (FIB) im Rasterelektronenmikroskop mit Details von einigen zehn nm dargestellt, wobei auch die elementspezifische Abbildung mittels energiedispersiver charakteristischer Röntgenstrahlung unterstützt wird (SEM-EDX).

In den kurzfaserverstärkten Materialien verbindet das eutektische Si die Kurzfasern und es bildet sich ein dreidimensionales Si-Kurzfaser-Netzwerk. Eine Lösungsglühung bewirkt auch in den SFRM eine Vergröberung der Si-Strukturen, aber diese bewirken weiterhin den Zusammenhalt der Kurzfaserverteilung. Mit steigendem Si-Gehalt nimmt auch der Elastizitätsmodul und die Druckfestigkeit bei erhöhter Temperatur zu. Die beobachtete Entfestigung ab Stauchungen von 4% wird auf Bruchvorgänge in der Verstärkungsstruktur zurückgeführt. Bei thermozyklischen Kriechversuchen zeigen die SFRM-Proben der übereutektischen AlSi18-Matrix eine doppelt so hohe Lebensdauer wie die eutektische und die untereutektische Matrix. Die Lebensdauer sinkt nach einer Lösungsglühung, dafür nimmt die Duktilität deutlich zu. Die Si-Ausscheidungsvorgänge werden auch in den SFRM beobachtet und die Art der Vernetzung der Kurzfasern durch das eutektische Si beeinflusst die mechanischen Kennwerte.

## Abstract

Thermal stability and the improvement of the mechanical properties of Al-Si alloys and their composites are important for their application in engine and break components. The study of the three-dimensional microstructure of the materials would be a significant tool for further alloy and composite development by understanding the influence of the 3D architecture of their heterogeneities.

In this work the thermal expansion of different AlSi1.1, -1.7, -7, -12 alloys and reinforced AlSi1.1, 7, 12, 18 alloys with 20%vol. of $Al_2O_3$-short fibres is investigated. A reduction of the thermal expansion is observed by increasing the Si content in both unreinforced and reinforced Al-Si alloys. The addition of random planar alumina fibres reduces the in plane thermal expansion, but the transverse expansion is significantly increased with respect to the matrix. The precipitation kinetics of Si is studied by means of Differential Scanning Calorimetry (DSC). The measured exothermic and endothermic effects produced by the precipitation and dissolution of Si are correlated with an increase and reduction of the coefficient of thermal expansion (CTE), respectively. The results provide a method to use dilatometry for studies of precipitation kinetics of Si in aluminium.

A detailed study of the 3D morphology of different eutectic architectures of unmodified and Sr-modified AlSi7-12 alloys and composite materials is been conducted, Scanning Electron Imaging (SEI) of deep etched samples and a new Focused Ion Beam – Energy Dispersive Spectroscopy (FIB-EDX) method are applied. The 3D structures of the silicon phases can be reconstructed on sub-µm scale.

Al-Si alloys, with 7% and higher content of Si, present a percolating Si-network in the as cast condition. The addition of Strontium produces morphological changes of the network from lamellar Si to a fine dispersed coral fibrous like architecture. Spheroidisation and coarsening of the eutectic Si architecture is studied after different exposure times at 540°C. The disintegration of the eutectic Si network in AlSi foundry alloys by the solution treatment is in contrast to the stabilization of the Si short fibre network in the SFRMs.

The addition of alumina fibres into the Al-Si matrices has avoided the disintegration of the Si-structure by forming an $Al_2O_3$-Si-network. During solution treatment, Si diffuses from fibre free-zones to the fibre surface by forming coarse Si particles.

Both, elastic modulus and maximum strength (from compression tests) show the improvement of the properties by increasing the Si content. Strength vs. true strain curves of compression tests depict a softening in the composite materials starting at about 4% of strain (independent of the Si content), which is related to the fracture of the alumina fibre network.

Thermal cycling tests depict an increment of the cycling life of composite by the hypereutectic addition of Si by a factor of ~2 comparing the AlSi18/$Al_2O_3$/20s composite with AlSi7/$Al_2O_3$/20s or AlSi12/$Al_2O_3$/20s materials. The ductility of materials is increased during solution treatment but with a considerable reduction in the number of cycles of thermal cycling creep tests.

# Index

# Chapter 1
# Objectives

Al-based alloys are used widely due to their light weight and high strength, compared with pure-Al. Aluminium Metal Matrix Composites (MMC) are considered attractive choices for use in automotive engines because of the advantageous mechanical properties at elevated temperatures, such as enhanced specific strength and stiffness provided by the ceramic reinforcement and some ductility by the Al-alloys [Kelly, 2000; Requena, 2006; Schnabl, 2003]. These materials are finding steadily more applications in the aerospace and defence industries. In many of these applications, resistance to elevated temperature must be enhanced. The coefficient of thermal expansion (CTE) is one of the important thermo-mechanical properties. The dimensional stability can be a critical issue for the service lifetime of engine components that are exposed to thermal cycling like pistons [Henning, 1994; Zhang, 2003].

Thermal treatments of age hardening alloys like Al-Si containing Mg and/or Cu, are to improve the mechanical properties appropriate for the final application. During solution treatment, the as-cast microstructure is reheated to below the eutectic temperature for an appropriately termed time. This process is followed by water quenching to maintain supersaturation, and can be followed by an ageing treatment at moderate temperature to produce a high density of small precipitates, increasing the hardness of the alloy [Edwards, 1998; Mori, 2006; Zeren, 2005; Bekheet, 2002]. The Al-Si binary system is designated as non age-hardening. The main reason for a solution treatment is not to dissolve the Si phase, the solubility of which is only 1.6 wt.% at the eutectic temperature (1.2 wt.% at 540°C). Actually, the solution treatment of alloys containing more than 2 wt.% Si is a spheroidization treatment of the eutecticly segregated Si, the main objective of which is to improve the ductility of the eutectic material. After solution treatment, dimensional stabilization becomes important for hot parts in Al-engines, where local dimensional changes during exposure time would induce additional stresses.

The understanding of the three-dimensional architecture of eutectic alloys and short fibre reinforced composite materials is a key for the improvement of the mechanical properties of materials [Vidal-Sétif, 1999]. Therefore, intensive work has been done in order to investigate the effect of Si spheroidization on microstructure and mechanical properties in Al-Si alloys, but mainly in 2D.

The present doctoral thesis presents a detailed description of the topics listed bellow:

- Precipitation Kinetics of Si
- Thermal stability of the Al-Si system and dependence on thermal condition
- Influence of above topics on Short Fibre Reinforced Materials (SFRM).
- Morphological evolution of eutectic Si in Al-Si alloys and in SFRM.
- Indication of the influence of above features on mechanical properties at elevated temperatures.

# Chapter 2
# Background

## 2.1 Aluminium Alloys

### 2.1.1 Aluminium, General Introduction

Aluminium, the second most plentiful metallic element on earth, became an economic competitor in engineering applications during the first halve of the 20th century. It was to become a metal for its time. The emergence of three important industrial developments would, by demanding material characteristics consistent with the unique qualities of aluminium and its alloys, greatly benefit growth in the production and use of the new metal.

When the electrolytic reduction of alumina ($Al_2O_3$) dissolved in molten cryolite was independently developed by Charles Hall in Ohio and Paul Heroult in France in 1886 [World Aluminium, 2000], the first internal combustion-engine-powered vehicles were appearing, and aluminium would play a role as an automotive material of increasing engineering value. Electrification would require immense quantities of lightweight conductive metal for long-distance transmission and for construction of the towers needed to support the overhead network of cables which deliver electrical energy from sites of power generation. Within a few decades the Wright brothers gave birth to an entirely new industry which grew in partnership with the aluminium industry development of structural reliable, strong, and fracture-resistant parts for airframes, engines, and ultimately, for missile bodies, fuel cells, and satellite components.

The Aluminium industry's growth was not limited to these developments. The first commercial applications of aluminium were novelty items such as mirror frames, house numbers, and serving trays. Cooking utensils were also a major early market. In time, aluminium grew in diversity of applications to the extent that virtually every aspect of modern life would be directly or indirectly affected by its use.

### 2.1.2 Aluminium Production

All aluminium production is based on the Hall-Héroult process. Alumina refined from bauxite is dissolved in a cryolite bath with various fluoride salt additions made to control bath temperature, density, resistivity, and alumina solubility. An electrical current is then passed trough the bath to electrolyse the dissolved alumina with oxygen forming at and reacting with the carbon anode, and aluminium collecting as a metal pad at the cathode. The separated metal is periodically removed by siphon or vacuum methods into crucibles, which are then transferred to casting facilities where remelt or fabricating ingots are produced.

The major impurities of smelted aluminium are iron and silicon, but gallium, titanium and vanadium are typically present as minor contaminants. Internationally, minimum aluminium purity is the primary criterion for defining composition and value. In the United States, a convention for considering the relative concentrations of iron and silicon as the more important criteria has evolved. Reference to grades of unalloyed metal may therefore be by purity alone, for example, 99,70% Al, or by the method sanctioned by the Aluminium Association in which standardized Pxxx grades have been established. In the later case, the digits following the letter P refer to the maximum decimal percentages of Si and Fe, respectively. For example, P1020 is unalloyed smelter-produced metal containing no more than 0.10% Si and no more than 0.20% Fe [Davis, 1993]. Common P grades range from P0202 to P1535, each of which incorporates additional impurity limits for control purposes.

Refining steps are available to attain much higher levels of purity. Purities of 99.99% are achieved through fractional crystallization or Hoopes cell operation. Combinations of these purification techniques result in 99.9999% purity for highly specialized applications.

### 2.1.3 Alloying

It is convenient to divide aluminium alloys into two major categories: casting compositions and wrought compositions. A further differentiation for each category is based on the primary mechanism of property development (heat treatable and non-heat treatable alloys).

Cast and Wrought alloy nomenclatures have been developed [Davis, 1993]. The Aluminium Association system is most widely recognized in the United States [Al association, 1990]. Their alloy identification system employs different nomenclatures for wrought and cast alloys, but divides alloys into families for simplification. For *wrought alloys* a four-digit system is used to produce a list of wrought composition families as follows:

- *1xxx* Controlled unalloyed (pure) composition used primarily in the electrical and chemical industries.
- *2xxx* Alloys in which copper is the principal alloying element, through other elements, notably magnesium, may be specified. 2xxx series alloys are widely used in aircrafts.
- *3xxx* Alloys in which manganese is the principal alloying element. Used as a general-purpose alloy for architectural applications and various products (cans).
- *4xxx* Alloys in which silicon is the principal alloying element. Used in welding rods and brazing sheets.
- *5xxx* Alloys in which magnesium is the principal alloying element. Used in automotive interiors, boat hulls, gangplanks, and other products exposed to marine environments.
- *6xxx* Alloys in which magnesium and silicon are principal alloying elements. Commonly used for car body and architectural extrusions.
- *7xxx* Alloys in which zinc + magnesium are the principal alloying elements, but other elements such as copper, chromium, and zirconium may be specified. Used in aircraft structural components and other high-strength applications.
- *8xxx* Alloys including lithium and some tin compositions, characterizing miscellaneous compositions.
- *9xxx* Reserved for future use.

*Casting compositions* are described by a three digits system followed by a decimal value. The decimal .0 in all cases pertains to casting alloy limits. Decimals .1, and .2 concern ingot compositions, which after melting and processing should result in chemistries conforming to casting specification requirements. Alloy families for casting compositions are:

- *1xx.x* Controlled unalloyed (pure) compositions, especially for rotor manufacture.
- *2xx.x* Alloys in which copper is the principal alloying element, but other alloying elements may be specified.
- *3xx.x* Alloys in which silicon is the principal alloying element, but the other alloying age hardening elements such as copper and magnesium are specified. The 3xx.x series comprises the majority of all shape castings produced.
- *4xx.x* Alloys in which silicon is the principal alloying element.
- *5xx.x* Alloys in which magnesium is the principal alloying element.
- *6xx.x* Unused.
- *7xx.x* Alloys in which zinc is the principal alloying element, but other alloying elements such as copper and magnesium may be specified.
- *8xx.x* Alloys in which tin is the principal alloying element.
- *9xx.x* Unused

### 2.1.4 Strengthening Mechanisms

The predominant objective in the design of aluminium alloys is to increase strength, resistance to wear, creep and fatigue. Effects on these properties are specific to the different combinations of alloying elements, their alloy phase diagrams, and to the microstructures of solidification, thermomechanical history, heat treatment and/or cold working. These factors, to a large extent, depend on whether the alloy is a non-heat-treatable alloy or heat-treatable (precipitation strengthening) alloy.

Strength at elevated temperatures is improved mainly by solid-solution and second-phase hardening because at least for temperatures exceeding those of the precipitation-hardening range (>230°C), the precipitation reactions continue into the softening regime. For supersonic aircraft and space vehicle applications subject to aerodynamic heating, the heat-treatable alloys of the 2xxx group can be used only for temperatures up to 150°C.

### *Non-Heat-Treatable Alloys*

Strengthening in non-heat-treatable alloys occurs from solid-solution formation, second-phase microstructural constituents (eutectic segregates and/or dispersoids), precipitates, and/or strain hardening. Wrought alloys of this type are mainly those of the 3xxx and 5xxx groups containing Mg, Mn and/or Cr as well as the 1xxx aluminium and some alloys of the 4xxx group that contain only Si. Non-heat-treatable casting alloys are of the 4xx.x or 5xx.x groups, containing only Si or only Mg, respectively, and the 1xx.x aluminium.

- *Solid-Solution Strengthening:* For those elements that form solid solutions, the strengthening effect when the element is in solution tends to increase with increasing difference in the atomic radii of the solvent (Al) and solute (alloying element) atoms, but has to be less than 15% to be able to assume substitutional lattice positions. There are no interstitial hardening elements for Al.
- *Strengthening from Second-Phase Constituents:* Elements and combinations that form predominantly second-phase constituents with relatively low solubility at high temperature include Fe, Ni, Ti, Mn, Cr and Zr, and combinations thereof and with Si. The segregation of small volume fractions of the intermetallic-compound phases formed by these elements during solidification or by precipitation in the solid state during homogenisation and solution treatment also increase strength and hardness by hindering dislocation movement even at elevated temperature. These dispersoids yield as well some grain refinement. These aluminides do not cause appreciable precipitation hardening, nor is it intended. Their purpose is to produce finely dispersed particles (<1µm) that retard or inhibit grain growth in the alloy during hot working of wrought alloys.
- *Strain hardening:* by cold rolling, drawing, or stretching is an effective means of increasing the strength of all types of alloys, by increasing the dislocation density. This increase is obtained at the expense of ductility.

### *Heat-Treatable Alloys*

Heat treatable (precipitation hardening) Al-alloys for wrought and cast products contain elements that decrease in solubility with decreasing temperature, but their concentrations can exceed their equilibrium solid solubility at room temperature and moderately higher temperatures. The strengths of most binary alloys containing Mg, Si, Zn or Mn alone exhibit little change if precipitated.

The mechanism of strengthening by age hardening involves the formation of small (<0.1µm) at least partially coherent crystals containing the precipitating atoms. These cause a great deal of interfacial strain because of the mismatch in the lattice parameters. Such 3D strain fields pin dislocations, because the interaction of the correlated strain fields causes either attraction or repulsion of dislocations reducing the strain energy, similar to the reduction in strain energy of a single solute moving to a dislocation but owing to the 3D extension of precipitates with significantly higher interactive forces. When dislocations are pinned or trapped by a high density of precipitates, the yield strength of the alloy is considerably increased as well as the hardness.

Heat treatment for precipitation strengthening includes a solution treatment at a high temperature to maximize the solubility, followed by rapid cooling or quenching to a low temperature to obtain a solid solution supersaturated with both solute elements and vacancies.

- *Natural aging* refers to spontaneous formation of coherent clusters of solute atoms (GP-zones) during exposure at room temperature. Atom cluster enriched in solute atoms segregate either in 3D morphology along selected lattice planes, depending on the alloy system. Diffusion at room temperature is enhanced by the vacancy supersaturation which fades out with time. Al-Cu-alloys exhibit strong natural aging after being solution-heat-treated and quenched. AlMgSi as well as AlZnMg alloys show this effect.
- *Artificial aging* includes exposure at temperatures above room temperature so as to produce the transitional forms of metastable precipitates of a particular alloy system. These transitional particles remain fully or partially coherent with the solid-solution matrix and thus contribute to precipitation strengthening. With further heating or higher temperatures the precipitated particles coarsen, but even more importantly increase the inter-particle distances and they convert into the equilibrium phases, which generally are not coherent. These changes soften the material (over-ageing) and, carried further, produce an annealed condition.

The commercial heat-treatable aluminium alloys are, with the exception of the Al-Cu system, based on ternary or quaternary systems with respect to the solutes involved in developing strength by precipitation. The most prominent systems are: Al-Mg-Si (6xxx wrought alloys); Al-Si-Mg, Al-Si-Mg-Cu (3xx.x casting alloys); Al-Zn-Mg and Al-Zn-Mg-Cu (7xxx wrought and 7xx.x casting alloys); Al-Si-Cu (3xx.x) and Al-Cu-Mg-Si, alloys of the 2xxx and 2xx.x groups (wrought and casting alloys, respectively).

### 2.1.5 Cast-alloys based on the aluminium-silicon system

Alloys with silicon as the major alloying addition (>4at.%) are the most important of the aluminium casting alloys mainly because of the high fluidity imparted by the presence of relatively large volumes of the Al-Si eutectic. Other advantages of these castings are high resistance to corrosion, good weldability and the fact that the silicon phase reduces both shrinkage during solidification and the coefficient of thermal expansion of the cast products. Si increases the hardness and wear resistance. However, machining may present difficulties because of the presence of hard silicon particles in the microstructure. Commercial alloys are available with hypoeutectic and, less commonly, hypereutectic compositions.

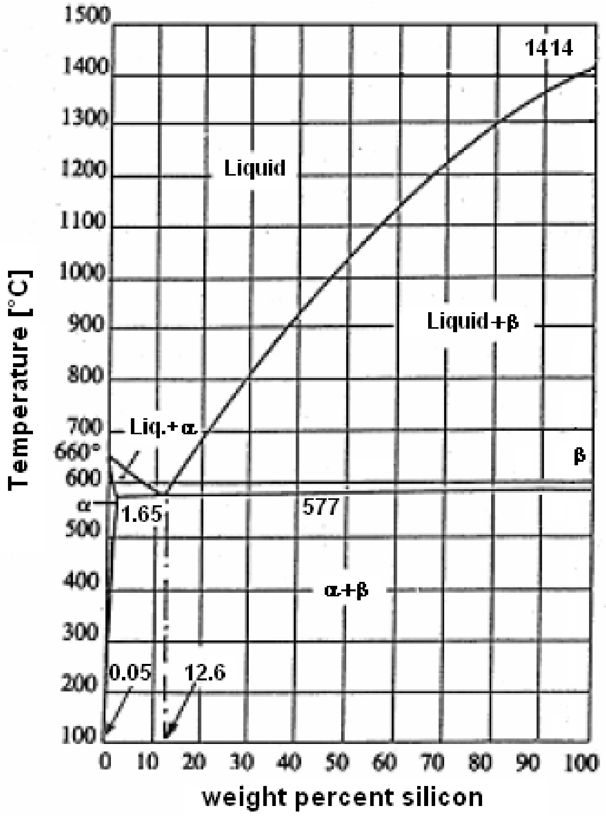

**Figure 2.1.** The Al-Si phase diagram [Smithells, 1983],

β = essentially pure Si.

The eutectic is formed between an aluminium solid solution containing just 1.65wt% silicon (at the eutectic temperature ~577°C) and virtually pure silicon as the second phase (Figure 2.1). The eutectic composition has been a matter of debate but it is now generally accepted as being close to Al-12.6wt:% [Thermocalc, 2004]. Slow solidification of pure Al-Si alloys produces a very coarse microstructure in which the eutectic comprises large plates of silicon in a continuous $\alpha$ solid solution matrix. Alloys having this coarse eutectic exhibit low ductility because of the brittle nature of the large silicon plates. Rapid cooling, as occurs during pressure die or permanent mould casting, greatly refines the microstructure and the silicon phase assumes a fibrous form with the result that both ductility and tensile strength are much improved. The eutectic can also be refined by the process known as modification.

### 2.1.6 Silicon modification

The widespread use of Al-Si alloys for other types of castings derives from the discovery by Pacz in 1920 that a refinement or modification of the eutectic microstructure, similar to that achieved by rapid cooling, occurred when certain alkali fluorides were added to the melt prior to pouring [Pacz, 1921; Makhlouf, 2001].

Mechanical properties may be substantially improved due to the refinement of the microstructure [García-Hinojosa, 2003; Haque, 1995; Ogris, 2002a] and to the change of planar interfaces during solidification which minimizes porosity in the casting. Fracture toughness is also significantly raised [Thall, 1950].

Modification of Al-Si alloys is commonly achieved by the addition of sodium salts or small quantities (0.005-0.015%) of metallic sodium to the melt although the actual amount of sodium needed may be as little as 0.001% [Polmear, 1995]. The use of sodium presents casting problems such as reduced fluidity, but its major disadvantage arises through the rapid loss of the element by evaporation or oxidation. It is therefore necessary to add an excess amount and difficulties in controlling the content in the melt can lead to under- or over-modification of the final castings. Research has, therefore, been directed at replacing sodium and considerable commercial success has been achieved by modifying with strontium. The addition of 100-300ppm [Polmear, 1995; Dahle, 2005; Haque, 1995] of this element as an Al-Sr or Al-Si-Sr master alloys also produces a refined Al-Si-eutectic and tensile properties comparable with those obtained when sodium is used. Loss of strontium during melting is much less and, moreover, the modified microstructure is refined after remelting. Over-modification is also less of a problem with strontium since excess amounts of this element are taken into the compound $SrAl_3Si_3$ which has comparatively little effect on the size of the silicon particles in the eutectic. Yet, another advantage of strontium is that it suppresses formation of primary silicon in hypereutectic alloys which should improve their ductility and toughness. Modification mainly operates by increasing the undercooling during casting.

### 2.1.7 Binary Al-Si alloys

Binary Al-Si alloys up to the eutectic composition retain good levels of ductility, providing the iron content is controlled to minimize formation of large, brittle plates of the compound $\beta$-AlFeSi. In this regard, additions of manganese have been found to be beneficial because this element favours the eutectic formation of the finer $\alpha$-AlFeSi phase which has so-called Chinese script morphology. If the silicon content is below 8%, modification is not necessary to achieve acceptable levels of ductility because the primary $\alpha$-phase is present in relatively large amounts. The eutectic composition, which has a high degree of fluidity and low shrinkage on solidification, has particular application for thin-walled castings. As a class, the alloys are used for sand and permanent mould castings for which strength is not a prime consideration, e.g. domestic cookware, pump castings and certain automobile castings, including water-cooled manifolds.

When as-cast alloys containing substantial amounts of supersaturated silicon are subjected to elevated temperatures they suffer expansion due to the precipitation of Si from solid solution [Polmear, 1995]. Dimensional stability can be achieved by heating for several hours in the temperature range 200-500°C prior to subsequent machining or use, and tempers of the T5 or T7 types should be given to castings which are to be used at temperatures of 150°C or above [Polmear, 1995].

## 2.2 Metal Matrix Composites

### 2.2.1 General definitions

_Composite Material:_ A composite (or composite material) is defined as a material that consists of at least two constituents (distinct phases or combinations of phases) which are bonded together along the interface in the composite, each of which originates from a separate ingredient material which pre-exists the composite [mmc-asses, 2001].

The essential elements of this definition are:

1. composite refers to a material with properties like a continuum, as opposed to a structure or a component; as such a composite material is used for the fabrication of components of various shapes or functions, thus it should be distinguished from a wing or other structure made of several components bonded together, and from an electronic device or packaging structure made of layered materials (although one of the materials in the packaging could be a composite);
2. the composite is produced via a physical combination of at least two pre-existing ingredient materials; this distinguishes a composite from other multiphase materials which are produced by thermodynamic processes where one or more phases result from phase transformation: many "in-situ composites", such as directionally solidified eutectics or alloys from which a ceramic phase is precipitated, are thus considered to be alloys and not composites [Tjong, 2000] (even though their properties can be described using composite theory) .

Composites are classified by means of the type of matrix in which the second ingredient is embedded. The matrices of technological interest are polymeric, metallic and ceramic matrices. Thus, there are basically three different types of composites: *Metal Matrix Composites* (MMC), *Ceramic Matrix Composites* (CMC) and *Polymer matrix Composites* (PMC)

*Metal Matrix Composite (MMC):* a composite material in which one constituent is a metal or alloy forming at least one percolating network. The other constituent is embedded in this metal matrix and usually serves as reinforcement.

The reinforcement is characterised by its chemical composition and its properties as ingredient material, secondly by its shape and dimensions, its volume fraction and spatial distribution in the matrix, i.e. its architecture.

### 2.2.2 Types of MMC

There are two different classes of metal matrix composites [Degischer, 1997]:

1. Discontinuously reinforced matrix, where either particles, platelets (SiC, $Al_2O_3$, $B_4C$) or short fibres of high aspect ratio (usually $Al_2O_3$-$SiO_2$) or whiskers (e.g. SiC) are embedded within the alloys the strength of which contributes essentially to the composite properties. However, the use of whiskers as reinforcement has been forbidden in Europe due to their asbestosis like toxicity [Birchall, 1988; Ad. Comp. Mat., 1991]
2. Continuously reinforced metals, where either monofilaments of approximately 0.1mm in diameter (e.g. SiC) or multifilament tows of at least some hundreds of fibres of about 0.01mm in diameter (e.g. SiC, $Al_2O_3$, carbon) are embedded within a rather ductile matrix; framework like reinforcement structures or open pore sponges infiltrated by a metal create interpenetrating composites such components have to be manufactured by a net shape technique to preserve the continuous fibre.

There are two characteristic processing problems for such metal matrix composites:

1. The melt of the most metals does not wet the reinforcing ceramics. Therefore the two components have to be forced together (e.g. by pressure infiltration of molten metal into reinforcement performs, or by stirring discontinuous reinforcement into the melt, or by powder metallurgical compaction in solid state). The reactivity of certain melts with certain atmospheres in the perform can stimulate pressureless infiltration due to the chemical activity [Schiroky, 1997].
2. Secondly, metallic melts, especially of aluminium and magnesium, are highly reactive. As soon as bonding is achieved, care has to be taken to avoid chemical reaction between the matrix and the reinforcing phase, because the reaction products usually degrade the mechanical properties of the composite [Huang, 2005].

The orientation of the reinforcement within the matrix will determine the degree of anisotropy of the MMC. Particle Reinforced Metals (PRM) show normally the lowest anisotropy since the shape of the particle in generally spherical, irregular or platelet-like exhibiting a shape factor smaller than 5. However, depending on the production method and post processing route they can present a certain degree of alignment in the case of irregularly shaped particles (e.g. extruded materials). In the case of short fibre reinforced metals (SFRM), the reinforcement is usually produced as performs with the fibres randomly oriented in one plane. This means that the properties of the SFRM will normally show isotropy for directions oriented parallel to the plane of the fibres. Continuous fibre reinforced metals (CFRM) show a high degree of anisotropy for the undirectionally aligned fibres, but to counteract this effect (in case of need) it is possible to apply layers or weaves with different fibre orientation in one plane.

### 2.2.3 Processing Methods

The most commonly used methods of production of MMC can be divided in two groups:

1. Liquid phase processes.
2. Solid state processes.

#### 2.2.3.1 Liquid phase processing

Some characteristic problems have to be surpassed when producing a MMC using the metal matrix in the liquid state:

1. The melt of the metal usually does not wet the reinforcement. The two components have to be forced together in order to obtain a composite with embedded reinforcements. Bonding can be done by exerting a pressure on the melt or by shear forces when stirring the reinforcement (only discontinuous reinforcement) into the melt.
2. Most metals, which are used as matrix such as light metals, are highly reactive specially in the liquid state. As soon as bonding is achieved, care has to be taken to avoid chemical reaction between the matrix and the reinforcement since these products may degrade the mechanical properties of the composite.

Stir Casting:

This is the simplest process used for producing PRM. Here, a powder of ceramic particles is introduced into the molten matrix by stirring (see Figure 2.2). This can in principle be done with relatively conventional processing equipment. Due to the non-wettability between the ceramic and the metal, mixing of gas has to be prevented and only particles larger than 10µm can be introduced up to a volume fraction of about 20%. It is possible to carry out a continuous or semi-continuous production method and the obtained MMC ingots are suitable for further operations such as casting or extrusion. There are two major disadvantages in this process: the long period of molten matrix can result in interfacial reactions between matrix and reinforcement and microstructural inhomogeneity due to particle agglomeration, gas bubble entrapment and particle segregation due to differences in densities or/and as a result of particle pushing by an advancing solidification front [Degischer, 1998].

Commercially available PRM manufactured using this method have been successfully produced using aluminium and magnesium matrices [Alcan, 2003; Mortensen, 1993].

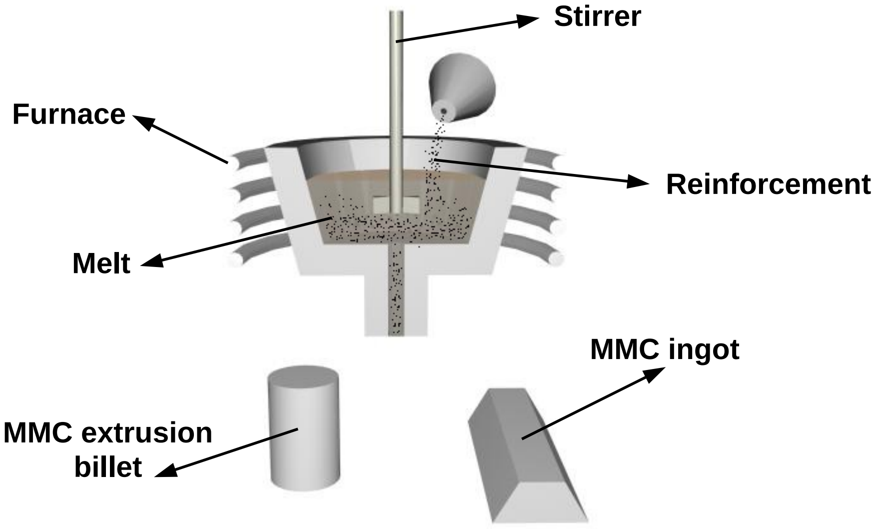

**Figure 2.2.** Schematic representation of the stir casting process.

<u>Infiltration Processes:</u>

In the case of infiltration techniques, the molten unreinforced matrix will infiltrate a ceramic perform of open porosity by means of pressure provided by a piston, gas, vacuum [Mortensen, 1993] or by use of capillarity forces [Pech-Canul, 2000; Carreño-Morelli, 1998] (pressureless infiltration). These methods are normally used for producing short fibres reinforced MMC and are quite common for producing continuously reinforced MMC [Carreño-Morelli, 1998; Nolte, 1997].

The main advantages of gas pressure or pressure-less infiltration techniques are [Mortensen, 1993]:

- No mechanical degradation of the reinforcement, which is an issue when producing composites having high volume fraction of reinforcement or featuring fragile reinforcements such as low volume fraction short fibre performs.
- The possibility of producing a net or near-net-shape material that is generally difficult to machine.
- The possibility of producing locally reinforced parts.

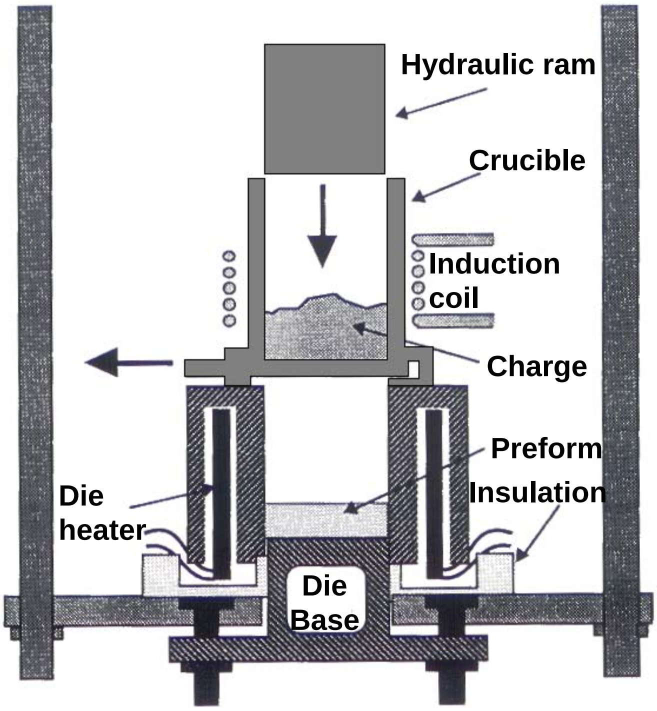

**Figure 2.3.** Schematic representation of the squeeze casting method [Clyne, 1993].

Although capillarity-driven infiltration may be attractive in some instances, pressure infiltration has some significant advantages for general engineering applications [Mortensen, 1993]:

- There are fewer restrictions on the chemistry of the matrix and the reinforcement.
- Pressure speeds infiltration significantly, allowing shorter process cycles and reducing chemical interaction of the matrix with reinforcement or die tooling.
- Applied pressure permits infiltration of performs with initial temperatures below the matrix liquidus, which can reduce further chemical interaction between matrix and reinforcement.

- Applied pressure practically eliminates the occurrence of uninfiltrated portions of the perform.
- If used together with properly designed cooling for directional solidification, applied pressure can drive matrix flow through the perform to avoid matrix solidification shrinkage.
- Applied pressure increases the rate of heat removal from the casting during solidification, in turn refining the matrix microstructure and reducing the time for fibre-matrix chemical reaction in the solid state.

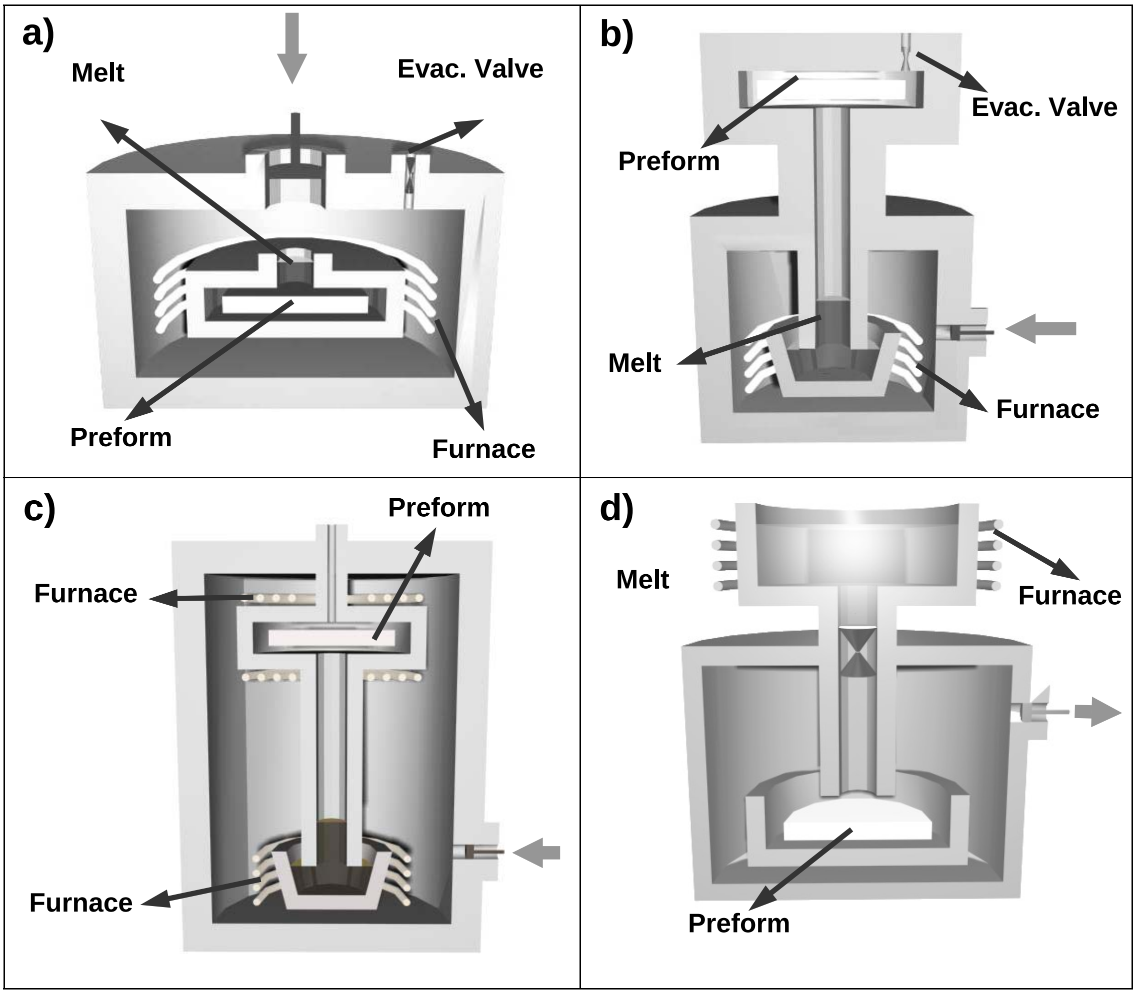

**Figure 2.4.** Four different experimental stups used for producing MMC by gas pressure infiltration (grey arrows represent the gas pressure inlet): a) the melt and the preform are both located in the autoclave during the infiltration, b) only the melt is in the autoclave and this is injected into the preform by means of applied pressure, c) both the melt and the preform are inside the autoclave but in different chambers before the infiltration process begins, d) the molten matrix is outside the autoclave and fed from above into the evacuated preform.

Among the piston-driven infiltration processes, squeeze casting is one of the main techniques used for the production of MMC [Mortensen, 1993; Clyne, 1993; Yue, 1996; Kaczmar, 2000; Henning, 1994]. Figure 2.3 shows schematically the equipment setup used for this process. The primary distinction between this method and conventional pressure die casting is that the ram continues moving during solidification, deforming the growing dendrite array and compensating for the freezing contraction (which is typically about 5%). In addition to this, the ram movement is usually slower, and the applied pressure often greater but rather hydrostatic, than is typical for die casting.

Several gas pressure infiltration devices have been designed [Mortensen, 1993; Carreño-Morelli, 1998]. Figure 2.4 shows four different experimental set-ups that have been used for producing MMC by using this method. The main disadvantages of these machines if compared to piston-driven ones is the lower available range of pressures, which implies that infiltration is slower and cooling rates are lower resulting in the higher probability of reaction between matrix and reinforcement and of remaining fine pores in the MMC. However, in gas-driven techniques there is no piston that must be separated from the matrix metal, and there is greater versatility in mould design in some configurations because the die can be immersed into the chamber containing pressurized gas. This makes the stress state of the die predominantly compressive, because the pressure outside the die is higher than that inside.

Spray Deposition:

Using the principles of rapid solidification, a variety of processing techniques have been developed and emerged as attractive and emerged as attractive and viable alternatives to optimise both the microstructure and properties of particle reinforced metal matrix composites [Srivatsan, 1995]. Here, a stream of metallic droplets impinges on a substrate in such a way as to build up a composite deposit. The reinforcement can be fed into the spray, if particulate, or introduced onto the substrate if fibrous. The first commercially available spray deposition technique and the most used was the Osprey$^{TM}$ method. The primary advantages of this technique are:

- The rapid formation of a range of semi-finished products such as tubes, billets or strips directly from the melt.
- Creation of composite materials which can contain up to and over 20vol% of the reinforcement by injection of particles smaller than 10µm into atomised stream of molten alloy.
- Potential for the economical manufacture of a spectrum of products as a direct consequence of the high rates of metal deposition that are available coupled with the concurrent elimination of several of the processing steps required in ingot metallurgy and powder metallurgy techniques.
- The facilitation of secondary processing routes without prolonged soaking times and/or the large deformation ratios required for fine grain-size, segregation-free microstructures.

However, secondary forming (i.e. extrusion, rolling, forging) is needed to reduce the inherent porosity from deposition.

*Thermal spraying* refers to another group of techniques used for production of MMC by spray deposition. This involves the feeding of powder, or in some cases wire, into the hot zone of a torch, where it is heated and accelerated as separate particles by the rapid expansion of a gas. The most common thermal spraying methods are plasma spraying and the use of High Velocity Oxy-Fuel (HVOF) guns [Clyne, 1993; Srivatsan, 1995]. Some porosity usually remains when these techniques are implemented.

#### 2.2.3.2 Solid state processing

The characteristic problems that arise during liquid state processing such as non-wetting between matrix and reinforcement and chemical reactions can be, in principle, avoided or diminished if the materials are processed in the solid state. In this case both of the components will remain in solid state during the whole production process and are bonded by diffusion.

Powder Metallurgy:

This process involves the sintering of a metallic powder (the matrix) and the ceramic fibres or particles [Poletti, 2003; Falahati, 2001]. The blending can be carried out dry or in liquid suspension. This is usually followed by cold compaction, canning, evacuation and a high temperature consolidation state such us HIPing or extrusion. The presence of fine oxide dispersoids coming from the precursor powders are very typical for Al based MMCs and these can affect remarkably the mechanical properties such as room and high temperature strength of these materials [Han, 1999; Zhigang, 2002; Mohamed, 1998]

Diffusion Bonding:

This is the mostly used technique for the production of MFRM. Here, arrays of filaments are placed between thin metallic foils or coated by the matrix and then hot pressed at high temperature. This method is attractive for the production of monofilament reinforced Ti matrix composites because: a) reinforcement of Ti with continuous fibres is particularly attractive (in view of the scope for significant improvements in creep resistance and stiffness), b) routes involving liquid Ti suffer from rapid interfacial chemical reaction and c) Ti is well suited for diffusion bonding operations since it dissolves its own oxide at temperatures above 700°C [Dudek, 1992]

## 2.3 Thermal effects and high temperature behaviour

### 2.3.1 Thermal expansion

Metals and alloys undergo dimensional changes in response to variations in temperature, a phenomenon that has critical implications for industries that process these materials at high temperatures. Solidification practices, such as casting or spray-forming, and hot working procedures in the solid state, such as forging, rolling or extrusion, can be significantly influenced by thermal stresses and strains that arise from temperature variations. If not properly controlled, these effects can have an adverse influence on product quality. Residual stresses and distortion can be introduced and in the worst cases crack-type defects can be formed. Hence the optimization of such processes calls for the use of sophisticated computer models that require comprehensive data on the thermal expansion characteristics of the material. The availability of data for the thermal expansion coefficient at elevated temperatures then becomes a key issue.

It is necessary to examine the alternative definitions of the thermal expansion coefficient, as the exact value can vary according to the definition employed, a fact that must be borne in mind by anyone wishing to employ such data.

#### 2.3.1.1 The coefficient of Thermal Expansion (CTE)

The expansion of any material with temperature can be quantified in terms of increasing linear dimension, such as the length of a specimen. In its simplest form, the *coefficient of linear thermal expansion* of any material can be defined as the fractional increase in length (linear dimension) per unit rise in temperature. The precise definition is slightly more complex with a number of alternatives as described below. The SI units of this quantity are $K^{-1}$ and typical values for metals and alloys are in the range $10\times10^{-6}$ to $30\times10^{-6}$ppm.$K^{-1}$. Ceramics normally have lower values in the range $1 \times 10^{-6}$ to $20 \times 10^{-6}$ppm.$K^{-1}$, and it is generally found that materials with higher melting temperatures have lower thermal expansion coefficients. An approximate rule of thumb for materials that melt above 600 ◦C is that they have a linear expansion of about 2% when heated from room temperature to their melting points [Touloukian, 1975].

It is important to note that the coefficient of thermal expansion (CTE) is a temperature-dependent property and will, for most metals and alloys, gradually increase with temperature. However in some instances the occurrence of phase changes will cause discontinuities in the value of the coefficient: for example a sharp contraction occurs on heating iron-based materials through the ferrite to austenite transition, as the crystal lattice changes from body-centred cubic to the more compact face-centred cubic structure.

Examination of the literature reveals a number of numerical formulae for calculating the thermal expansion coefficient. These can be grouped into two broad categories, depending on whether the expansion relates to a temperature range or a single temperature. Both of these have further subtle variations and the values of the coefficient can vary significantly according to the definition employed.

*Definition over a temperature range.*

Consider a sample of material with initial length $L_0$ at temperature $T_0$ which expands to $L_1$ at $T_1$, and then to $L_2$ at $T_2$ (Figure 2.5). The most general definition is the 'mean' or 'average' coefficient of expansion as given by ASTM [ASTM, 1995; ASTM, 1999; Kirby, 1992]:

$$\alpha_m = \frac{(L_2 - L_1)/L_0}{T_2 - T_1} = \frac{1}{L_0}\frac{\Delta L}{\Delta T} \qquad (2.1)$$

Here $\alpha_m$ is related to the slope of the chord between two points on the curve of length against temperature, and so represents the expansion over the particular temperature *range* from $T_1$ to $T_2$. Furthermore, the fractional increase in length is calculated by dividing the increase in length by the length at $T_0$. It is thus necessary to specify all three temperatures when quoting the value of $\alpha_m$. Usually $T_0$ is defined as a reference temperature such as 20°C.

Often the lower limit of the specified temperature range is also used as the reference temperature, leading to a modification of the equation to the following [Barron, 1998; Touloukian, 1975]:

$$\alpha_{m^*} = \frac{(L_2 - L_1)/L_1}{T_2 - T_1} = \frac{1}{L_1}\frac{\Delta L}{\Delta T} \qquad (2.2)$$

Sometimes tables are listed with pairs of values for $\alpha_{m^*}$ and temperature. This can lead to confusion if it is not made clear that the CTE refers to a temperature range and not to a single temperature.

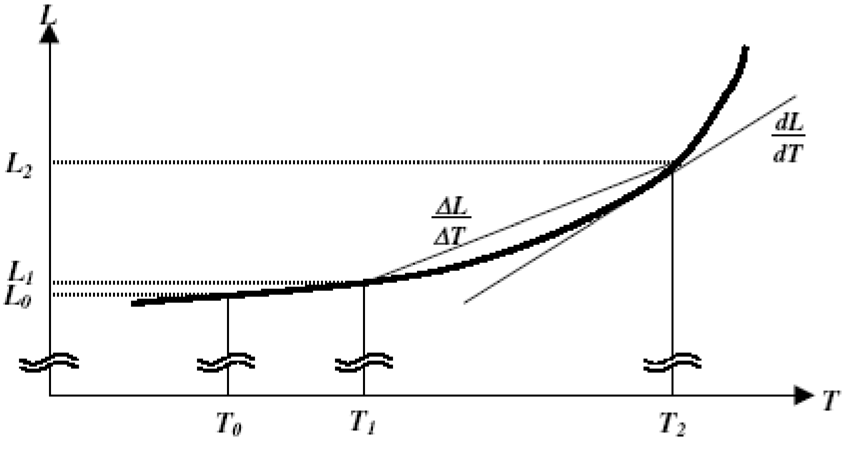

**Figure 2.5.** Change in length, L, of a sample of material as a function of temperature, T.

*Definition at a single temperature.*

In contrast to the previous definitions, the *instantaneous* coefficient of linear thermal expansion [6] (also referred to as *thermal expansivity* [ASTM, 1995]) is related to the derivative d*L*/d*T* at a single temperature. This is the slope of the tangent to the curve of length against temperature (Figure 2.5). The true coefficient can thus be defined as follows:

$$\alpha = \frac{dL/L_1}{dT} = \frac{1}{L}\frac{dL}{dT} \tag{2.3}$$

This is the limiting case of equation (2) as $T_1$ and $T_2$ become closer. It is a more fundamental definition than those described earlier, as only one temperature needs to be specified.

### 2.3.2 Thermal cycling in MMCs

Thermal stresses can affect the mechanical properties of MMCs, both in terms of yielding asymmetries and through changes in creep performance [Clyne, 1993]. These effects are in general relatively weak, primarly because thermal stresses often become reduced to low level by stress relaxation processes, particularly if these are allowed to operate over an extended period. However, if the temperature is repeatedly changed, then the thermal stresses are continuously regenerated, so that they can then exert a substantial influence on the mechanical performance. Before examining the mechanical behaviour of a composite material during thermal cycling, it is instructive to consider the effects of thermal cycling-induced internal stresses changes on a unloaded specimen.

A simple view [Rabinovitch, 1983] of the expected behaviour during thermal cycling is presented in Figure 2.6, which shows schematic changes in axial matrix stress and composite strain. Transverse stresses are neglected. The matrix is initially (point A) taken, Figure 2.6a, as having a residual tensile stress equal to the yield stress (because of cooling cycle). On the heating, this stress falls, becoming compressive and eventually causing yielding in compression (point B). A period of progressive plastic flow then follows. On cooling (from point C), the matrix yields in tension at point D, before returning to A. The dilatometry traces are predicted to show hysteresis, but no net dimensional change, if the residual stress after the thermal cycle is the same as the initial.

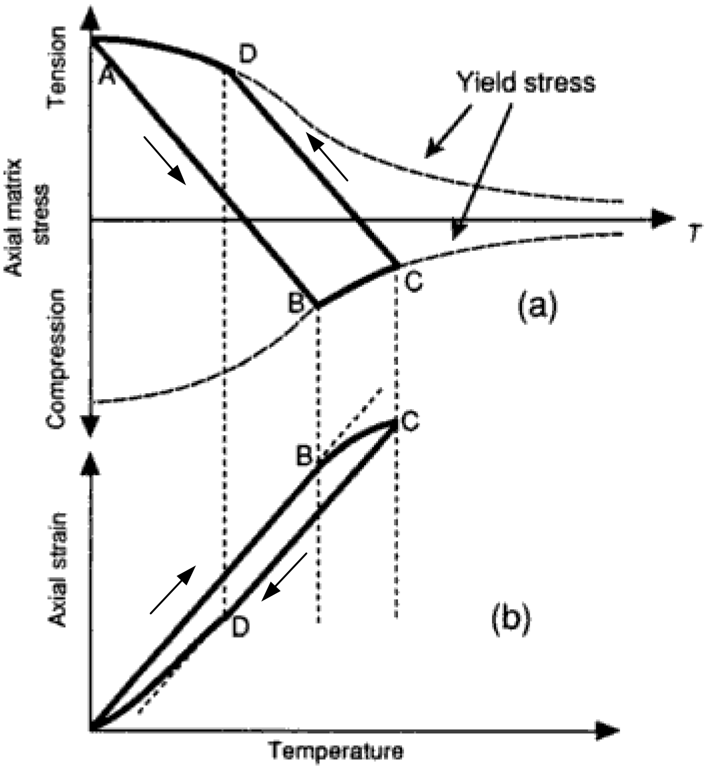

**Figure 2.6.** Schematic Illustration of the variation in a) matrix stress and b) specimen strain during thermal cycling of an aligned fibre composite

*Loaded thermal cycling*

Many researchers have observed [Furness, 1991; Le Flour, 1987; Wu, 1984; Hong, 1988; Pickard, 1988; Daehn, 1989] that the creep rates of discontinuous MMCs are substantially enhanced by thermally cycling the specimen while under an applied load. Two types of theoretical modes have been proposed:

- *Continuously or repeatedly deforming models* [Roberts, 1956; Anderson, 1962; Olsson, 1995] (also called enhanced plasticity models [Derby, 1991]) in which the thermal stresses combines with the applied load to exceed the material's yield stress, giving rise to a time-independent strain which is biased according to the sense of the applied load
- *Enhanced creep models* in which the internal stresses are not sufficient to cause matrix yielding, but aid conventional global time-dependent creep.

# Chapter 3

# Equations and basic models applied

## 3.1 Calculating the Coefficient of Thermal Expansion

Various macro- and micro-mechanical approaches have been proposed for obtaining the coefficient of thermal expansion of a composite, knowing the material constants of the components [Chawla, 1987].

Although a basic physical property, the CTE of a metal matrix composite is relatively difficult to predict, because the thermal behaviour of such a material is influenced by several parameters like the matrix yield strength, creep resistance, internal stress distribution and load transfer, phase changes and the architecture of the composite (e.g. particle size and shape, contiguity, porosity).

With appropriate thermo elastic models like the Schapery, or the Turner model, the CTE of a composite can be theoretically estimated assuming purely elastic conditions. The rule of mixtures considers independent expansion of the constituents.

### 3.1.1 Rule of Mixture (ROM)

Assuming a perfect composite, e.g. no voids, homogeneously distributed reinforcement, homogeneous matrix, no residual micro-stresses which normally appear as a consequence of the fabrication process, no elastic interactions between the constituents of a composite or the elastic properties of the constituents of the composite are equal [Hahn, 1991], the simplest description of the coefficient of thermal expansion of the composite are based on the analogy to the Voigt model. The model is based on springs connected in parallel series, and is often called “rule of mixture” (ROM) [Rammerstorfer, 2000].

According to a simple slab model of layers of two constituents, the resulting thermal expansion is the sum of the expansion of the components:

$$\alpha_C = f_I \alpha_I + f_M \alpha_M \tag{3.1}$$

where *f* is the volume fraction, and $\alpha$ the coefficient of thermal expansion of the component. The subscripts C, I, and M refer to the composite, inclusion (reinforcement) and matrix, respectively. $\alpha_C$ is thus the arithmetic mean of the coefficients of expansion of each phase, weighted by the volume fractions.

Since the composite is assumed to be free of voids, the following relation for a two-component composite is valid:

$$f_I + f_M = 1\text{, hence, } f_M = 1 - f_I \qquad (3.2)$$

Results of the linear ROM are in a good agreement with measurement results, for PRM only if the dimensional change of the matrix of the composite is stress-free, which requires discrete, isolated hard particles in a matrix with vanishing yield strength [Prohazka, 2001]. Isotropic plastic deformation would be admitted.

### 3.1.2 Schapery model

Bounds on effective thermal expansion coefficients of isotropic and anisotropic composite materials consisting of elastic phases are derived by employing extremum principles of thermoelasticity coupled with use of Hashin's bounds for the bulk composite modulus. It is assumed that the Poisson ratios of the components are not very different. Application is made to two-phase isotropic, particulate reinforced composites [Schapery, 1968].

$$\text{upper bound: } \alpha_C^{(+)} = \alpha_I + (\alpha_M - \alpha_I)\frac{\dfrac{1}{K_C^{(-)}} - \dfrac{1}{K_I}}{\dfrac{1}{K_M} - \dfrac{1}{K_I}} \qquad (3.3)$$

$$\text{lower bound: } \alpha_C^{(-)} = \alpha_I + (\alpha_M - \alpha_I)\frac{\dfrac{1}{K_C^{(+)}} - \dfrac{1}{K_I}}{\dfrac{1}{K_M} - \dfrac{1}{K_I}} \qquad (3.4)$$

Where *K* is the bulk modulus of the components of the composite. The bulk modulus is related to the Young's modulus *E* of isotropic materials by

$$K = \frac{E}{3(1-2\nu)} \qquad (3.5)$$

where $\nu$ is the Poisson's ratio.

Note that $\alpha_C$ depends on the volume fraction and phase geometry only through their effect on bulk modulus.

$K_C$ is the bulk modulus of the composite. However, only the upper and lower bounds of $K_C$ are known in a given case, corresponding to Hashin and Shtrikman's bounds [Hashin, 1963]. These bounds are given by:

$$\text{upper bound: } K_C^{(+)} = K_I + \frac{V_M}{\dfrac{1}{K_M - K_I} + \dfrac{3V_I}{3K_I - 4G_I}} \tag{3.6}$$

Hashin and Shtrikman's lower bound is calculated with the same formulae, after inversion of subscripts *I* and *M*:

$$\text{lower bound: } K_C^{(-)} = K_M + \frac{V_I}{\dfrac{1}{K_I - K_M} + \dfrac{3V_M}{3K_M - 4G_M}} \tag{3.7}$$

where *G* is the shear modulus, which is related to the Young's modulus *E* of isotropic materials by

$$G = \frac{E}{2(1+\nu)} \tag{3.8}$$

The upper bound on $K_C$ yields the lower bound of the composite CTE $\alpha_C^{(-)}$ shown in equation (3.3) and vice versa.

It is noteworthy that Hashin and Shtrikman's lower bound $K_C^{(-)}$ is an exact result for an elastic composite in which the reinforcement is a sphere coated with a uniform layer of the matrix. As already described above, the lower bound $K_C^{(-)}$ yields the upper bound of Schapery's model $\alpha_C^{(+)}$, thus should be closest to the actually occurring coefficient of expansion of a system having approximately spherical particles [Schapery, 1968]. The upper bound of Schapery's model $\alpha_C^{(+)}$ coincides with the CTE value determined from Kerner's model [Kerner, 1956].

In the presence of matrix plasticity, the composite is apparent CTE will deviate from the bounds derived in Schapery's analysis of elastic composites [Elomari, 1997].

### 3.1.3 Turner model

A simpler model that is often used is the Turner model. The model assumes homogeneous strain throughout the composite, and that only uniform hydrostatic stresses exist in the phase. The stresses are assumed insufficient to disrupt the composite. It is assumed that each component in the composite, which is constrained to change dimensions with temperature, changes at the same rate as the composite and the shear deformation is negligible [Hahn, 1991]. Using a balance of internal average stresses, Turner derived the coefficient of thermal expansion of a two-component composite as follows [Turner, 1946]:

$$\alpha_C = \frac{\alpha_I V_I K_I + \alpha_M V_M K_M}{\mathrm{V_I} K_I + V_M K_M} \tag{3.9}$$

This expression falls below Schapery's lower bound for the CTE of elastic composites.

Especially, composites with three-dimensionally continuous reinforcements and matrix phases should be well described by the Turner model, because it is expected that they approach the assumption of the same dimension change in the average (expansion and shrinkage, respectively) of each component of the composite in comparison with the composite itself [Prohazka, 2001]. If the phase with the small CTE is 3D percolating the resulting stresses may increase unrealistically high. For UD fibre reinforced metals it holds for the fibre direction.

## 3.2 Si precipitation

### 3.2.1 Introduction

During the processing of most age hardening aluminium alloys, non-isothermal precipitation plays a key role. It can be encountered during the early processing of the material, when considering the precipitation of dispersoids during homogenization [Robson, 2001] or hot rolling. Precipitation during a non-ideal quench is an issue when considering thick plate applications [Deschamps, 1998]. During the heating ramp multi-step heat treatments, dissolution of metastable phases can occur concurrent with precipitation of more stable phases [Gomiero, 1994].

Non-isothermal precipitation differs in a number of ways from the classically studied isothermal precipitation reactions [Nicolas, 2003]:

1. During the temperature treatments, all parameters of the precipitation process, namely diffusion, driving force and nucleation barriers, evolve simultaneously. Thus, precipitates that nucleate at a given time may be destabilised at the next time step, for instance.
2. Most precipitation hardening aluminium alloys precipitate through a sequence of several metastable phases. A non-isothermal temperature history may activate the precipitation of several of these phases in a complex manner.

### 3.2.2 Thermodynamic equations

The implemented model is based on the classical laws of precipitate evolution [Wagner, 1991] and its originality lies in the fact that these laws have been applied to each size class of the particle distribution. The model has been implemented for 7xxx series in the same way as described by Nicolas et al [Nicolas, 2003].

Basic equations

*a) Nucleation law*

A classical nucleation law including an incubation time was introduced given the nucleation

$$\text{rate:} \left.\frac{dN}{dt}\right|_{\text{nucleation}} = N_o Z\beta^* \exp\left(-\frac{\Delta G^*}{kT}\right)\exp\left(-\frac{\tau}{t}\right) \qquad (3.10)$$

where:

$N_0$ is the number of nucleation sites, $Z$ is the Zeldovich factor (here 0.05), $\beta^* = \frac{4\pi r^{*2} D\overline{C}}{a^4}$, $r^*$ is the critical radius, $D$ the diffusion coefficient, a the lattice parameter

$\Delta G^* = \frac{\Delta G_{o,nuc}}{\ln^2\left(C(r^*)/C_\infty\right)}$, $\Delta G_0$ is a fitting parameter, $\tau = \frac{1}{2\beta^* Z}$.

*b) Growth/dissolution kinetics*

The model is based on a classical law governing both dissolution and growth:

$$\nu = \frac{dr}{dt} = \frac{\overline{C} - C_i(r)}{C_p - C_i(r)} \frac{D}{r} \qquad (3.11)$$

where,

*r* is the radius at time *t*,

$\overline{C}$ is the mean solute concentration in the matrix (at%),

*$C_i(r)$* is the solute concentration at the particle/matrix interface (at%),

*$C_p$* is the solute concentration of the precipitate (at%),

*D* is the volume diffusion coefficient in the matrix ($m^2.s^{-1}$).

The interfacial concentration *$C_i(r)$* is the solute concentration at the particle/matrix interface. In the case of a diffusion-controlled process, *$C_i(r)$* can be approximated by the equilibrium concentration of the matrix in presence of a particle of radius r at the considered temperature. In the case of a binary alloy, the temperature determines this equilibrium concentration, using the Gibbs-Thompson equation to consider the radius dependence:

$$C_i(r) = C_i^{\infty} \exp\left(\frac{2\sigma V_m}{rRTC_p}\right) \qquad (3.12)$$

where

$C_i^{\infty}$ is the equilibrium concentration of solute across a planar interface (at%) (given by the phase diagram),

*σ* is the particle/matrix interfacial energy ($J.m^{-2}$),

*$V_m$* is the molar volume of the Si precipitates ($m^3.mol^{-1}$),

*$C_p$* is the atomic fraction of solute in the precipitate,

*T* is the absolute temperature (K),

*R* is the universal gas constant (8.314 $J.K^{-1}.mol^{-1}$).

*Parameters*

Many parameters have to be estimated. Note that it is very difficult to fit them on non-isothermal experiments, considering that many of them are temperature-dependent. As a consequence, fitted parameters are very unsatisfying regarding literature values. This work has to be continued.

| Diffusion | Interfacial energy | $C_\infty$ | $N_0$ |
|---|---|---|---|
| $D_{0,Si} = 1\times10^{-5}\ m^2.s^{-1}$<br>$Q_{diffSi} = 160.460$ KJ/mol | $\sigma = 0.4 J/m^2$ | $C_\infty = C_{exp}(-\Delta H/RT)$<br>$\Delta H = 62000$ J/mol<br>$C_{exp} = 60.16$at.% | $6\times10^5$ |

**Table 3.1.** Literature parameters for modelling of Si precipitation

### 3.2.3 Calculating the Percent Length Change and CTE in AlSi-alloys

The percent length change in Al-Si-alloys can be estimated from the modelled volume fraction following the subsequent treatment:

The length change in Al-Si-alloys could be principally subdivided as the contribution of three different effects: the expansion of a) Al and b) Si can be treated like in a composite material by the addition of both effects multiplied by their atomic fractions. Another important effect is the additional linear change produced by the c) precipitation of Si from a substitional Al-Si fcc cell into diamond structure. Therefore, the linear change ($\Delta l_{AlSi}$) of an AlSi-alloy can be written as:

$$\Delta l_{AlSi}(T) = f_{Al}\Delta l_{Al}(T) + f_{Si}\Delta l_{Si}(T) + \Delta l_{prec}(T) \qquad (3.13)$$

where:

$\Delta l_{Al}$ and $\Delta l_{Si}$ are the length changes of pure-Al and Si, respectively

$\Delta l_{prec}$ represents the corresponding length change due to the precipitation of Si

$f_{Al}$ and $f_{Si}$ are the aluminium and silicon volume fractions in the alloy, respectively.

Si dissolves in an fcc Al-cell during solution treatment which has an atomic volume of $6.60\times10^{-23}cm^3/at$. Si precipitates by forming a diamond structure with an atomic volume 21.4% higher ($8.01\times10^{-23}cm^3/at$) than in fcc Al-Si. Therefore, Si precipitation causes an expansion of the alloys, i.e. which could reach 0,086% in length (0.26vol%), if all 1.2% Si dissolved at 540°C could be quenched in and precipitated afterwards. The contribution of Si precipitation to the expansion is directly related with the volume fraction of precipitated Si and linear change of the alloy at a temperature T. Therefore, the $\Delta l_{prec}$ term can be calculated as:

$$\Delta l_{prec}(T) = k.V_{frac}(T).l(T) \qquad (3.14)$$

where,

$V_{frac}(T)$ is the volume fraction (in adimensional units) estimated by modelling (3.2.2) at a temperature $T$.

$k$ is the additional volume change of Si-diamond structure from Al-Si fcc ($=7.13x10^{-4}$).

$l(T)$ is the length of the sample at a temperature T.

Finally, the $\Delta l_{AlSi}$ *of the alloy* can be calculated by combining (3.13) and (3.14) as:

$$\Delta l_{AlSi}(T) = f_{Al}\Delta l_{Al}(T) + f_{Si}\Delta l_{Si}(T) + k.V_{frac}(T).l(T) \qquad (3.15)$$

From this equation, the Coefficient of Thermal Expansion can be calculated numerically as explained before in 2.3.1.1.

## 3.3 Basics Composite Mechanics

Composite materials are inherently inhomogeneous, in terms of both elastic and inelastic properties. One consequence of this is that, on applying a load, a non-uniform distribution of stress is set up within the composite. Much effort has been devoted to understanding and predicting this distribution, as it determines how the material will behave and can be used to explain the superior properties of composites over conventional materials.

### 3.3.1 The slab model

The simplest way to model the behaviour of a composite containing continuous, aligned fibres is to treat it as if it were composed of two slabs bonded together, one of the matrix and the other of the reinforcement, with the relative thickness of the latter in proportion to the volume fraction of the fibres (designated as f). The response of this “composite slab” to external loads can be predicted easily, but its behaviour will closely mirror that of the real composite only under certain conditions (Figure 3.1).

*Axial stiffness*

The model is most useful for the case of a normal stress being applied parallel to the fibre axis (the “3” direction). The two components of the slab composite must have the same strain in this direction, $\varepsilon_{3C}$, equal to the ratio between the stress and the Young’s modulus for each of the two components.

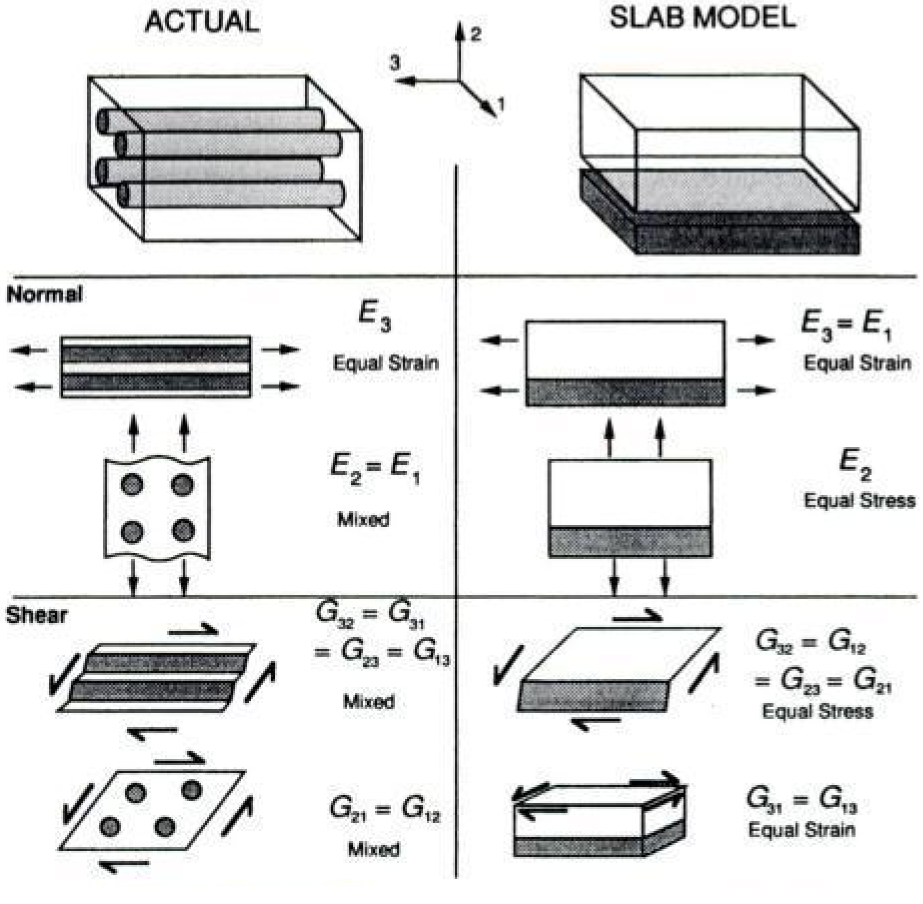

**Figure 3.1.** Schematic illustration of how the elastic constants are defined for a real fibre composite and for the slab model representation. The partitioning of stress and strain between the constituents is noted in each case.

But means of a simply mathematical treatment [Clyne, 1993] the Young’s modulus of the composite can be written as:

$$E_{3C} = (1 - f)E_M + fE_I \qquad (3.16)$$

This well-known *“Rule of Mixtures”* indicates that the composite stiffness is simply a weighted mean between the moduli of the two components, depending on the volume fraction of reinforcement.

*Transverse stiffness*

Prediction of the transverse stiffness of a composite from the elastic properties of the constituents is far more difficult than the corresponding axial value. This is because, in a real composite, the phases are not equally stressed nor equally strained, as depicted in Figure 3.1. Furthermore, the symmetry of the composite is different from that of the slab model. The “equal stress” bound is obtained by considering an applied stress in the direction “2“ so that the component strains can be expected in terms of the applied stress. The composite modulus is thus given by [Clyne, 1993]:

$$E_{2C} = \left[ \frac{f}{E_I} + \frac{1-f}{E_M} \right]^{-1} \qquad (3.17)$$

The equal stress treatment is described as a *“Reuss model”*

### 3.3.2 The shear lag model

The most widely used model describing the effect of loading an aligned short fibre composite is the so-called shear lag model, originally proposed by Cox [Cox, 1953] and subsequently developed by others [Outwater, 1956; Rosen, 1960; Dow, 1963], which centres on the transfer of tensile stress from the matrix to fibre by means of interfacial shear stresses. The basis of the calculations is shown schematically in Figure 3.2. The external loading is applied parallel to the fibre axis. The model is based on considering the radial variation of shear stress in the matrix and at the interface. A comprehensive mathematical treatment of the model is given in [Clyne, 1993]. By means of this model, the axial Young’s modulus of the composite can be expressed as:

$$E_{3C} = \left\{ fE_I \left[ 1 - \frac{\tanh(ns)}{ns} \right] + (1 - f)E_M \right\} \qquad (3.18)$$

where,

$n$ is a dimensionless constant given by $n = \left[ \frac{2E_M}{E_I (1 + \nu_M) \ln(1/f)} \right]^{1/2}$

$s$ is the fibre aspect ratio $L/r_0$

$L$ is the fibres' length

$\nu_M$ is the poisson coefficient of the matrix

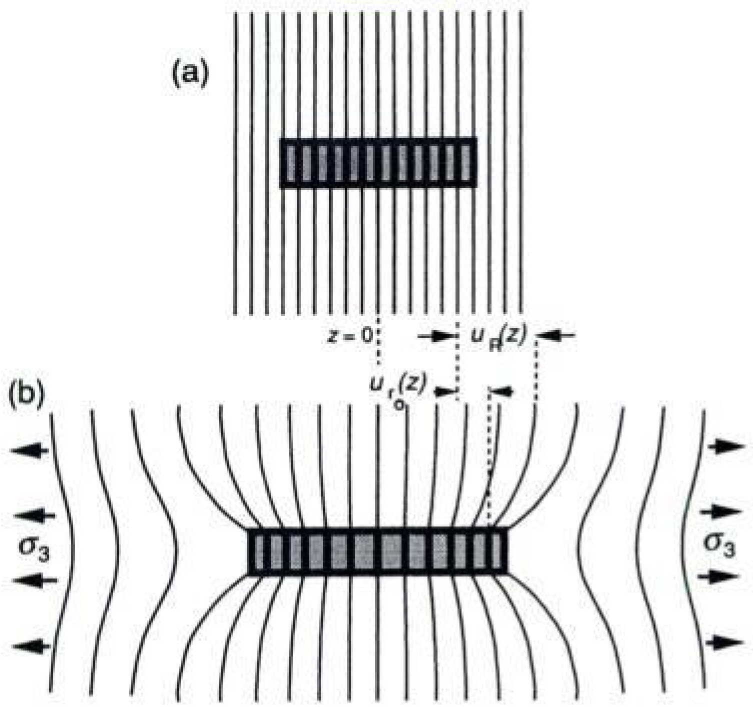

**Figure 3.2.** Schematic illustration of the basis of the shear lag model, showing a) the unstressed system and b) the axial displacements, *u*, introduced on applying tension parallel to the fibre [Clyne, 1993].

# Chapter 4
# Experimental Methods

## 4.1 Description of materials

The different AlSi-alloys and short fibre reinforced materials (SFRM) were produced using a squeeze casting process by LKR, Ranshofen, Austria, using an UBE HVSC VCL 350 as described elsewhere [Requena, 2004]. About 200ppm of Sr were introduced into AlSi7 and AlSi12 alloys in order to modify the eutectic morphology. The composition of the alloys is depicted in Table 4.1. The unreinforced alloys were produced in stepped blocks with sections of different thickness: 2, 6, 10 and 14mm for sections S1, S2, S3 and S4, respectively (Figure 4.1a). The microstructure of the different sections was investigated (Figure 4.1b), observing identical microstructure for the thicker ones: S1 Secondary Dendrite Arm Spacing between 5-7µm, S2 SDAS=10-20µm and S3, S4 SDAS = 20-30µm. Therefore, all samples were produced from the mentioned sections named S3 and S4 in Figure 4.1.

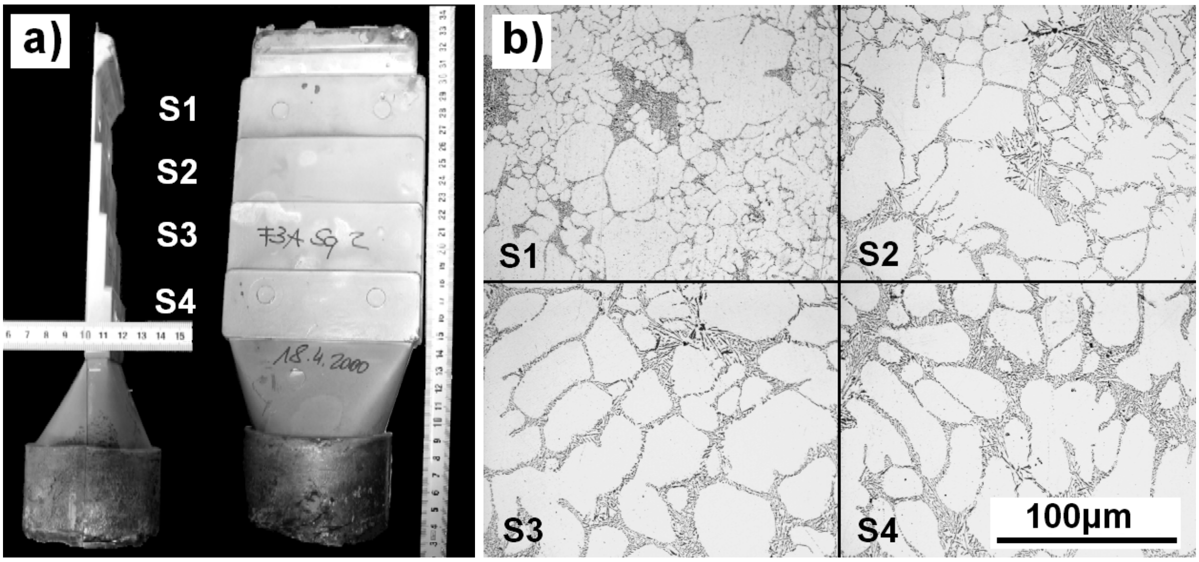

**Figure 4.1.** a) Standard step block of unreinforced-alloys, b) e.g. microstructure of AlSi7 in the different step sections.

Saffil preforms of 107mm diameter x 60mm thickness and 60x30x600mm$^3$ (produced by Thermal Ceramics de France S.A.) of randomly planar distributed short fibres (Figure 4.2) were infiltrated with the unmodified AlSi-alloys in order to obtain the SFRMs samples of 20% volume fraction, which will be referred to as AlSiX/$Al_2O_3$/20s.

| Alloy | Si | Fe | Cu-Ni | Sr |
|---|---|---|---|---|
| AlSi1.1 *) | 1.11 | 0.09 | <0.01 | - |
| AlSi1.7 | 1.74 | 0.07 | <0.01 | - |
| AlSi7 *) | 7.04 | 0.07 | <0.01 | - |
| AlSi12 *) | 11.87 | 0.08 | <0.01 | - |
| AlSi18 *) | 17.86 | 0,16 | <0.01 | - |
| AlSi7Sr | 6.95 | 0.07 | <0.01 | 0.017 |
| AlSi12Sr | 11.77 | 0.08 | <0.01 | 0.018 |

**Table 4.1.** Composition of the alloys [wt.%], Al balance.

*) Matrix alloys for SFRMs

Samples of different sizes and shapes were cut from the original ingots for testing. All the specifications of samples are presented in Table 4.2.

| **Samples for** | **Dimensions [mm]** | **Obs.** |
|---|---|---|
| Metallography | 10 x 10 x 10 | |
| Dilatometry | 4 x 2 x 15 | SFRMs samples were cut parallel and perpendicular to the random fibre plane |
| DMA (E mod.) | 2 x 4 x 55 | SFRMs samples were cut parallel and perpendicular to random fibre plane |
| DSC | $\Phi$=6, thickness=1 | |
| Isothermal Calorimetry | $\Phi$=15, thickness=1 | A pile of 20 samples was used. Parallel faces are required for optimal conductivity between the samples. |
| SANS | 20 x 20 x 4 | |
| Compression | $\Phi$=10, length=15 | SFRMs samples were cut parallel and perpendicular to random fibre plane |
| Thermocycling | 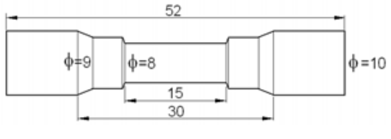 | SFRMs samples were cut parallel to random fibre plane |

**Table 4.2.** Specifications of machined samples for different tests.

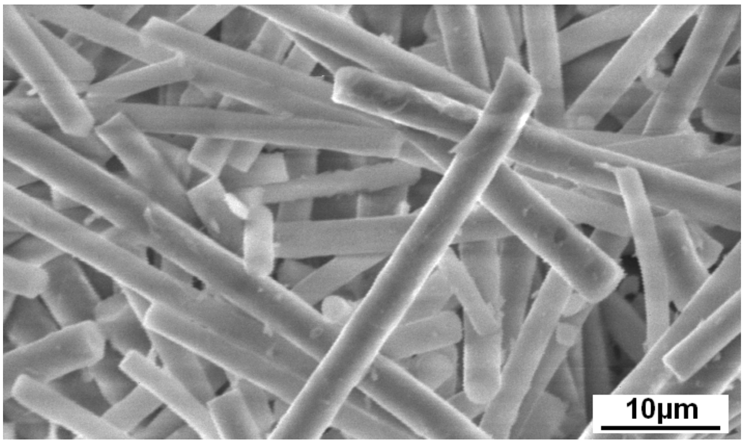

**Figure 4.2.** SEM image of Saffil preform on the plane of planar fibre distribution.

## 4.2 Thermal treatments

Different thermal treatments of the materials were carried out (Table 4.3). The as cast condition is called T1. The solution treatment (ST) was carried out in a Linn High Therm furnace model 70.26 at 540°C followed by water quenching. Samples for spheroidization kinetic studies were solution treated during 5, 20, and 80 minutes, 4, 16 and 64 hours. T4 is naturally aged after quenching in water from the solution treatment temperature. T4a-c comprise different cooling rates from ST. T5 and T6s are stabilization treatments. T6* and T6 "ageing" treatments were performed after T4 in the TMA (Thermomechanical Analyser) 2940 CE dilatometer (see 4.6.1). T4a-e and T7* thermal treatments were performed in the dilatometer.

<table>
<tr><td><b>T1</b>: as-cast</td><td colspan="8">Stabilising treatments: <b>T5 :</b> T1 + 300°C/2h <b>T6s :</b> T4 + 300°C/2h</td></tr>
<tr><td colspan="9"><b>T4</b>: T1 +540°C/4h + $H_2O$ (SFRMs) or 540°C/15' + $H_2O$ (unreinforced alloys)</td></tr>
<tr><td colspan="4">Cooling rate variations:<br><b>T4a</b>: T1 +540°C/4h →<b>20</b>K/min→RT<br><b>T4b</b>: T1 +540°C/4h →<b>3</b>K/min→RT</td><td colspan="5"><b>T4c</b>: T1 +540°C/4h →<b>1</b>K/min→RT<br><b>T4d</b>: T1 +540°C/4h →<b>5</b>K/min→RT<br><b>T4e</b>: T1 +540°C/4h →<b>300</b>K/min→RT</td></tr>
<tr><td colspan="9">Kinetic studies of Si precipitation at temperatures along the heating cycle of the calorimeter and dilatometer:</td></tr>
<tr><td>Temperature [°C]</td><td>175</td><td>200</td><td>250</td><td>270</td><td>300</td><td>370</td><td>420</td><td>460</td></tr>
<tr><td>T4: 3K/min to T+$H_2O$</td><td><b>T6*a</b></td><td><b>T6*b</b></td><td><b>T6*c</b></td><td><b>T6*d</b></td><td><b>T6*e</b></td><td><b>T6*f</b></td><td><b>T6*g</b></td><td><b>T6*h</b></td></tr>
<tr><td>T4: 3K/min to T/1h+$H_2O$</td><td></td><td><b>T6a</b></td><td></td><td></td><td><b>T6b</b></td><td></td><td></td><td></td></tr>
<tr><td>T4: 3K/min to T/10h+$H_2O$</td><td></td><td><b>T6c</b></td><td></td><td></td><td></td><td></td><td></td><td></td></tr>
</table>

**Table 4.3.** Designation of thermal treatments.

## 4.3 Microstructural analysis

### 4.3.1 Conventional metallography

The materials were ground with 320, 500, 1000, 2400, 4200 Struers SiC paper (using water as coolant with a rotating speed of 300RPM) and subsequently polished with DP-diamond paste of 3 and 1 µm particle diameter (with a rotating speed of 150RPM and Dp-Lubricant blue (Struers) as coolant). Polishing with MgO was performed, if necessary.

Light Optical Microscopy (LOM) was performed by means of a Zeiss Axioplan microscope with digital imaging system. Optical zoom between 2.5 and 100X were available in this device.

Deep etching with NaOH 10wt.% was performed in order to produce enough contrast between Al and Si during SEM investigation (by contrast edge effect [Vander Voort, 1984]). The samples were submerged in the solution during 2 minutes and consecutively cleaned with water.

SEM investigation was carried out by means of a Philips XL-30 scanning electron microscope using a beam of 15kV. A beam of 20KV was selected for spheroidization kinetic studies. 15kV voltage produces a better resolution of the microstructure, but not enough contrast between Al and Si phases, which is required for image analysis. Different magnifications were used to reveal about 100-200 Si particles for quantitative analysis within each picture.

### 4.3.2 Image analysis

SEM images were analysed using the SigmaScan Pro software. More than 800 hundred Si particles for each solution treatment time of the different alloys and about 400 in the composite material were analysed by measuring the perimeter and area of each Si particles (Figure 4.3). The shape factor $F_p$ of each Si particle was calculated by (4.1), where $P$ and $A_p$ represent the perimeter and area, respectively [Ogris, 2002b]. $F_P = 1$ for a perfect circle and increases the more nonconvex and elongated the particles are. A frequency count of the area and shape factor of Si particles was performed in each picture showing an unsymmetrical unimodal distribution (extended towards bigger particles) for both microstructural parameters. Therefore, the mode value (observation with greatest frequency) of both microstructural parameters was calculated in order to represent the most characteristic values. Finally, the representative area and shape factor of each thermal condition was calculated by (4.2) and (4.3), respectively:

$$F_p = \frac{P^2}{4\pi A_P} \qquad (4.1)$$

$$A = \frac{1}{n}\sum_{k=1}^{n} A_i \qquad (4.2)$$

$$F = \frac{1}{n}\sum_{K=1}^{n} F_i \qquad (4.3)$$

where $A_i$ and $F_i$ denote the mode values for the area and shape factor of the i-th picture, and $A$ and $F$ indicate the representative area and shape factor of each thermal condition averaged over the corresponding pictures analysed.

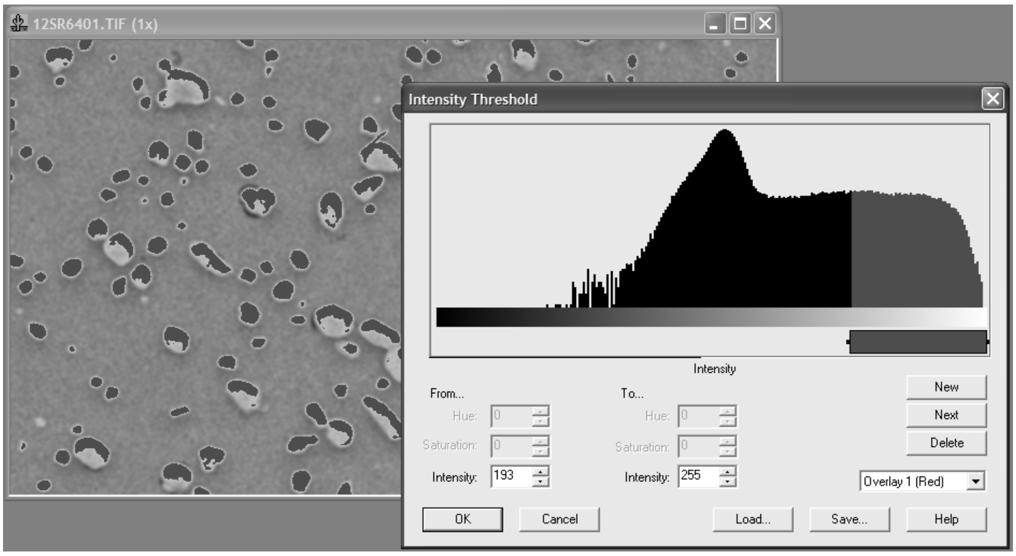

From...
Hue: 0
Saturation: 0
Intensity: 193

To...
Hue: 0
Saturation: 0
Intensity: 255

Overlay 1 (Red)

**Figure 4.3.** Determination of Si particle area and perimeter from a SEM image of solution treated AlSi7Sr (540°C/64h) using SigmaScan Pro software.

## 4.3.3 Three-dimensional imaging

### 4.3.3.1 Deep etching

Small samples of unmodified and Sr-modified AlSi-alloys and AlSiX/$Al_2O_3$/20s composite materials in the as cast condition and after 20 minutes and 4 hours of solution treatment at 540°C were etched with 17wt. % HCl during 48 hours to remove the aluminium phase. A percolating Si-network for AlSi7 and AlSi7Sr could be conserved in the as cast condition. On the other hand, all solution treated samples disintegrated completely during deep etching. A consistent Si-$Al_2O_3$-structure for the composite material was extracted from all the studied thermal conditions. Si and Si/$Al_2O_3$-structures were investigated by observation of the 3D-networks in a high resolution FEI strata DB 235 electron microscope. Three-dimensional stereo images of the percolating Si-$Al_2O_3$-network were carried out by means of the software ZSEM version 2.06 [Stampfl, 1996]. The 3D images were constructed from two different stereo images of the same position of the sample but with a rotation angle of 3 degrees between them. The software identifies homologue points for both images performing a 3D picture in red and green scale.

#### 4.3.3.2 FIB / FIB EDX tomography

The 3D analysis of the samples was performed using a 3D FIB tomography method similar as described in [Giannuzzi, 2005]. The FIB microscope consisted of a Dual Beam Workstation (FEI Strata DB 235) using the electron beam for imaging and the focused ion beam (Ga) for milling of the sample and Pt deposition (Figure 4.4). Normally, FIB tomography employs a combination of sample milling and secondary electron imaging. In this case, the resolution depends on the precision of individual FIB cuts and the SE images. In [Holzer, 2004] it was shown that the overall resolution is below 100 nm in the case of porous $BaTiO_3$ ceramics. Hence the term FIB nanotomography is used. However, some materials do not provide sufficient SE/BSE contrast between phases. In this case, the EDX signal might be used in addition to the SE images. Using this approach, the resolution depends on the precision of FIB milling and on that of the EDX mapping. The later depends on the material and acceleration voltage of the electron beam [Heinrich, 1998]. In this study, FIB tomography using SE images alone and SE images with EDX mapping was used investigating samples of the Al-Si system. The following procedure was used:

(a) First a protective layer of Pt is deposited over the area of investigation. The Pt layer serves not only as protection but helps in suppressing curtaining effects [Giannuzzi, 2005], hence improving the quality of the cuts, and in providing a sharp interface to the sample material. This interface was later used for alignment of individual slices for the 3D reconstruction.

(b) Reference markers for slice alignment are milled into the sample surface.

(c) A rectangular trench near the deposited Pt layer is milled using a high ion beam current of 20nA. The trench is sufficiently large to permit electron imaging and EDX analysis at 52° sample tilt (angle between the electron and the ion beam on the system used in this study).

(d) The cross section is polished employing a Ga ion beam current of 1nA and subsequently imaged using the electron beam at an accelerating voltage of 6kV. The ion beam current provides a smooth polished surface at reasonable milling time. In the case of the sample AlSi12, chemical analysis of Si and Al was performed by energy dispersive spectroscopy (EDS) with an acceleration voltage of 8kV using a Si EDX detector (EDAX).

(e) The 2D sectioning and imaging sequence was repeated with an increment of 300 nm between individual slices for the samples AlSi7 and AlSi12, and 58nm for the sample AlSi7Sr in order to collect the data for the 3D reconstruction of the nano-morphology of the Si inclusions in the eutectic structure (see Table 4.4).

(f) Finally, the 2D images are aligned using cross correlation of reference markers and the Pt-sample interface using the software package Amira 3.1. The voxel size was correlated with the pixel size and corrected in the vertical axis since images are tilted 52°. Image segmentation was performed manually by marking individual grains of Si in each slice. Different smoothing options were tried and carefully checked. About 200 images were processed for each sample of unmodified and Sr-modified AlSi7 alloy, and 30 EDX maps for the eutectic AlSi12 alloy.

| Voxel size (nm) | x | y | z |
|---|---|---|---|
| AlSi7 AC | 59 | 75 | 58 |
| AlSi7Sr AC | 59 | 75 | 58 |
| AlSi12 AC | 59 | 75 | 300 |

**Table 4.4.** Voxel sizes of the different 3D reconstructions (AC = as cast, z: slicing direction, see Figure 4.4).

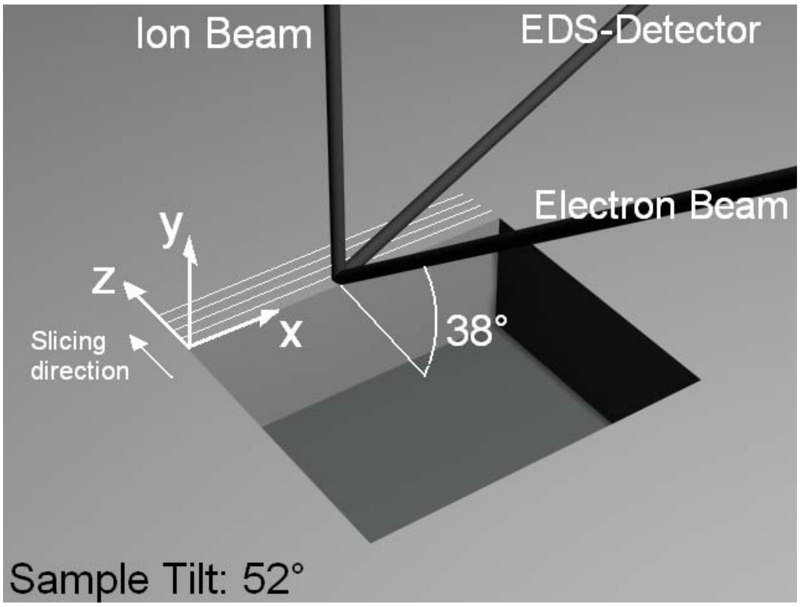

**Figure 4.4.** Schematic FIB cross section imaging method (z: slicing direction). The angle between the electron and ion beam is 52°.

### 4.3.4 Transmission Electron Microscopy (TEM)

Transmission Electron Microscopy was performed on AlSi1.7 after different treatments in a Philips CM200 (200 kV) High Resolution TEM at the Institute of Materials Physics (Vienna University, Austria). The preparation of the TEM foils was done by means of two methods: electropolishing (70% methanol, 30% nitric acid, 35 V, -30°C) and ion milling ($Ar^+$, 6 kV, 1 mA, incident beam angle: 15°, temperature of liquid nitrogen). The identification of the phases was carried out using selected area diffraction and energy dispersive X-ray analysis.

### 4.3.5 Small Angle Neutron Scattering (SANS)

SANS was employed to analyse the evolution of the size distribution of Si precipitates in AlSi1.1 and AlSi12 samples during “ageing” from different initial thermal conditions. Basics of the SANS technique can be found elsewhere [Kostorz, 1979]. The measurements were performed with the instrument SANS-2 at the Geesthacht Neutron Facility (GeNF). Selector-monochromated neutrons with a mean wavelength of $\lambda$=0.58nm and a wavelength spread of $\Delta\lambda/\lambda$ = 10% were used. The neutron beam impinging on the ~2.5mm thick samples had a diameter of 8mm. Four different detector distances (1, 3, 9 and 21m) were used together with appropriate collimations to cover scattering vectors $q$ from 0.03 to 3nm$^{-1}$ ($q=4\pi.\sin\theta/\lambda$, where $2\theta$ is the scattering angle). Scattered neutrons were recorded with 50 x 50cm$^2$ area detector using 128 x 128 pixels. Measured intensities were corrected for the sample transmission, background intensity and detector response.

The measured SANS spectra was analysed by means of the software SANDRA v4.3.6 [GKSS, 2000] from where the scattering curves were obtained by radial integration of the spectra. For this calculation, it is necessary to provide also information about the thickness and transmittance (coefficient between neutrons passing the sample and total emitted) of the sample.

### 4.3.5.1 General description of SANS-2

SANS-2 is mainly dedicated to neutron small-angle scattering studies of precipitates, clusters, interfaces, grain sizes, magnetic structures etc. in materials like metals, ceramics, polymers and colloids using cold non-polarised and polarised neutrons (Figure 4.5). A special feature is that all components which define the sample environment are movable on air cushions. The sample environment area is variable from a few mm up to 2.5 m length. Thus SANS-2 is the most variable instrument for small angle scattering at GeNF [GKSS, 2000].

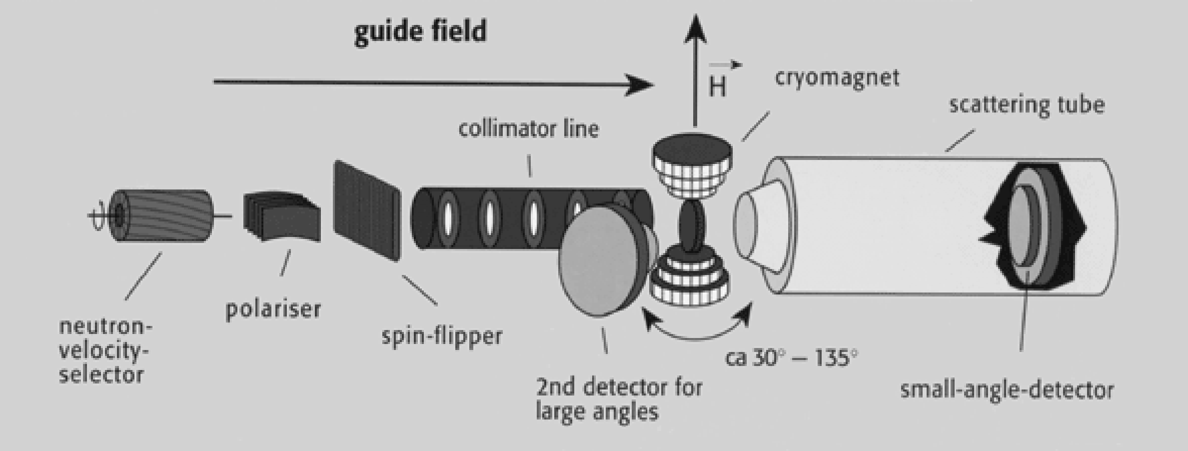

**Figure 4.5.** Schematic view of the small-angle scattering instrument SANS-2 [GKSS, 2000]

The following sample environments are available:

1. A conventional electro-magnet with a remote controlled sample changer. The vacuum chamber is directly connected to the collimator and detector tubes, so

that samples can be measured without any windows. The magnetic field (up to 1.7 T) is horizontal. A closed cycle refrigerator with a temperature range from 10 K to 300 K is also available.

2. A conventional electro-magnet with a vertical field (up to 1 T). An additional area detector can be moved around the sample in a distance of about 1m. This allows the simultaneous measurement of both the small angle scattering and the diffuse wide angle scattering (fig.1). The system contains a refrigerator (10 - 300K) and a remote controlled sample changer.
3. A superconducting magnet (up to 5 T) with a closed cycle refrigerator (10 - 300K) produces its magnetic field parallel to the flight direction of the incident neutron beam.
4. Chamber for large samples with a remote controlled sample changer operated either with vacuum (without windows) or with inert gas (e.g. He, etc.).
5. A furnace especially for polymeric, biological or chemical samples (e.g. liquids or powders), temperature range from -30 to 250 °C can be operated either with inert gas (e.g. He etc.) or in vacuum.
6. Open sample table, with a rotating table, a tilting table and a linear translation table can support equipment of external users such as furnaces, special sample holders, or other bulky and heavy instruments.

## 4.4 Thermal analysis

### 4.4.1 Thermal expansion measurements

Dilatometric tests were carried using a TMA 2940 CE thermal mechanical analysis equipment (TA Instruments) .The expansion ($\Delta l$) of the specimens was measured between RT and 540°C at a heating rate of 3K/min in a nitrogen atmosphere. A numerical derivative of the $\Delta l$ vs. T-curve smoothed within intervals of T±12.5K provides the instantaneous coefficient of thermal expansion (CTE) at a temperature T as:

$$\alpha_T = (1/L)*dL/dT \qquad (4.4)$$

where, L is the length of the specimen at the respective temperature T.

The range of CTE calculations was between 50 and 510°C to avoid the transition range of heating and cooling, respectively. Specimens of the composite material were tested with their longitudinal axes within the random fibre plane and in the perpendicular direction.

### 4.4.1.1 General description of TMA 2940

The thermomechanical analyser (TMA) measures linear changes in the dimension of a specimen as a function of time, temperature (in the range between –70°C and +1000°C), and force. A schematic of the instrument is shown in Figure 4.5.

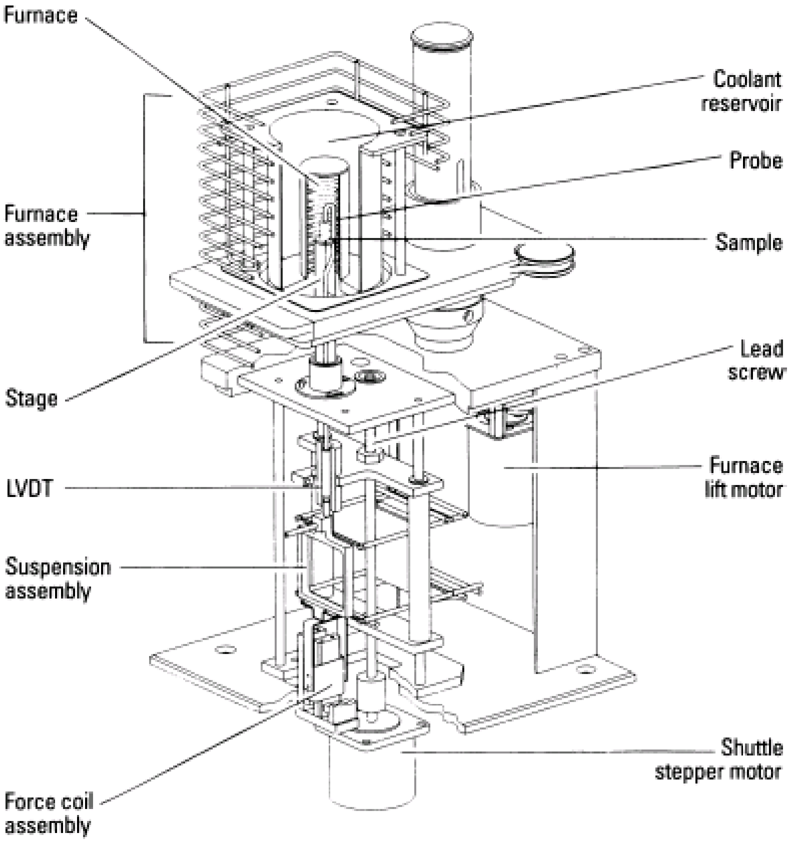

**Figure 4.5.** TMA 2940 (TA Instruments) schematic [Hassel, 1991]

The heart of the device is a moveable-core linear variable differential transformer (LVDT), the output of which is proportional to the linear displacement of the core caused by changes in sample dimensions. The core itself is part of a quartz probe that contacts the sample.

In the TMA, the sample is positioned above the LVDT, on the quartz stage and the moveable probe was placed on the top of the sample (see Figure 4.6). The quartz probe with a low coefficient of thermal expansion of about 0.5ppm/K transmits changes in the length of the specimen to the transducer (LVDT) with a resolution of 0.1µm.

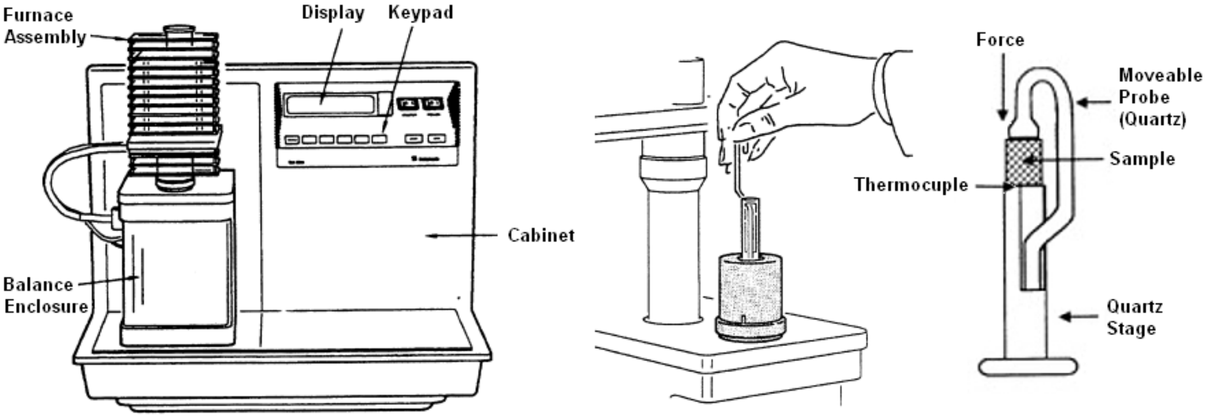

**Figure 4.6.** Specimen positioning in the TMA 2940 [TMA, 1999]

Temperature control of the sample is achieved by programming a low mass furnace, with heating rates between 0.01 and200 K/min, that is automatically lowered to surround the sample stage and the probe. The sample temperature is measured using a thermocouple, positioned close to the sample. An optional cooling device placed around the furnace core accommodates programmed cooling and subambient operation. The furnace is filled with nitrogen during the experiments (usually 100 ml/min).

Force applied to the sample (0.001 to 1N) is generated and controlled by an electromechanical coil. The force can be held constant or varied during an experiment. The exerted pressure by the probe, with a diameter of 3mm, results in a stress of 7kPa.

### 4.4.2 Calorimetry

#### 4.4.2.1 Differential Scanning Calorimetry (DSC)

DSC (Differential Scanning Calorimetry) were carried out in AlSi1.1 and AlSi1.7 samples. AlSi1.7 was tested in a DSC 2920 equipment using a heating rate of 3 and

5K/min in nitrogen atmosphere appropriated to establish thermal equilibrium in this device. DSC measurements in AlSi1.1 were performed in a power-compensated thermal analyser Perkin-Elmer DSC7 calorimeter at TECSEN (Faculté des Sciences et Techniques de St-Jérôme, Marseille, France), subjected at different heating rates of 5, 10, 20, 50 and 100K/min. All tests in both differential scanning calorimeters were carried out after different thermal treatments in a temperature interval between 30 and 540°C.

### 4.4.2.1.1 General description of DSC 2920 CE

A complete DSC 2920 CE system consists of the instrument; a DSC, Dual Sample DSC, or Pressure DSC cell; and a controller (Figure 4.7a). Both the temperatures and the heat exchanges associated with transitions in materials can be easily and rapidly measured by the system. The measurements provide quantitative and qualitative data relative to physical or chemical changes of a material involving endothermic or exothermic processes with a sensitivity of 0.1µW.

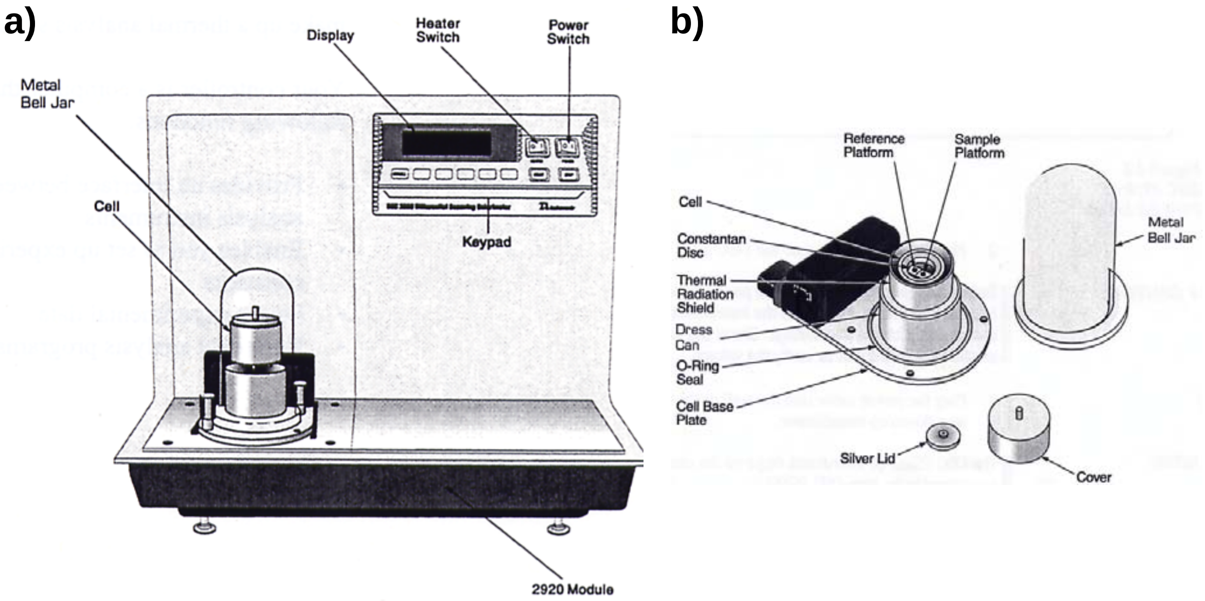

**Figure 4.7.** General view of DSC 2920 device.

The standard and dual sample DSC cells (Figure 4.7b) both use a constantan (thermolelectric) disc as a primary heat-transfer element. A silver heating block, capped with a vented silver lid, encloses the constantan disc. The selected sample(s) and an inert reference are placed in pans that sit on raised portions of the disc. Heat is transferred through the constantan disc to both the samples(s) and reference pans. Differential heat flow to the sample(s) and reference are monitored by the chromel-constantan area thermocouples. The thermocouples are formed at the junctions of the constantan disc and the chromel wafers welded to the underside of the two raised portions of the disc. Chromel and alumel wires are connected to the chromel wafers at the thermocouple junctions to measure sample temperature. The alumel wire welded to the reference wafer is for thermal balance.

Purge gas, entering the heating block through an inlet in the DSC cell's base plate, is preheated to block temperature by circulation before entering the sample chamber through the purge gas inlet. Gas exits through the vent hole in the silver lid.

Vacuum and air cooling ports on the DSC 2920 CE lead to openings in the cell but not directly to the sample chamber. A bell jar, placed over the cell and sealed with an O-ring, protects the operator from evolved gases and permits cell evacuation.

#### 4.4.2.1.2 General description of Perkin-Elmer DSC7

The Perkin-Elmer-DSC7 device consists of a dual sample DSC cell with a furnace facility permitting scans between 20 and 600°C. The measurements can be performed in an nitrogen or air atmosphere with a maximum heating rate of 80K/min. In-situ cooling of samples can be performed up to 300K/min. This device achieves a very high calorimetric accuracy and precision better than 1 and 0.1%, while its heat-flow sensitivity is about 0.1µW.

**Figure 4.8.** General view of Perkin-Elmer DSC7 device.

### 4.4.2.2 Isothermal calorimetry

Isothermal calorimetric measurements were carried out on AlSi1.1 and AlSi12 alloys by means of a Tian-Calvet heat conduction calorimeter (at TECSEN, Marseille) measuring the heat flow, dH/dt, versus time. These calorimetric curves give directly the isothermal reaction kinetics. Curves displaying a heat flow minimum are typical for reactions involving nucleation and growth mechanisms and yield sigmoid-shaped curves when plotting the heat evolved (obtained by integrating heat flows) or the fraction transformed.

The time elapsed between quenching of the specimens, drying and transfer into the calorimeter after preheating to a temperature slightly higher than that of the apparatus is about 5min. As the parasitic heat effects due to the introduction of samples into the calorimeter last for about 30min in spite of preheating, curves are not quantitative for times shorter than 30min.

Regarding the DSC results for AlSi1.1, the isothermal calorimetric measurements were performed at a temperature close to 180°C, which after calibration was determined to be 176.5°C.

#### 4.4.2.2.1 Description of Tian-Calvet microcalorimeter

The calorimeter consists of two symmetrical thermal fluxmeters, each constructed by a series of 480 thermocouples surrounding a cylindrical hole for the measurement

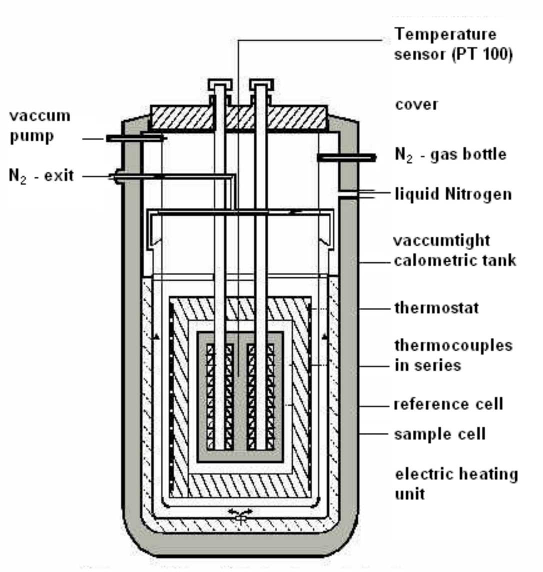

**Figure 4.9.** General diagram of Tian-Calvet microcalorimeter.

cells. The electric signal delivered by the difference in output voltage of the two fluxmeters is proportional to the thermal effect occurring in the cells. It is calibrated by using electrical heaters inside the cells. The temperature of the calorimeter (-190 to 200°C) can be regulated by using a cold nitrogen gas flow and electric heating.

The calorimeter can be used for the measurement of enthalpies of mixing and solution, enthalpies of fusion and transition, enthalpies of reactions, enthalpies of adsorption and desorption and heat capacities. For each application suitable measurement cells are available.

## 4.5 Mechanical properties

### 4.5.1 Hardness measurements

#### 4.5.1.1 Brinell hardness

Samples of identical shapes used for dilatometric measurements were used to perform hardness tests by means of a universal tester model M1C010 provided by Emcostest. Brinell hardness was measure using a load of 10kg and 1mm ball. The AlSi1.1 and AlSi7 alloys were tested at different thermal conditions.

#### 4.5.1.2 Vickers hardness

The same hardness tester device was used for measuring the Vickers hardness of the Si-$Al_2O_3$ networks. After dissolving the $\alpha$-Al of the SFRMs (see 4.4.1), Vickers hardness using a load of 0.1kg was measured on the plane of randomly distributed fibres producing a contact area of about 0.6 $mm^2$ on the remaining Si/$Al_2O_3$ network structure extracted form specimens submitted to different solution treatment periods. The resulting indentation was observed by means of Zeiss Axioplan optical microscope (see 4.3.1), where the diagonals were measured (see Figure 4.10). Finally, the Vickers hardness was estimated by:

$$HV = 1.854\frac{F}{d^2} \qquad (4.4)$$

where,

F = Load in kgf.
d = Arithmetic mean of the diagonals $d_1$ and $d_2$.

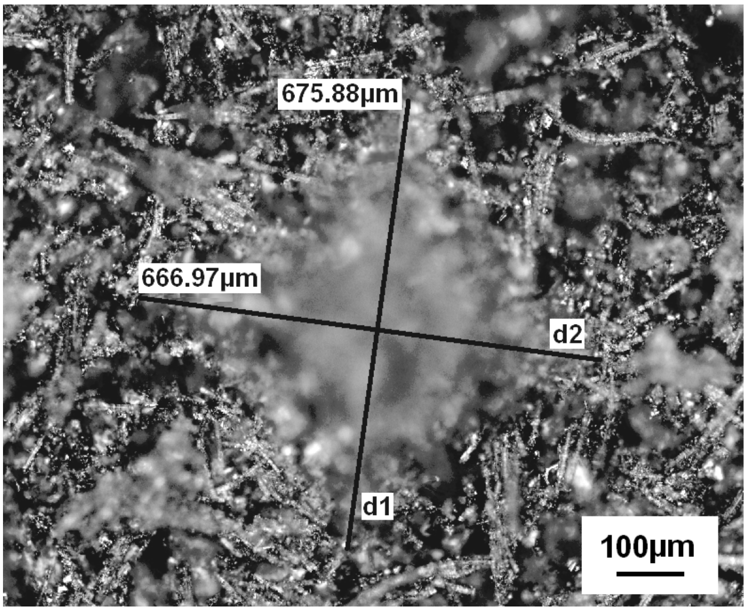

**Figure 4.10.** LOM image of an hardness indentation on a Si/$Al_2O_3$-Network of solution treated AlSi7/ $Al_2O_3$/20s (540°C/5min).

### 4.5.2 Dynamical Mechanical Analyser (DMA)

A simple way of measuring the Young Modulus of a material is to compress it by applying a know compressive force to a block of material, and measure the strain. In general, this is a poor way of measuring the modulus [Ashby, 1980]. For one thing, if the modulus is large, the extension will be too small to measure with precision. And, for another, if anything else contributes to the strain (like creep), then it will obviously lead to an incorrect value of E. Measuring the natural frequency vibration of a rod in e.g. a DMA device is a much better way of measuring E.

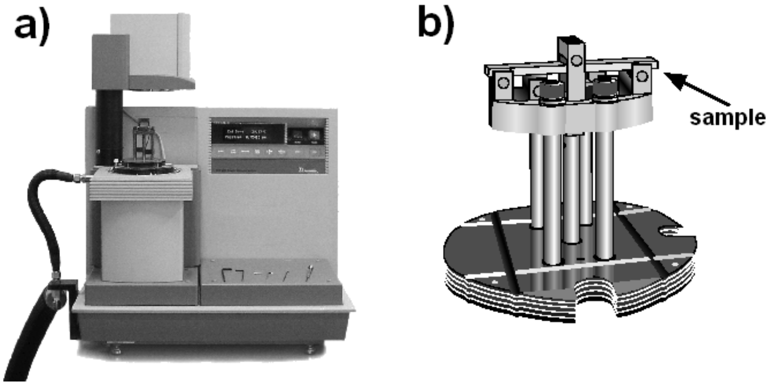

**Figure 4.11.** a) TA Instruments DMA 2980TM apparatus, b) three-point bending clamp [DMA, 2000].

The DMA studies were carried out with a TA Instruments DMA 2980™ dynamic mechanical analyser (Figure 4.11a). The DMA was used to measure the Young's modulus of the specimens as a function of temperature from room temperature to 350°C. The selected heating rate was 3 K/min.

The specimen was clamped, shown in Figure 4.11b, and then subjected to a uniform sinusoidal displacement of a constant maximum amplitude of 40µm. The oscillation frequency was fixed at 1Hz.

The specimen displacement is monitored by an LVDT and the measured lag between the drive signal and the LVDT is the phase angle. The phase angle and drive signal is used to calculate the elastic modulus E' and damping capacity E'' of the specimen [Elomari, 1995].

### 4.5.3 Compression tests

The compression tests of the specimens were carried out with a Gleeble 1500 machine. The samples were heated up to 300°C by alternating current passing through the samples. The temperature is controlled by a spot K-type termocouple located in the middle of the sample (see arrangement in Figure 4.12). Before testing, the temperature profile along the sample was determined, observing a deviation of about 5-10K from centre to border of the samples.

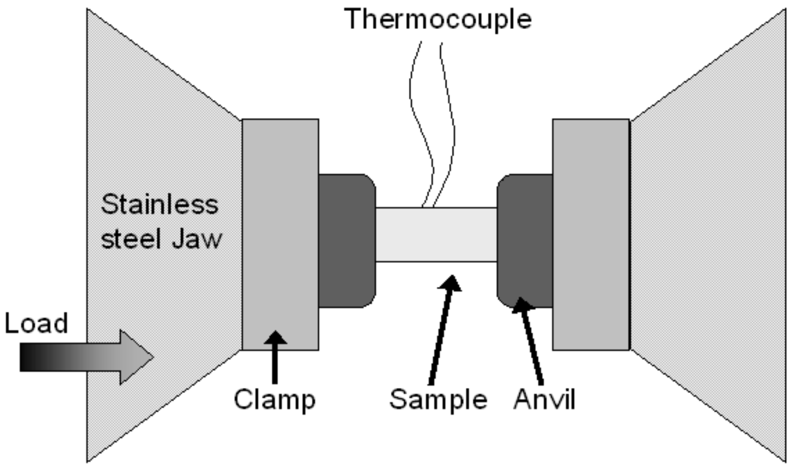

**Figure 4.12.** Arrangement for compression tests in Gleeble 1500 device.

### 4.5.4 Thermal-cycling creep tests

Thermal cycling creep tests were performed in a Gleeble 1500 apparatus (see 4.5.3). The tests were carried out at a constant load of 40 and 60MPa and in a temperature interval between 50 and 300°C. Heating and cooling rates of 12.5K/min were selected with a holding time of 3s after reaching the desired maximal and minimal temperatures. In this way, the total time for a complete cycle was 46 seconds (Figure 4.13). Due to experimental problems during cooling of the samples bellow 100°C, the device was programmed for pressure-air cooling from 110°C to the desired temperature of 50°C. Finally, the temperature amplitude in each real cycle was about 235K, between 65 and 300°C.

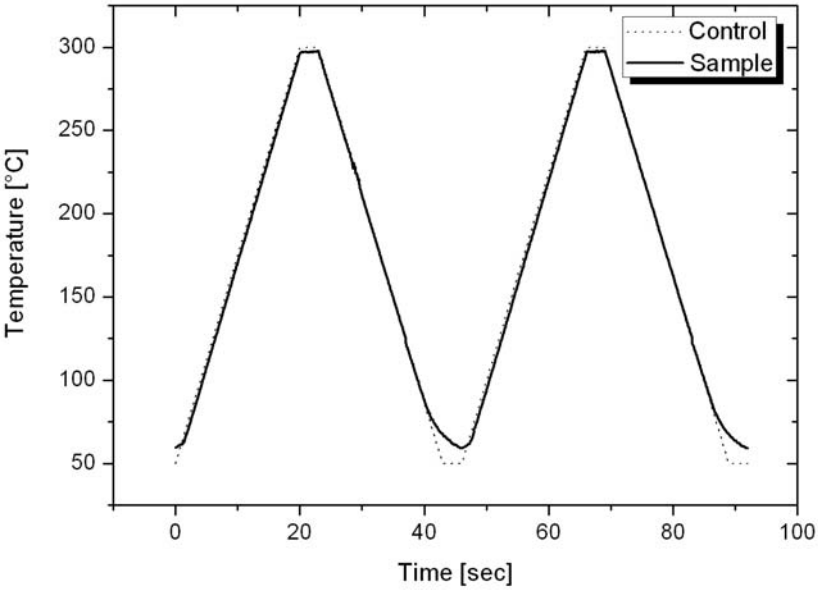

**Figure 4.13.** Measured temperature during thermal-cycling tests in Gleeble 1500 apparatus compared with controlling

Figure 4.14 shows the typical information obtained from thermal cycling “creep” tests, where the measured strain and the applied load and temperature cycles is depicted. The strain rate $\dot{\varepsilon}$ is calculated from the interpolated curve between the true strain at the corresponding temperature minima (equation 4.5). This curve represents the measured remaining strain $\varepsilon_r$ after each cycle.

$$\dot{\varepsilon} = \frac{d\varepsilon_r}{dt} \qquad (4.5)$$

Creep will occur only above 240°C [Lasagni, 2003]. Therefore the real creep rate is much faster than the average creep rate defined in Figure 4.14.

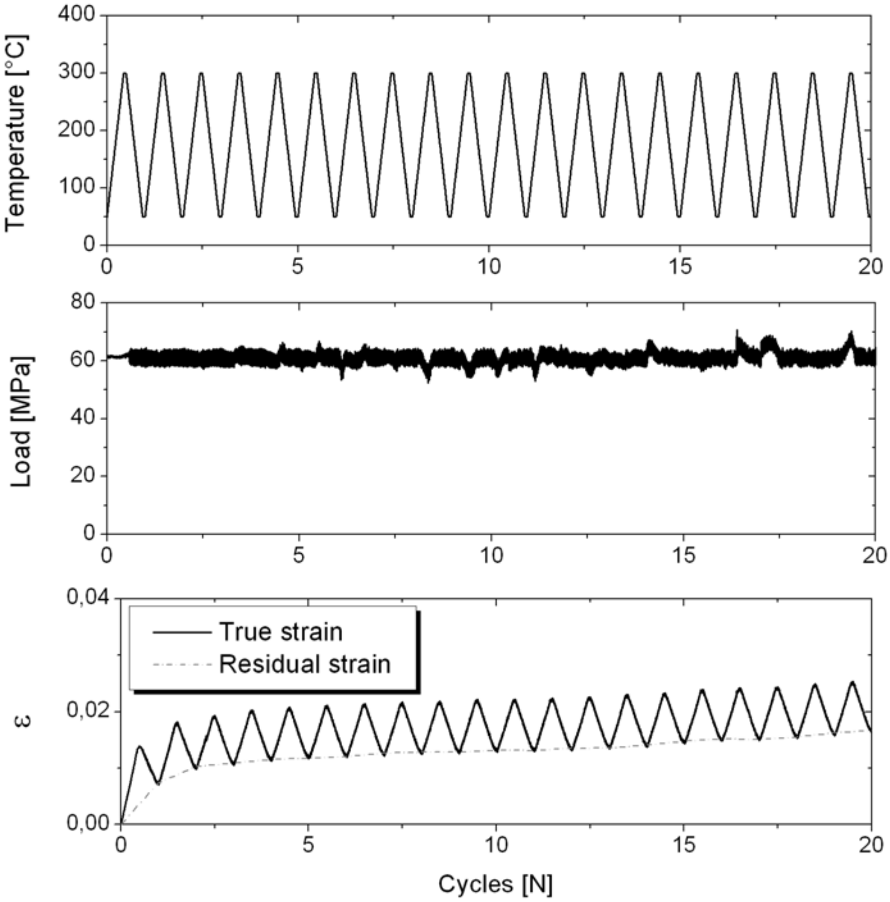

**Figure 4.14.** Measured strain, temperature and applied load during thermal cycling tests.

# Chapter 5
# Results

## 5.1 Metallography

### 5.1.1 Al-Si Alloys

The microstructures of as-cast AlSi1.7, AlSi7 and AlSi12 alloys are depicted in Figure 5.1a, b and c, respectively. The AlSi1.7 material consists of an $\alpha$-aluminium phase (comparable to AlSi1.1) but with a small amount of eutectic Si phase (<1vol.%) along the grain boundaries. The achieved solubility when passing the eutectic temperature of the given casting conditions is concluded to be 1.2 and 1.6vol.% Si. The $\alpha$-phase of AlSi7 is enclosed by the eutectic structure of lamellar Si. The amount of $\alpha$ amounts to about 73vol.% although the equilibrium phase diagram predicts 50vol.%. AlSi12 presents a mostly eutectic microstructure with few primary Si (<0.1vol.%). The $\alpha$-phase occupies almost 27vol.% which means that the alloy behaves hypoeutecticly. The as-cast microstructures of AlSi7Sr and AlSi12Sr modified versions are depicted in Figure 5.1d and e, respectively. The addition of about 200ppm Sr produced full modification of the eutectic structure from a lamellar eutectic morphology into a coral-like structure. Similar to its unmodified version, the morphology of AlSi12Sr shows mostly eutectic with about 27vol.% $\alpha$-dendrites, while in AlSi7Sr the about 76vol.% $\alpha$-phase are enclosed by the Al-Si eutectic.

### 5.1.2 Short Fibre Reinforced Materials (SFRMs)

Figure 5.2 shows LOM-images of the as-cast SFRMs looking onto the plane of random planar fibre orientation. A uniform distribution of the reinforcement can be observed for all the materials (Figure 5.2a). The microstructure of the composites' matrices is similar to that of the unreinforced alloys, presenting $\alpha$-dendrites enclosed by the eutectic structure in both versions of AlSi7/$Al_2O_3$/20s (Figure 5.2b,c). The secondary dendrite arm spacing of about 20µm is in average significantly smaller than that of the unreinforced casting. The eutectic is concentrated around fibres indicating that solidification started in between. About 15vol.% α-phase can be observed between the eutectic for the AlSi12/$Al_2O_3$/20s composite (Figure 5.2e). The AlSi1.1/$Al_2O_3$/20s matrix shows only α-aluminium since the Si is mostly in solution (Figure 5.2d). The AlSi18/$Al_2O_3$/20s composite shows mostly an eutectic microstructure with ~3vol% of primary Si inclusions (Figure 5.2f): Although the AlSi18 matrix is an hypereutectic alloy, about ~2vol.% of α-Al is observed.

### 5.1.3 Si Spheroidization – 2D Image Analysis

The chronology of Si spheroidization of the studied materials is presented in Figure 5.3. Both non-modified alloys AlSi7 and AlSi12 present similarly larger and longer Si particles than the modified versions (AlSi7Sr/AlSi12Sr) in the as cast condition (AC). The average area is about 5 times and 3 times higher and the shape factor is twice as big for AlSi7 and AlSi12 than for AlSi7Sr and AlSi12Sr, respectively (AC in Table 5.1). The AlSi7/$Al_2O_3$/20s (version 1) composite material presents similar Si particles as its unreinforced alloy, while the mean area of the Si particles in the $2^{nd}$ version is 38% lower.

After 80 minutes of solution treatment, the mean area of Si particles of the unmodified solutionized alloys increases by a factor of about 2.5 and the shape factor is reduced by a factor of about 2 (compared to as cast). The shape factor of Si particles of Sr-modified alloys decreases further approaching 1, but the mean area increases by about a factor of 5. The mean area of Si particles for both versions of AlSi7/Al2O3/20s becomes twice as big after the solution treatment than before, while F remains approximately constant for all the studied conditions in SFRM7 (v1) and decreases from 3.4 (in AC) to about 2.5 (from 540°C/5min) in the $2^{nd}$ version (Figure 5.4a).

The size distribution of the Si particles scatters much more in the modified alloys than in the unmodified. The measured standard deviation for the studied alloys increases with solution treatment time amounting 1.5-2.4 and 0.2-0.4 for the Sr-modified and unmodified alloys after 540°C/64h, respectively. The ripening of Si particles in Sr modified alloys (Figure 5.4b) follows a $\sqrt{t}$ law. Both unmodified alloys exhibit slower coarsening rate with a time law like $t^{\beta}$, with $\beta \sim 0.3$. Coarsening of Si particles of the AlSi7/$Al_2O_3$/20s (v1) behaves similar to its AlSi7 matrix but at somewhat bigger A values. The same behaviour is observed for in its 2nd version, but presenting lower A values. After 64 hours of soaking time at 540°C, the mean areas of Si particles approach each other between 8.5-11µm$^2$ for all the studied materials. The shape factor for all samples (Figure 5.4b) becomes relatively constant after 5 min of solution treatment approaching 2 for AlSi7/12, whereas for the Sr-modified alloys *F* becomes around 1.2 at longer exposure times at 540°C.

| Material | $F_{Si}$-AC | $F_{Si}$-80' ST | $A_{Si}$-AC[µm$^2$] | $A_{Si}$-80' ST [µm$^2$] |
|---|---|---|---|---|
| AlSi7 / AlSi12 | 4.2 / 4.6 | 2.4 / 2.0 | 1.3 / 1.0 | 3.1 / 2.8 |
| AlSi7Sr / AlSi12Sr | 2.0 / 1.9 | 1.3 / 1.4 | 0.2 / 0.3 | 1.4 / 1.5 |
| SFRM7 **v1** | 2.7 | 2.8 | 1.6 | 3.8 |
| SFRM7 **v2** | 3.3 | 2.4 | 1.0 | 2.6 |

**Table 5.1**. Microstructural parameters of the Si in the studied materials in as cast (AC) and 80min at 540°C solution treated (80' ST) condition. Note: SFRM7 = AlSi7/$Al_2O_3$/20s.

## 5.2 Three-dimensional imaging

### 5.2.1 Deep etching

Figures 5.5a-f show SEM micrographs of the Si sponge-like structure obtained after dissolving the $\alpha$-Al from the AlSi7 and AlSi7Sr specimens. After < 5 minutes of solution treatment at 540°C a high degree of Si spheroidization was achieved and the original network is disintegrated to form individual Si particles. Therefore, it was not possible to obtain an interconnected network structure of Si from the solution treated samples by deep etching. The as cast AlSi7-alloy (see Figure 5.5a-c) shows a Si structure composed of thin (~1µm) several 10µm long lamellae forming space frame like walls of a few µm width in between the dendritic arms of the dissolved $\alpha$-Al. By the addition of Sr, the microstructure of the lamellar Si space frame changes into a coral like structure consisting of fine (~0.2µm) dendritic Si branches (Figure 5.5d-f) forming dispersed fibrous walls.

Figure 5.6 shows SEM micrographs of the structures obtained after dissolution of the $\alpha$-Al from AlSi7/$Al_2O_3$/20s (version1) in the as-cast condition (see Figure 5.6a and b) and solution treated during 20min (see Figure 5.6c and d) and 4h (see Figure 5.6e and f). Few Si plates not connected to the fibres are observable only in the as cast condition. During solution treatment, Si has coarsened into Si-particles on the $Al_2O_3$ fibres. Si bridges connecting the $Al_2O_3$-fibres are found in the as cast condition and more frequently after 540°C/20min, while they are not observable after 4h of solution treatment.

The morphology of the 2nd version of AlSi7/$Al_2O_3$/20s in the as cast condition shows something different from that of the version 1, presenting a connected Si structure of the unreinforced alloy together with the $Al_2O_3$-fibres. This is clearly illustrated in Figure 5.7a, where an alumina-fibre is connected to the eutectic Si structure by means of Si bridges. Contrarily to the version 1, Figure 5.7b shows connected Si plates in a fibre-free zone.
Deep etched images of AlSi12/$Al_2O_3$/20s and AlSi18/$Al_2O_3$/20s are depicted in Figure 5.8 and Figure 5.9, respectively. Like in AlSi7/$Al_2O_3$/20s (version 2), interconnected Si plates are observable in the as cast condition (Figure 5.9a,b). The Si plates of AlSi18/$Al_2O_3$/20s are bigger than those in AlSi12/$Al_2O_3$/20s and AlSi7/$Al_2O_3$/20s (v2), respectively. Primary Si particles interconnecting the alumina fibres of about $10^4 µm^3$ are observable in as cast and solution treated samples. Si bridges between $Al_2O_3$-fibres are more often observed in AlSi7/$Al_2O_3$/20s and AlSi12/$Al_2O_3$/20s (in as cast and after 20 minutes of solution treatment at 540°C) than in AlSi18/$Al_2O_3$/20s. The last one presents interconnected $Al_2O_3$ fibres by means big primary Si inclusions (see detail Fig. 5.9b) in all studied thermal conditions, and few Si bridges in AC and mostly sheroidizated Si particles on the $Al_2O_3$-fibres.

Figure 5.10 depicts the 3-dimensional structure of the Si-$Al_2O_3$ networks in the as cast condition a) and after 4hours b) of solution treatment at 540°C for AlSi7/$Al_2O_3$/20s (version 1). Thin Si bridges between Si fibres and Si particles at fibres are clearly observable in the as cast condition. In Figure 5.10b, coarse and spheroidizated Si particles can be observed after 4hours at 540°C. No Si-bridges are observable between the fibres at this thermal condition, but occasionally nodes connecting crossing fibres.

### 5.2.2 FIB SEM / EDX tomography

Cross section images of all studied alloys are shown in Figure 5.11. A region of modified-eutectic in AlSi7Sr enclosing primary $\alpha$-Al is presented in Figure 5.11a, where slices in distances of 3,94µm are depicted. Cross section number 4 shows mainly two different structures (placed on both image borders) with different orientations of the fibrous-Si. During sectioning (from image number 4 to 1) both structures joined revealing frameworks of different orientations of Si lamellae. Si free $\alpha$-zones in between are also observable in the sample.

Figure 5.11b presents the cross section of a wide Si eutectic framework in AlSi7 alloy. Si lamellae of about ~3µm thickness are observed in different planes. These Si-lamellae are interconnected by nodes.

Si-EDX-cross section images of the AlSi12-alloy are depicted in Figure 5.11c, where slices at 310nm distant are presented. Several thin Si-plates are observed mostly with similar orientation covering the whole studied region.

Figure 5.12a depicts a reconstructed three-dimensional image obtained from 2D sectioning in AlSi7Sr. The fibrous morphology of the modified eutectic is clearly observed, showing Si fibres and branches of about 0.2-0.4µm in diameter and some micrometers in length (~3-5µm) oriented in many different directions. These fibres are mostly interconnected by nodes of some nanometres in cross section (~0.05-0.1µm$^2$). The intersection of 3 different grains is observed in Figure 5.12b, separated by Si-free grain boundary zones of about 1µm width. Grain A (See Figure 5.12b) shows a long thick Si fibre along the grain boundary with interconnected Si branches growing parallel to the y-axis. Complete interconnection and similar orientation of fibrous Si is observed in the grain B, while Si fibres in grain C oriented are perpendicular to those of grain A and B. In this grain (C), Si fibres seem to be mostly interconnected but some distance from the grain boundary isolated short fibres are also observed. Figure 5.12c shows a detail of the fibrous Si morphology observed at the right side of the cross section. Like in Figure 5.12b, a Si free zone is observed between three different grains (C, D and E). Grain C presents a partially interconnected fibrous-Si morphology of about 0.2µm thickness. The observed fibres of grain E are totally interconnected and thicker than in grain C (~0.5µm diameter). Si fibres of the grain D are partially interconnected and mainly oriented at about 45° to the xy-plane. The thickness and interconnectivity of the fibres shows to be higher near the grain boundary D-E (0.4-0.5µm thickness) and decreases by moving along the z-axis in direction to the grain C (~0.2µm). This morphology is similar to that observed in Figure 5.12b.

The architecture of the reconstructed eutectic Si in AlSi7 (Figure 5.13a) presents Si plates of about 1~3μm thickness. These plates are separated into two different regions (each with clearly preferential Si orientation), which are interconnected by nodes (Figure 5.13b). The connectivity between the Si plates in each region is clearly observed in the 3D images. These connecting nodes (Figure 5.13c) are much thicker (~1-4μm²) than those of the AlSi7Sr-alloy. Since the 3D reconstruction was performed in a sample with only about 10μm in the milling direction (x-axis), only parts of the Si plates are observed here.

The 3D-morphology of the eutectic Si phase in the unmodified AlSi12-alloy (Figure 5.14a) is similar to that of AlSi7, but thinner Si plates of about 0.5-1μm in width were observed. The studied region presents Si lamellae oriented in many different directions but with similar relative orientation as those in AlSi7, where almost perpendicular plates were found. Figure 5.14b shows a rotated region of the studied volume showing parallel Si plates oriented at ~45° to the xy-plane. Like in AlSi7, these Si plates seem to be connected in several nodes (some of them are marked in Figure 5.14b).

## 5.3 Transmission Electron Microscopy

Figure 5.16a,b shows the microstructure of AlSi1.7 alloy in T4 and T6a conditions, respectively. Both samples present a similar microstructure, presenting only dislocation lines and also some loops. No evidence of Si precipitates was observed in both water quenched and heat treated alloy (T6a=T4:200°C/1h). The number of loops is smaller in heat treated sample than in the water quenched. The studied samples present lamellar Si or inclusions of about 3-10μm as it can be observed in Figure 5.16c.

The morphology of Si precipitates in T6*d, T6*e, T6*f, T6*g, T6b and T6c conditions are depicted in Figure 5.17a-f, respectively. The studied thermal conditions are marked on DSC runs in Figure 5.15. The alloy in the T6*d condition (T4:RT→3K/min→270°C) exhibits semicoherent globular and Si platelets between 30-80nm and 30-150nm in width, respectively. These precipitates were mainly observed on {111} planes. The thickness of the mostly triangular platelets limited by <110> orientations seams to be less than 10nm. Thus the volume can be estimated to be between $2x10^3$ - $4x10^4$nm³, while those of globular morphology amounts between $1x10^4$ - $2x5x10^5 nm^3$. The microstructure of AlSi7 after T6*e shows mostly globular precipitates and some globular with similar size values like in the T6*d condition. TEM micrographs of AlSi1.7 alloy after continuous heating up to 370°C (T6*f) presents only globular Si precipitates of about 40-80nm. Similar morphology of the Si precipitates was observed in the T6*g condition (T4:RT→3K/min→420°C), depicting globular Si of about 100-150nm but clearly in a lower number density.

By isothermal heating at 300°C during 1 hour (T6b: Figure5.17e) mainly the Si platelets from T6*d condition seem to be dissolved, presenting mostly globular Si precipitates reaching 20-60nm sizes. On the other hand mostly globular Si precipitates of 20-40nm (T6b, Figure 5.17d) were observed after isothermal heating at 200°C/10h.

Figure 5.18a and b depict the microstructure of an AlSi1.7 sample in the T6*e condition (T4:RT→3K/min→300°C) with diffraction pattern (Fourier transformation), respectively. As it is observed all precipitates are formed only in the fcc planes. A high resolution TEM image of a Si plate precipitate is depicted in Figure 5.18c, where partially coherent structure of a Si platelet precipitate is observed.

Slow cooled samples at 20K/min after solution treatment of the AlSi1.7 alloy (T4a, Figure5.19a) present globular and Si platelets of about 10-30 and 40-100nm, respectively. On the other hand, if the alloy is slowly cooled at 3K/min from ST (T4b), bigger globular Si precipitates (40-80nm) are found (Figure 5.19b), and still showing some orientation relationship of platelets.

Figure 5.19c depicts a TEM image after heating up to 420°C of an AlSi1.7 sample previously in the T4a condition. The microstructure of the material presents incoherent globular precipitates in a higher density, compared to T4a, but with similar sizes (20-40nm). These precipitates are dissolved after continuous heating at 3K/min to 460°C where only dislocations and loops (due to water quenching for sample observation) were observed (Figure 5.19d).

## 5.4 Thermal expansion

### 5.4.1 Unreinforced Al-Si alloys

The Percent Length Change (PLC) of AlSi1.1 and AlSi1.7 after different cooling rates from the solution treatment, i.e. T4 and T4a-c is depicted in Figures 5.20a and 5.21a, respectively. The length of both AlSi1.1 and AlSi1.7 samples after slow cooling at 1K/min from 540°C increases like pure Al. By increasing the cooling rate after solution treatment to 20K/min (T4a), a small deviation from pure Al for temperatures higher than 350°C is observed. This deviation is considerably increased for the water quenched samples between 200-300°C presenting an increment in the linear expansion of about 0.07 and 0.08% with respect to pure Al and rule of mixtures (99,6%Al+0.4%Si) for AlSi1.1 and AlSi1.7, respectively, producing a corresponding permanent length change.

The same behaviour was observed for both AlSi7 and AlSi12 alloys, presenting an important deviation in PLC curves for the T4 condition (0.08%) with respect the slowly cooled samples (detail in Figures 5.22 and 5.23) and rule of mixtures (94,3%Al+5.7%Si and 89,3%Al+10.7%Si, respectively).

The permanent length change of the alloys in the different initial condition can be seen at the end of the dilatometric curves at 540°C for all studied materials. There, the length change of about 0.05% can be read from the difference between the T4 test results and the reproducible curve obtained for the T4c condition. In comparison with ROM, the thermal expansion of the alloys approaches that of AlSi1.1 and AlSi1.7 at 540°C for all the studied thermal conditions. In case of AlSi7 and AlSi12 alloys, the linear thermal expansion of materials decreases about 0.06% in T4c and 0.08% in T4b,c for AlSi7 and AlSi12, respectively, compared to that of the ROM estimation.

| Alloy | CTE [ppm.K$^{-1}$] / Temperature [°C] | | | |
|---|---|---|---|---|
| | T4 | T4a | T4b | T4c |
| AlSi1.1 | 41.2 / 249 | 37.4 / 390 | 34.4 / 390 | 33.2 / 392 |
| AlSi1.7 | 45.9 / 245 | 35.3 / 375 | 32.3 /387 | 31.2 / 401 |
| AlSi7 | 33.9;32.4 / 242;298 | 30.5 / 398 | 28.2 / 390 | 28.2 / 390 |
| AlSi12 | 35.4 / 291 | 26.5 / 344 | 25.9 / 327 | 25.9 / 327 |

**Table 5.2**. Values of CTE maximum of studied alloys heated at 3K/min after T4 and slowly cooling from ST.

All studied alloys (in the T4 condition) present CTE peak of the suited materials amount 41.2, 45.9 and 35.4ppm.K$^{-1}$ around 249, 245 and 291°C for AlSi1.1, AlSi1.7 and AlSi12, respectively. The AlSi7 alloy presents a double CTE peak with maximum of 33.7 and 32,5ppm.K$^{-1}$ around 241 and 298°C, respectively. The temperature interval where the precipitation takes place is increased by the higher Si content starting at about 180°C for all studied alloys to 305, 320, 340 and 350°C for AlSi1.1, AlSi1.7, AlSi7 and AlSi12, respectively.

The AlSi1.1 material shows a CTE peak at about 380°C for T4a-c samples reaching values of 37.4, 34.4 and 33.2ppm.K$^{-1}$, respectively (Figure 5.20b). Contrarily to all studied alloys, the CTE of AlSi1.1 for all the studied thermal conditions is increased from 490°C up to the end of the measured temperature interval. The AlSi1.7 material (Figure 5.21b) present a CTE peak of 35.3ppm.K$^{-1}$ at 375°C in the T4a condition, which decreases and shifts slowly to higher temperatures for T4b (32.3 ppm.K$^{-1}$ and 387°C) and T4c (31.2ppm.K$^{-1}$ and 401°C), respectively. As observed in AlSi1.7, AlSi7 (Figure 5.22) presents a CTE peak after T4a of 30.5ppm.K$^{-1}$ at 395°C. No peak was observed for AlSi7 and AlS12 in T4b and T4c conditions where a maximum of about 28 ppm.K$^{-1}$ was observed at about 400°C. Similar behaviour was observed in AlSi12 where the CTE for all studied thermal conditions with a maximum of about 26 ppm.K$^{-1}$ at 350°C (see Figure 5.23).

The additional thermal expansion of T4 and slowly cooled samples is depicted in Table 5.3. Here, the additional PLC is obtained by the calculation of the area between the CTE peaks and the ROM estimation. The additional expansion in AlSi1.1 decreases about 14, 28 and 57% for T4a, T4b and T4c samples compared to that of the T4 condition. AlSi1.1 behaves similar showing a reduction in the residual expansion of 38, 63 and 75% in T4a, T4b and T4c conditions, respectively. On the other hand, the AlSi7 alloy presents an additional expansion of 0.02% in the T4a condition, which is comparable to that of AlSi1.1/1.7 in T4c.

| Alloy | Additional $\Delta l/l_0$ [%] | | | |
|---|---|---|---|---|
| | T4 | T4a | T4b | T4c |
| AlSi1.1 | 0.07 | 0.06 | 0.05 | 0.03 |
| AlSi1.7 | 0.08 | 0.05 | 0.03 | 0.02 |
| AlSi7 | 0.08 | 0.02 | - | - |
| AlSi12 | 0.08 | - | - | - |

**Table 5.3**. Differences in length change $\Delta l/l_0$ [%] with respect to: AlSi1.1 vs. pure-Al, AlSi1.7-12 vs. ROM, after water quenching and slowly cooling from ST.

In all the studied alloys the coefficient of thermal expansion shows an important reduction after the CTE peaks, compared to that of pure-Al (AlSi1.1) or ROM estimation (AlSi1.7/7/12). This drop is observed from 305, 320, 340 and 350°C for AlSi1.1, AlSi1.7, AlSi7 and AlSi12, respectively in the T4 condition and about 440-460°C for AlSi1.1/1.7 in T4,b,c conditions and AlSi7 in T4a. Also samples of AlSi7 in T4b,c and AlSi12 in T4a,b,c present a reduction of the CTE compared to ROM estimation but starting at a lower temperatures (400, 330-380°C, respectively).

### 5.4.2 Short Fibre Reinforced Materials

The thermal expansion of the composite materials in the plane of fibre orientation and in the transverse direction is depicted in Figures 5.24a-5.27a. The AlSi7/$Al_2O_3$/20s (v1) material shows a percent linear change significantly below that of the unreinforced matrix, but complementarily increasing in the transverse direction. 20 vol.% alumina fibres in AlSi7 decrease significantly the in plane expansion to half of that of AlSi7 from RT to 500°C, whereas the transverse expansion increases by about 30% with respect to the unreinforced matrix (Figure 5.25a).

The expansion of the T4c condition of all the alloys proceeds relatively linearly, while the expansion rate of the AlSi7/$Al_2O_3$/20s composite, i.e. the coefficient of thermal expansion, changes with temperature. Figure 5.25a shows an additional expansion close to 300°C increasing with the preceding cooling rate for both parallel and in plane directions. The difference in length change of the AlSi7/$Al_2O_3$/20s sample in the fibre plane between T4 and T4c condition up to 300°C amounts to about 0.07%, similar to that observed for the unreinforced alloy. The corresponding length change produced after the first heating of AlSi7/$Al_2O_3$/20s material in T4 condition in the dilatometer amounts to a linear shrinkage of about 0.15% in the fibre plane compared with T4c.

The CTE(T) curves of AlSi7/$Al_2O_3$/20s submitted to different cooling rates from solution treatment temperature are depicted in Figure 5.25b. The composite material in the fibre plane as well as transverse exhibits a CTE peak in T4 condition between 200-320°C, amounting 20.1 and 46.8ppm.$K^{-1}$, respectively. This effect disappears after slower cooling of 1, 3 and 20K/min from ST.

The AlSi1.1/$Al_2O_3$/20s material and the high Si content versions AlSi12/$Al_2O_3$/20s and AlSi18/$Al_2O_3$/20s exhibit a similar behaviour as the reinforced AlSi7 alloy. The expansion vs. temperature (PLC) of the mentioned materials is depicted in Figures 5.24a, 5.26a and 5.27a, respectively. Both PLC curves in transverse and in plane directions decrease with increasing the Si content i.e. at 520°C, showing an permanent length change of 1.93, 1.72, 1.60 and 1.45% (in the transverse direction) in the T4c condition for SFRM1.1, 7, 12 and 18, respectively. Contrarily, the length change for samples within the fibre in plane alignment remains constant at only ~0.6-0.7% (at 520°C) in all studied short fibre reinforced composites.

The composites present an additional expansion between 200 and 300°C in the T4 condition for both parallel and in plane directions. This is well observed by the calculation of the CTE (Figures 5.24b,c-5.27b,c) amounting 54.6, 46.8, 43.3 and 37.1ppm.$K^{-1}$ in transverse for SFRM1, 7, 12 and 18 composites, respectively, and about 20ppm.$K^{-1}$ in planar samples of studied reinforced materials.

The modelled CTE by Schapery of AlSi7-12-18 alloys and AlSi7-12/$Al_2O_3$/20s composite materials is depicted in Figure 5.28. The estimated CTE of the AlSi7 alloy shows the higher values amounting about 21 and 29.5ppm.$K^{-1}$ at 50 and 500°C, respectively. Here, a small difference of only 0.2ppm.$K^{-1}$ is observed between the upper and lower bounds of the model for the whole temperature interval. By increasing the Si content, the modelled CTE decreases at about 20 and 28ppm.$K^{-1}$, and 18.5 and 26.5ppm.$K^{-1}$ at 50 and 500°C for AlSi12 and AlSi18, respectively. The difference between upper and lower bounds is increased amounting 0.3 and 0.4ppm.$K^{-1}$ for AlSi12 and AlSi18, respectively. The modelled lower bounds of AlSi7-12/$Al_2O_3$/20s composite materials exhibit the lowest CTE values amounting 16,6 and 19ppm.$K^{-1}$, and 16,2 and 18.5ppm.$K^{-1}$ at 50 and 250°C, respectively. Contrarily to the unreinforced alloys, the difference with respect the upper bounds show higher (~1.4ppm.$K^{-1}$) reaching CTE values of 18-20.8ppm.$K^{-1}$ and 17.5-20ppm.$K^{-1}$ between 50-250°C for SFRM7 and SFRM12, respectively. Above 250°C, the thermoelastic models are not relevant because of the plastification of the matrix.

## 5.5 Calorimetry

### 5.5.1 Differential Scanning Calorimetry

Figure 5.29 depicts several DSC runs of AlSi1.7 alloy at different thermal conditions measured at 3 and 5K/min. Water quenched samples of AlSi1.7 (T4) present an exothermic effect between 180-300°C (heating rate = 5K/min), which is considerably shifted to higher temperatures by decreasing the cooling rate from ST to about 330-460°C, 340-440°C for T4a and T4b conditions, respectively. On the other hand, the magnitude of this exothermic effect decreases with decreasing the cooling rate from 1.44x10$^{-2}$W/g in T4, to 5.3x10$^{-3}$ and 0.8x10$^{-3}$W/g in T4a and T4b conditions, respectively. No exothermic effect was observed in AlSi1.7 samples in the T4c condition (slow cooled at 1K/min from ST temperature). All studied thermal conditions exhibit an endothermic reversion after the exothermic effect, starting at 300, 460, 440 and 420°C for T4, T4a, T4b and T4c conditions, respectively. This effect was observed up to the end of the measured temperature interval.

The magnitude of the exothermic effects is reduced to 0.9x10$^{-2}$ (155-330°C) and 0.5x10$^{-2}$W/g (280-330°C) in T4 and T4a, respectively, if a heating rate of 3K/min is applied. In this case, the endothermic effect after the corresponding exothermic peak start at 380 and 450°C for the T4 and T4a conditions, respectively.

Figure 5.30 depicts DSC measurements performed in AlSi1.1 at a heating rate of 20K/min after different thermal conditions, where a similar trend as in AlSi1.7 was observed. The alloy presents an exothermic effect between 200 and 330°C in the T4 condition which is displaced to higher temperatures for slow cooled samples in a temperature interval between 310, 330, 340-460°C for T4e (cooled at 300K/min), T4a (20K/min) and T4d (5K/min) conditions. The peak maximum is also displaced to higher temperatures with decreasing cooling rate at 288, 420, 428 and 434°C and amounting 8.7x10$^{-2}$, 2.0x10$^{-2}$, 1.3x10$^{-2}$ and 1.0 x10$^{-2}$W/g for T4, T4e, T4a and T4d thermal conditions. In all cases, the exothermic effect is followed by an endothermic effect, but contrarily to AlSi1.7, finishing at about 560°C for all studied thermal conditions.

The AlSi12 alloy shows a small exothermic effect between 260-370°C after heating at 20K/min in DSC apparatus (Figure 5.31). After that continuous dissolution of the Si phase is observed in the corresponding thermogram. The alloy in the T4a condition only present an endothermic effect starting at ~300°C up to the end of the measured temperature interval. In both thermograms the position of the base line is not clear.

DSC runs measured at different heating rates in AlSi1.1-alloy in the T4 condition are depicted in Figure 5.32. As a consequence of increasing the heating rate, the exothermic effect is displaced to higher temperatures at 248.3, 258.7, 281.3, 303.3 and 326.7°C during testing at 5, 10, 20, 50 and 100K/min, as well as the magnitude of exothermic and endothermic effect rates.

### 5.5.2 Isothermal calorimetry

Isothermal DSC results of AlSi1.1 and AlSi12 alloys after T4 condition are depicted in Figure 5.33. The heat evolution of AlSi1.1 differs from that of the AlSi12 alloy. AlSi1.1 presents 2 overlapped exothermic effects (A and B) during isothermal heating at 176.5°C representing precipitation. On the other hand, the AlSi12 alloy presents only an exothermic effect measured during the whole testing interval. It should also be mentioned that curves are quantified for times higher that 30min (see 4.4.2.2). Therefore, both curves are presented only for times higher than 0.5h.

## 5.6 Small Angle Neutron Diffraction

The scattering curves of AlSi1.1 in the T4 condition shows roughly similar results to that of the T4a condition (Figure 5.34) with a detachment of both curves at intermediate scattering vector values (0.03-0.6nm$^{-1}$).

Figure 5.35 depicts the evolution of the cross section of AlSi1.1 in the T4 condition and after heating at 3K/min to 200 (T6*b) and 250°C (T6*c). The scattering curves of studied thermal conditions are very similar but show an inflection point at a value of $q$ equal to 0.08nm$^{-1}$. Therefore, the T6*c curve shows somewhat higher cross section values than T6*b and T4 ones for $q < 0.08$nm$^{-1}$, and is lower to that of the T6*b and T4 condition for higher scattering vector values.

The cross section vs. scattering vector of T4a and subsequently heated AlSi1.1 samples (T7*e, T7*f and T7*g) are presented in Figure 5.36. The scattering curves of the T4a and T7*g conditions are similar while that of the T7*e and T7*f increase significantly their cross section values from $q > 0.1$nm$^{-1}$. Comparing the two last ones, the T4a sample heated up to 370°C (T7*f) shows a slightly higher cross section than the heated up to 300°C, between 0.7nm$^{-1}$ < $q$ < 2.5 nm$^{-1}$.

## 5.7 Mechanical properties

### 5.7.1 Hardness

#### 5.7.1.1 Influence of thermal treatment on the hardness of AlSi1.1

Figure 5.37 shows the evolution of the Brinell hardness in the AlSi1.1 alloy after different thermal conditions. The lowest values were observed in the T4 (28HB 5) and T6b (29HB 5). During heating at 3 K/min from the solution treated condition, the hardness is increased up to 32.5 and 39HB 5 at 200 (T6*b) and 300°C (T6*d), respectively. An improvement on the hardness was also observed by heating of the alloy during 10 hours at 200°C (T6c).

### 5.7.1.2 Influence of Si spheroidization on the rigidity of SFRMs

The hardness of the AlSi7/$Al_2O_3$/20 (v1) composite material, its unreiforced matrix and deep etched Si-$Al_2O_3$ network are displayed as a function of solution treatment time in Figure 5.38. A continuous decrease of the hardness by approximately 15% takes place for the unreinforced matrix with increasing the solution treatment time up to 4h. Contrarily to the AlSi7 matrix, the composite presents a slight increase of the hardness up to 20min of solution treatment time. This is in qualitative agreement with the results obtained for the Si/$Al_2O_3$ network where a maximum is also observed at the same ST time.

The Brinell hardness of AlSi1.1/$Al_2O_3$/20s, AlSi12/$Al_2O_3$/20s, AlSi18/$Al_2O_3$/20s and that of the second version of AlSi7/$Al_2O_3$/20s after different solution treatment times at 540°C are presented in Figure 5.39. The hardness of AlSi1.1/$Al_2O_3$/20s is almost constant at 71HB for the whole exposure time interval. The hardness of SFRM7 (v2) material decreases slowly from 93HB in the as cast condition to 90HB (3.2% lower) after 4h of solution treatment at 540°C but is significantly higher than that of version 1. AlSi12/$Al_2O_3$/20s presents similar behaviour amounting 92HB in as cast, but decreasing ~5.5% (85HB) after 540°C/4h. The AlSi18/$Al_2O_3$/20s material presents the highest values of hardness in the cast condition (103HB). Contrarily to SFRM7(v2) and SFRM12, the rigidity of the material decreases significantly (12% compared to as cast) after 20min of solution treatment approaching the HB values of the last ones.

Figure 5.40 depicts the Brinell hardness of AlSi7 alloy and both versions of the AlSi7/$Al_2O_3$/20s composite material. The distance between the Si particles in the unreinforced alloy is increased from 1.2 to 3.7µm after 4 hours of solution treatment in comparison with the as cast condition. The hardness of the alloy decreases linearly showing a slope of about –2.7HB/µm. The second version of SFRM7 composite presents smaller Si interparticle distance values than its unreinforced matrix, in the range between 0.9µm in as cast and 1.9µm after 540°C/4h, respectively. Like in AlSi7, the hardness of the composite decreases linearly with increasing interparticle distance with a similar softening slope (-3,1HB/µm). The 2nd version of AlSi7/$Al_2O_3$/20s composite presents much higher interparticle distance values (between 2.2 and 3.7µm in AC and T4, respectively) compared with the 1st composite version. Here, due to the less undercooling after processing of high volume mould, Brinell hardness values of the as cast condition are not comparable to water quenched samples where internal stresses are increased. After 20minutes of solution treatment, the hardness of the composite decreases almost linearly with a softening slope like in AlSi7 and SFRM7 v2. It is important to note that the dendrite arm spacing of the composite (~25µm) is 150% higher than in the 1st version (10µm). Therefore, the difference in hardness levels may be related to this observation.

### 5.7.2 Young's Modulus

The measured Young's modulii between 25-300°C of the fibre reinforced alloys (in the in fibre plane direction) and AlSi-alloys is depicted in Figure 5.41. The E modulus of the AlSi12 alloy is ~22% lower than its reinforced version (both in as cast). After solution treatment (540°C/4h), the Young modulus of the alloys is reduced slightly (~2%) from 76.3 in as cast to 74.8GPa. The same behaviour is observed in the AlSi7 alloy, achieving values of the elastic modulus of 73.8 and 72.2GPa in AC and after solution treatment at 540°C during 4h, respectively.

The E modulus of AlSi18/$Al_2O_3$/20s shows the highest for the whole temperature interval, reaching 106 and 91GPa at RT and 300°C, respectively. After solution treatment at 540°C the E modulus decreases dramatically to 99GPa at RT and 85GPa at 300°C, approximately 6% lower than before. The AlSi12/$Al_2O_3$/20s material exhibits a similar behaviour as the high Si content version, with lower E values for the whole measured interval. The highest E values were observed in the as cast condition, amounting 97 and 82GPa at room temperature and 300°C, respectively. The solution treated version (540°C/4h) decreases its stiffness ~5% for the whole temperature interval, reaching 93 and 80GPa at 25 and 300°C, respectively. In contrast with the high Si content composites, AlSi1.1/$Al_2O_3$/20s presents similar E values in the as cast condition and for the solution treated sample going to about 91 and 80GPa in RT and 300°C, respectively. AlSi12/$Al_2O_3$/20s after solution treatment shows the same measured E values as AlSi1.1/$Al_2O_3$/20s in both thermal conditions.

#### 5.7.2.1 Estimation of Young's modulus of unreinforced and reinforced matrices

The E modulus of AlSi1.1, AlSi7, AlSi12 and AlSi18 matrices and reinforced versions was calculated following the shear lag treatment. In the case of the unreinforced alloys, the Si was treated as the reinforcing phase. The Young's modulus of the alloys and composite materials was estimated in the as-cast condition and after 4h of solution treatment at 540°C. The microstructural parameters of the Si phase as well as the $\alpha$-Al ones used in this calculation are depicted in Table 5.4 and where obtained from microstructural characterization of SEM and LOM images. The composite E modulus was calculated from the unreinforced matrix estimation and that of the alumina short fibres. Here an average fibre length L and radius $r_0$ of 68 and 2µm, respectively, were used for the calculation of the aspect ratio *s*. Figure 5.42 depicts the microstructure of the eutectic phase in AlSi7,12,18/$Al_2O_3$/20s composites used for the calculation of the microstructural parameters presented in Table 5.4.

| $\mathbf{E_{Al}}$=69.2GPa, $\mathbf{E_{Si}}$=162.5GPa, $\boldsymbol{\nu_{Al}}$=0.33 [King, 1998] | | | | | | | | |
|---|---|---|---|---|---|---|---|---|
| Matrix | *L* [µm] | | *r₀* [µm] | | *s* | | *E* [GPa] | |
| | AC | 540°C/4h | AC | 540°C/4h | AC | 540°C/4h | AC | 540°C/4h |
| AlSi7 | 3 | 5.3 | 0.3 | 0.8 | 10 | 6.6 | 74.1 | 72.8 |
| AlSi12 | 9 | 5 | 0.5 | 0.9 | 18 | 5.6 | 79.8 | 74.9 |
| AlSi18 | 9 | 5.3 | 0.6 | 1 | 15 | 5.3 | 84.7 | 78.3 |

**Table 5.4.** Microstructural parameters of Si inclusions in AlSi matrices for the modelling of the E modulus in the studied SFRMs.

### 5.7.3 Compression tests on SFRMs

Figure 5.43 summarizes the maximum strength obtained from compression tests of the studied composites materials. Typical stress–strain curves from compression tests (parallel to random fibre distribution) in AlSi1.1/$Al_2O_3$/20s in T6s (T4 + 300°C/2h) and AlSi7/$Al_2O_3$/20s, AlSi12/$Al_2O_3$/20s and AlSi18/$Al_2O_3$/20s samples in the T5 condition (T1 + 300°C/2h) are shown in Figure 5.44. Generally, the strength of the alloy increases with increasing the Si content, amounting a maximum values of 132, 174, 169 and 214MPa for 1.1, 7, 12 and 18% of Si, respectively. The AlSi7 and AlSi12 matrices yield the same flow curves. All curves show similar trends presenting a pronounced softening after reaching maximal strength values at about 0.04% true strain, with slopes of -9.3x$10^4$, -7.0x$10^4$ and –11.5x$10^4$MPa for AlSi7/$Al_2O_3$/20s, AlSi12/$Al_2O_3$/20s and AlSi18/$Al_2O_3$/20s, respectively.

Similar behaviour but with lower strength values are observed for compression tests of composites samples with perpendicular fibres orientation to the compression load (Figure 5.45). In this case, the maximal strength reaches 107, 160, 152 and 183MPa for SFRM1.1, 7, 12 and 18, respectively. The softening effect is also attenuated getting slopes of –3.8x$10^4$, -8.9x$10^4$, -5.6 x$10^4$ and –8.6 x$10^4$MPa for AlSi1.1/$Al_2O_3$/20s, AlSi7/$Al_2O_3$/20s, AlSi12/$Al_2O_3$/20s and AlSi18/$Al_2O_3$/20s, respectively.

The stress-strain curves of AlSi1.1/$Al_2O_3$/20s samples with perpendicular random fibre plane show similar in both T5 and T6s conditions. In case of AlSi7/$Al_2O_3$/20s the effect of solution treatment in the maximum strength is accentuated by decreasing about 13.1 and 19.5% for perpendicular (Figure 5.47) and parallel (Figure 5.46) random fibre samples, respectively. Solution treated samples of AlSi12/$Al_2O_3$/20s and AlSi18/$Al_2O_3$/20s materials present similar trends as AlSi7/$Al_2O_3$/20s, decreasing the maximum strength after solution treatment + dimensional stabilization (T6s) by 21.1 and 28.4%, and by 19.1 and 21.5% for perpendicular and parallel random plane fibres, and AlSi12/$Al_2O_3$/20s (Figures 5.48 and 5.49) and AlSi18/$Al_2O_3$/20s (Figure5.50 and 5.51), respectively.

### 5.7.4 Thermal cycling creep tests on SFRMs

Figure 5.52 depicts the measured true strain and calculated strain rate from thermal cycling creep tests performed on AlSi7/$Al_2O_3$/20s, AlSi12/$Al_2O_3$/20s and AlSi18/$Al_2O_3$/20s composite materials in as cast. For both 40 and 60MPa constant loads, AlSi18/$Al_2O_3$/20s exhibits the highest thermal cycling life achieving 1265 and 99 cycles, respectively (Figure 5.52b,d). Both AlSi7/$Al_2O_3$/20s and AlSi12/$Al_2O_3$/20s composites materials behave similar achieving 508 and 525 cycles with a load of 40MPa and 91, 82 cycles at 60MPa, respectively. In all studied composite materials, the elongation at fracture decreases with increasing the load from 0.16-0.21 at 40MPa to 0.08-0.12 at 60MPa.

The strain rate of AlSi18/$Al_2O_3$/20s composite (Figure 5.52a,c) shows to be the lowest for the whole testing interval and both loads achieving a minimum value of only 4.8x$10^{-7}$$s^{-1}$ after 306 cycles under a load of 40MPa, and 6.2x$10^{-6}$$s^{-1}$ after 10 cycles at 60MPa. These values are increased with decreasing the Si content to $2.0x10^{-6}s^{-1}$ (44 cycles) and $1.5x10^{-5}s^{-1}$ (23 cycles) for samples of AlSi7/$Al_2O_3$/20s composite tested at 40 and 60MPa, respectively. Although the AlSi12/$Al_2O_3$/20s exhibits a minimum strain rate comparable to the of the reinforced AlSi18 alloy for both 40 and 60MPa load test conditions ($5.7x10^{-7}$ and 1.0 $x10^{-5}s^{-1}$, respectively), the strain rate of the composite seems to be generally higher than the AlSi7/$Al_2O_3$/20s material for the tested time interval.

The measured true strain and calculated strain rate from thermal cycling creep tests of solution treated composites is depicted in Figure 5.52. For both 40 and MPa loads, the thermal cycling life is decreased considerably after solution treatment achieving only 192, 162 and 179 cycles, and 38, 49 and 22 cycles for AlSi7/$Al_2O_3$/20s, AlSi12/$Al_2O_3$/20s and AlSi18/$Al_2O_3$/20s, respectively (Figure 5.53b,d). On the other hand, the ductility of the investigated composites in increased by 25-30% in comparison with samples tested in the as cast condition (between 0.21-0.27 and 0.10-0.15 for mechanical loads of 40 and 60MPa). No big differences is observed in the minimal strain rate of the different solution treated composites, where values of $4.2x10^{-5}$, $5.7x10^{-5}$ and $3.3x10^{-5}s^{-1}$,and $9.3x10^{-6}$, $1.7x10^{-5}$ and $4.0x10^{-6}s^{-1}$ are registered for AlSi7/$Al_2O_3$/20s, AlSi12/$Al_2O_3$/20s and AlSi18/$Al_2O_3$/20s composites, respectively (Figure 5.53a,c).

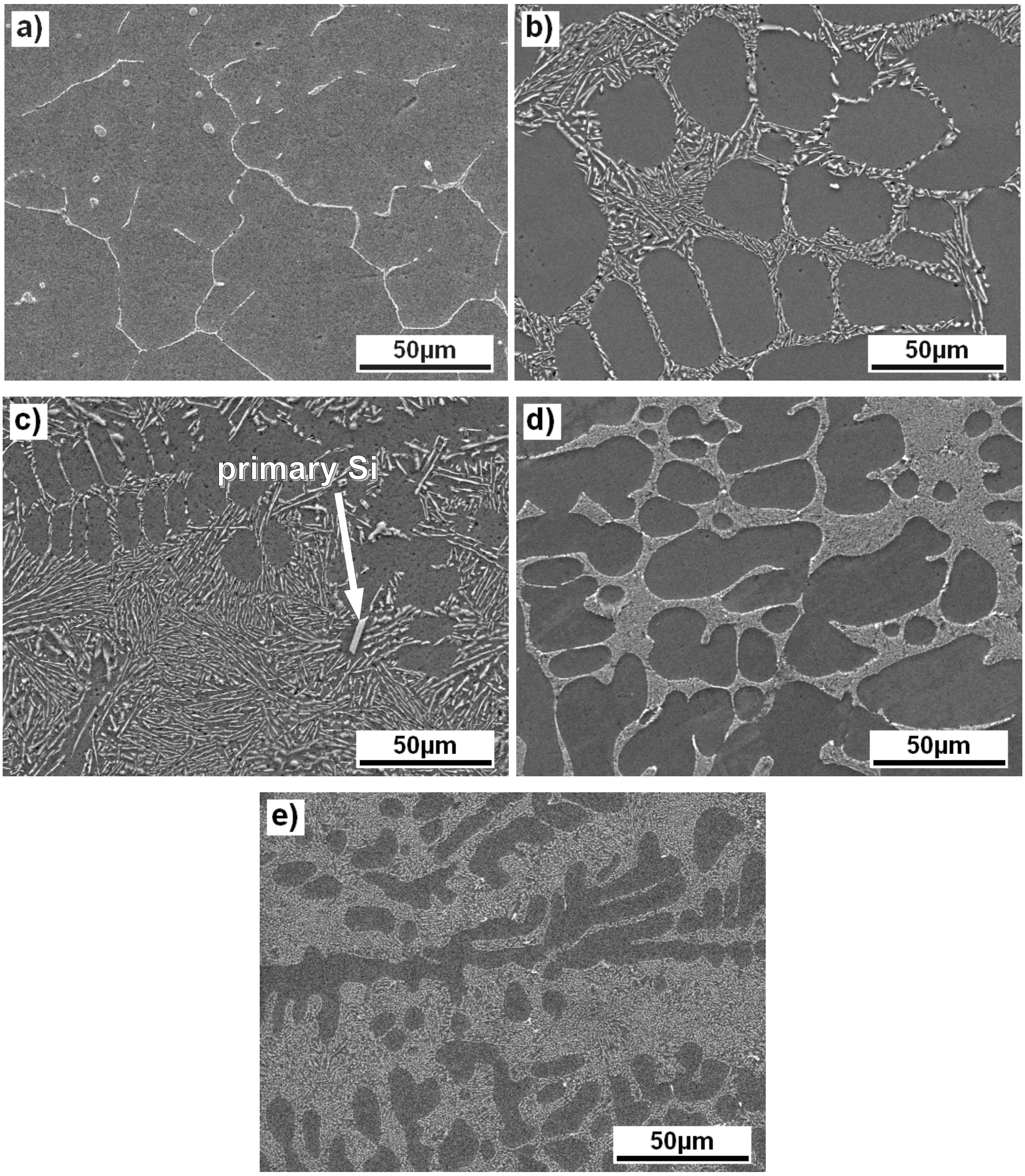

**Figure 5.1.** Microstructure of a) AlSi1.7, b) AlSi7, c) AlSi12, d) AlSi7Sr and e) AlSi12Sr in the as cast condition (white: Si eutectic structure, grey: $\alpha$-Al).

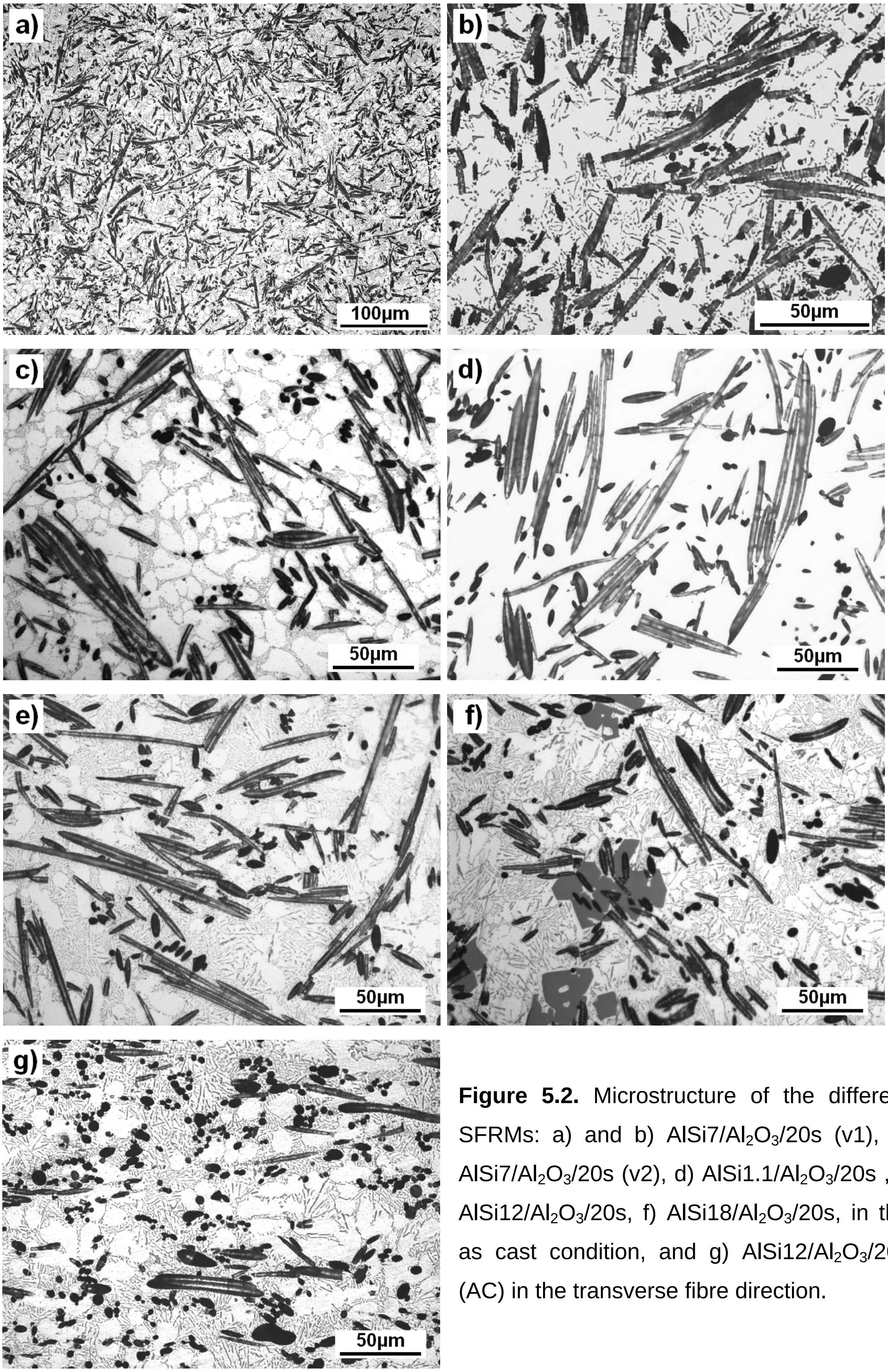

**Figure 5.2.** Microstructure of the different SFRMs: a) and b) AlSi7/$Al_2O_3$/20s (v1), c) AlSi7/$Al_2O_3$/20s (v2), d) AlSi1.1/$Al_2O_3$/20s ,e) AlSi12/$Al_2O_3$/20s, f) AlSi18/$Al_2O_3$/20s, in the as cast condition, and g) AlSi12/$Al_2O_3$/20s (AC) in the transverse fibre direction.

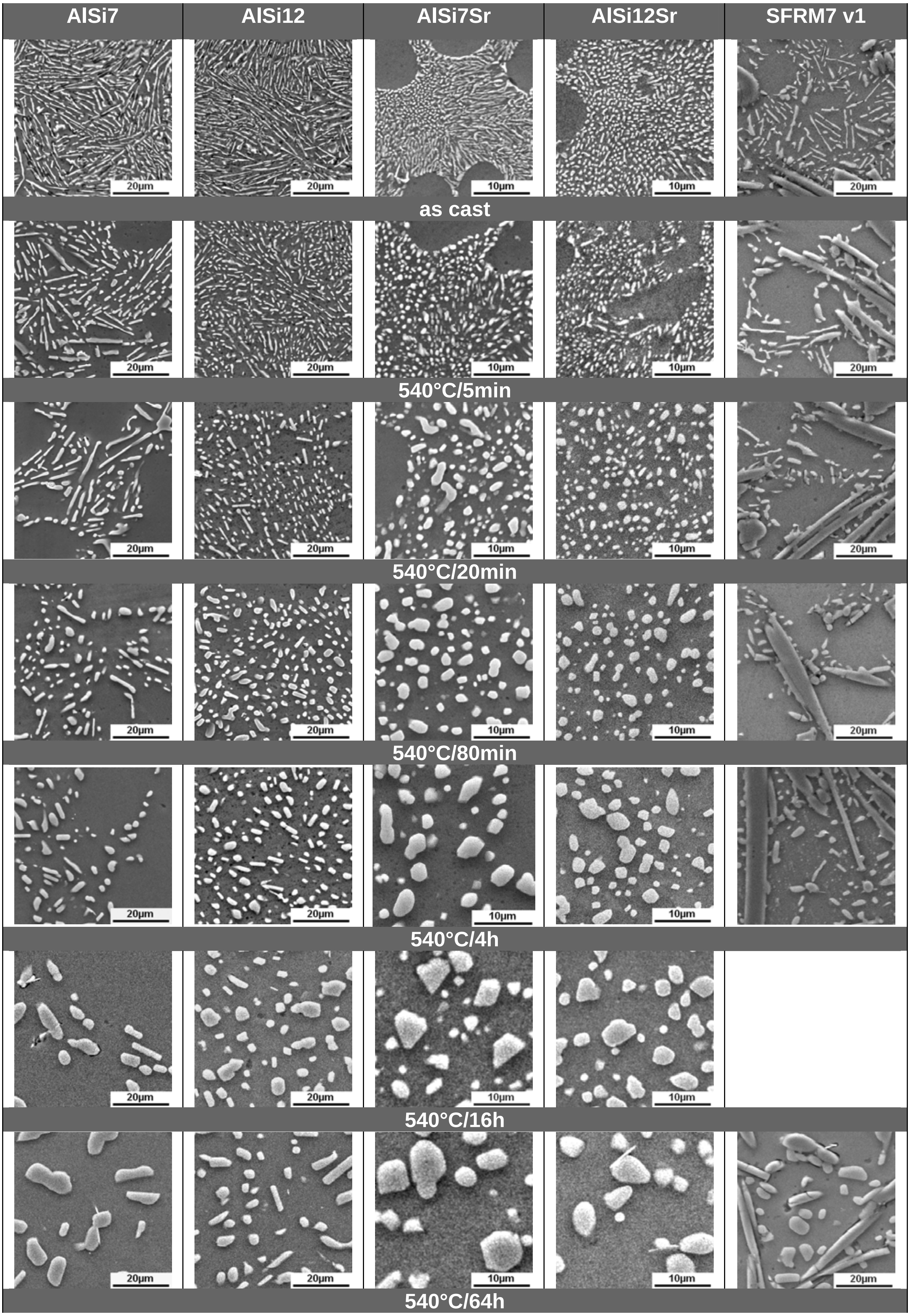

**Figure 5.3.** Chronology of Si spheroidization on studied materials.

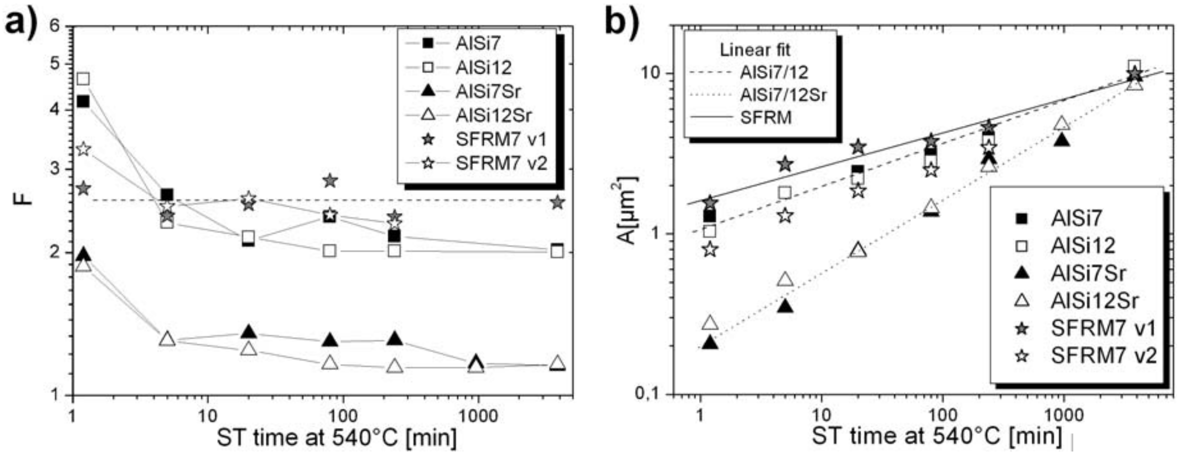

**Figure 5.4.** Quantitative analysis of spheroidization and coarsening of the Si phase:

a) shape factor F, b) representative mean area A.

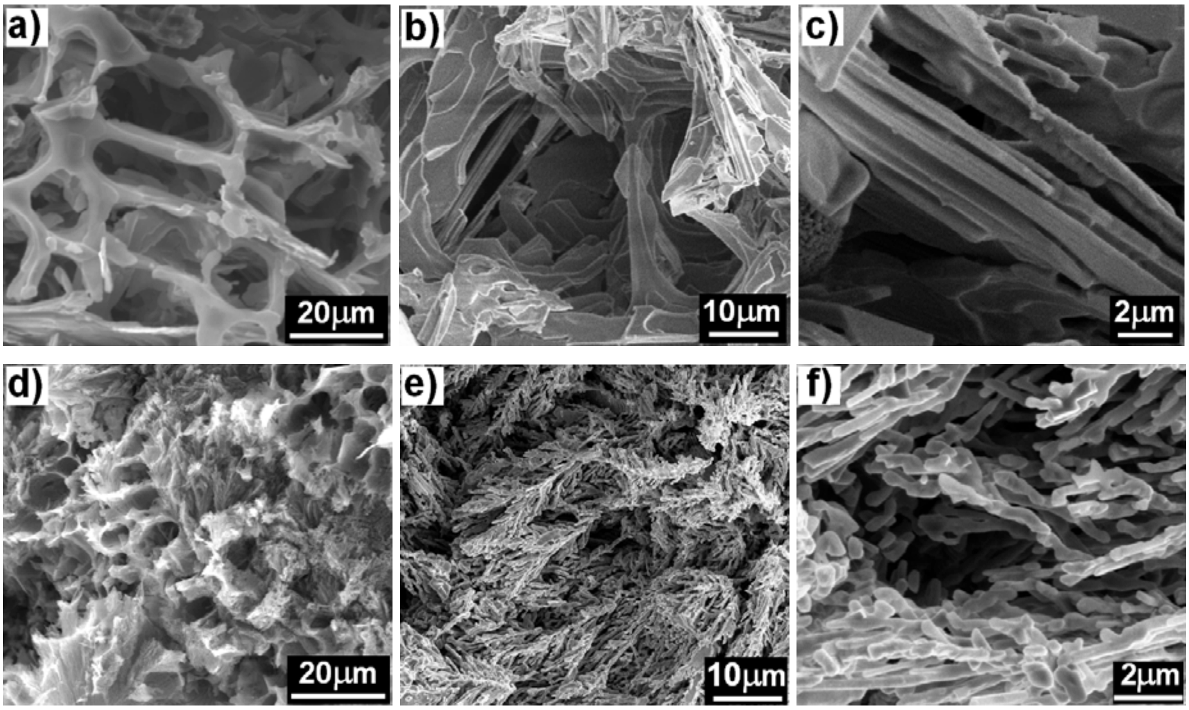

**Figure 5.5.** Si structure obtained after dissolution of the $\alpha$-Al in as cast AlSi7: a,b) remaining interdendritic arms, c) lamellar Si in the cell walls; in as cast AlSi7Sr: d,e) coral walls, f) fibrous Si structure within the cell walls.

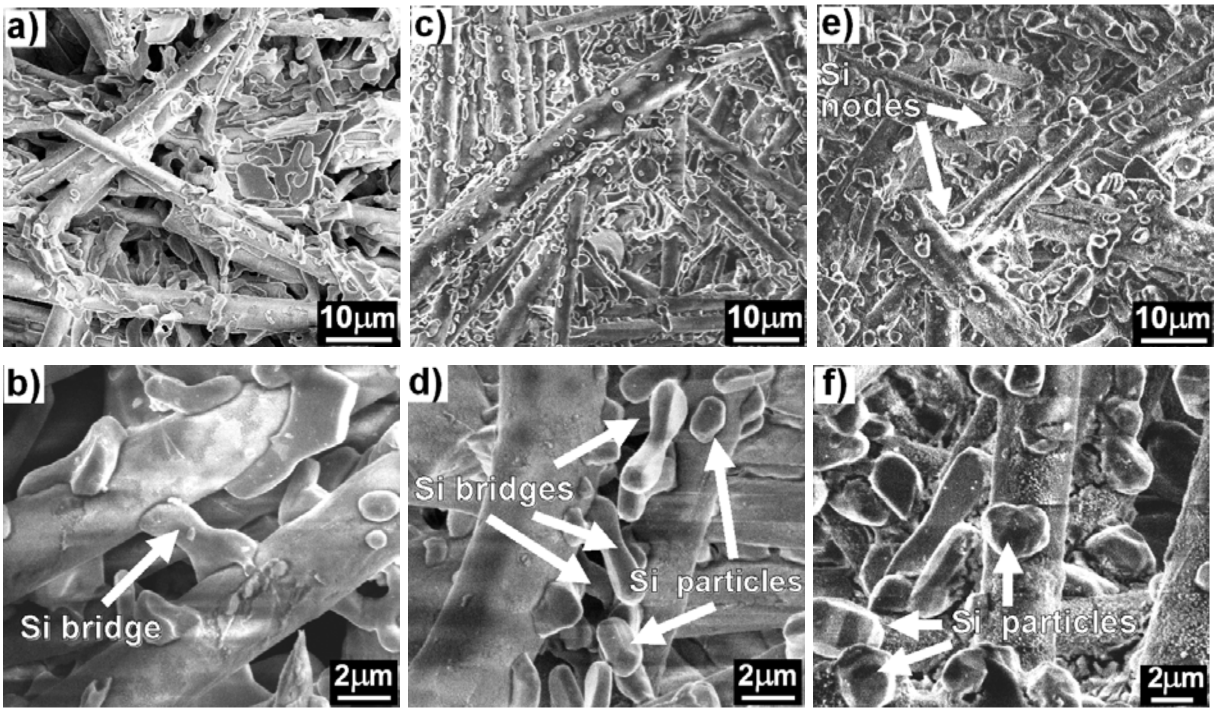

**Figure 5.6.** Microstructure of extracted Si-$Al_2O_3$ networks from AlSi7/$Al_2O_3$/20s (version 1) in: a,b) as cast, and after different solution treatment times at 540°C: c,d) 20min., e,f) 4h.

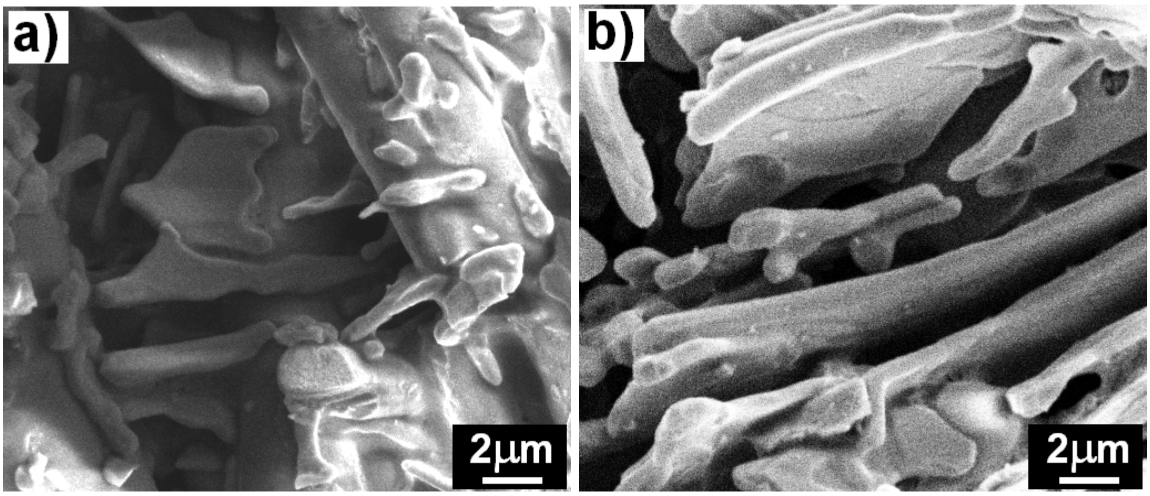

**Figure 5.7.** Structure of Si-$Al_2O_3$ network from AlSi7/$Al_2O_3$/20s (version 2) in as cast showing a) Si plates connected to the fibres and b) interconnected Si in a free-fibre zone.

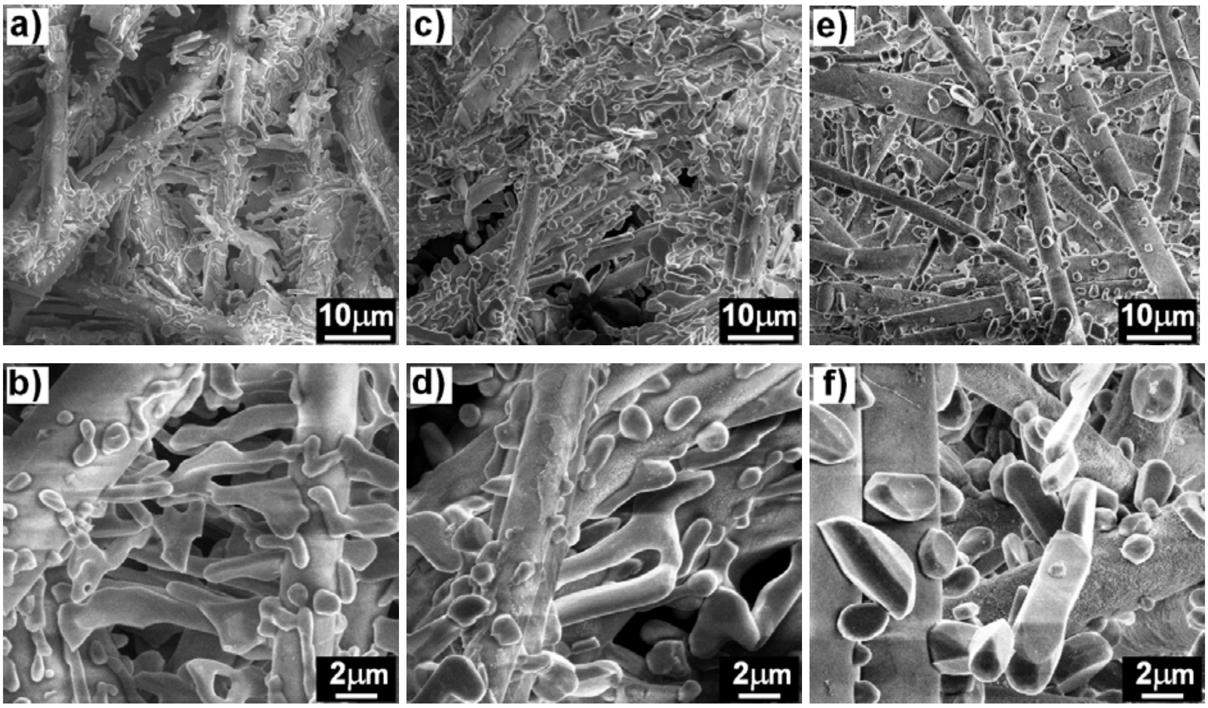

**Figure 5.8.** Microstructure of extracted Si-$Al_2O_3$ networks from AlSi12/$Al_2O_3$/20s in: a,b) as cast, and after different solution treatment times at 540°C: c,d) 20min., e,f) 4h.

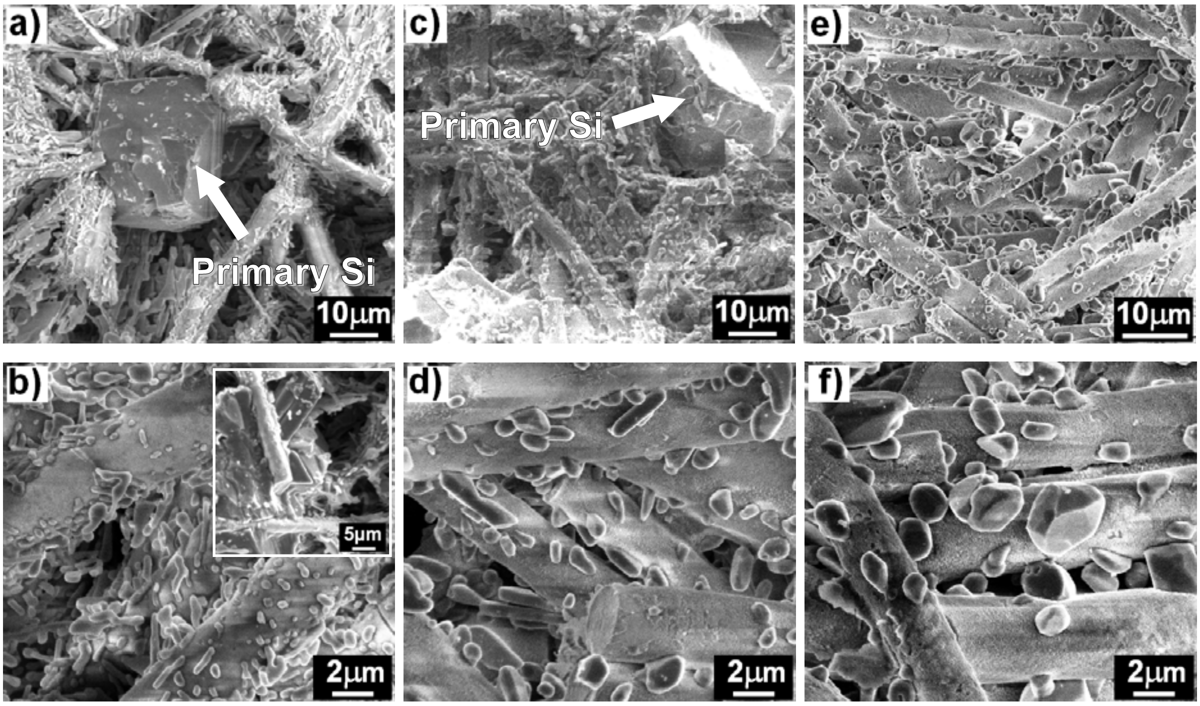

**Figure 5.9.** Microstructure of extracted Si-$Al_2O_3$ networks from AlSi18/$Al_2O_3$/20s in: a,b) as cast, and after different solution treatment times at 540°C: c,d) 20min., e,f) 4h.

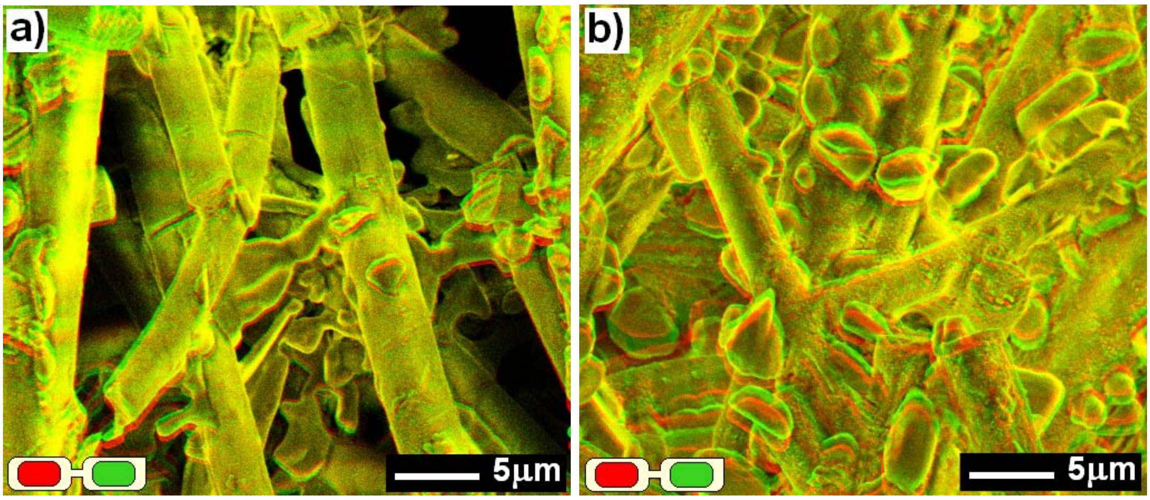

**Figure 5.10.** 3D microstructure of Si-$Al_2O_3$ network from AlSi7/$Al_2O_3$/20s (v1) in a) as cast condition and b) after 540°C/4h (Stereo images: Use red-green glasses!).

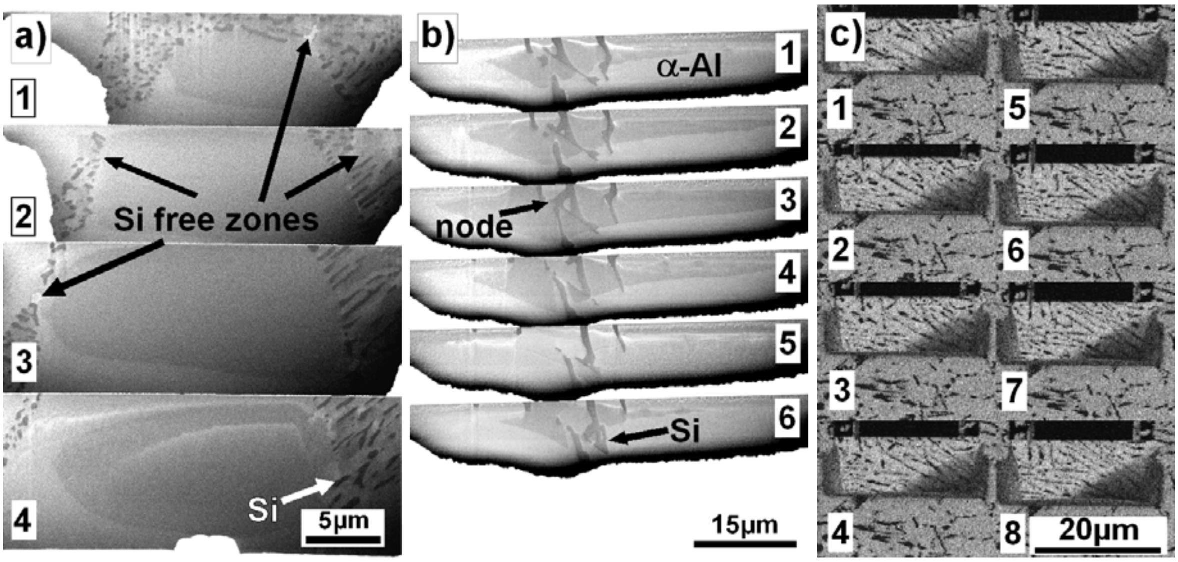

**Figure 5.11.** Series of parallel 2D-FIB cross-sections of a) AlSi7Sr (3.94µm spacing), b) AlSi7 (800nm spacing) and c) AlSi12 (310nm spacing). a) and b) SEM micrographs; c) EDX-map of Si (tilt: 52°).

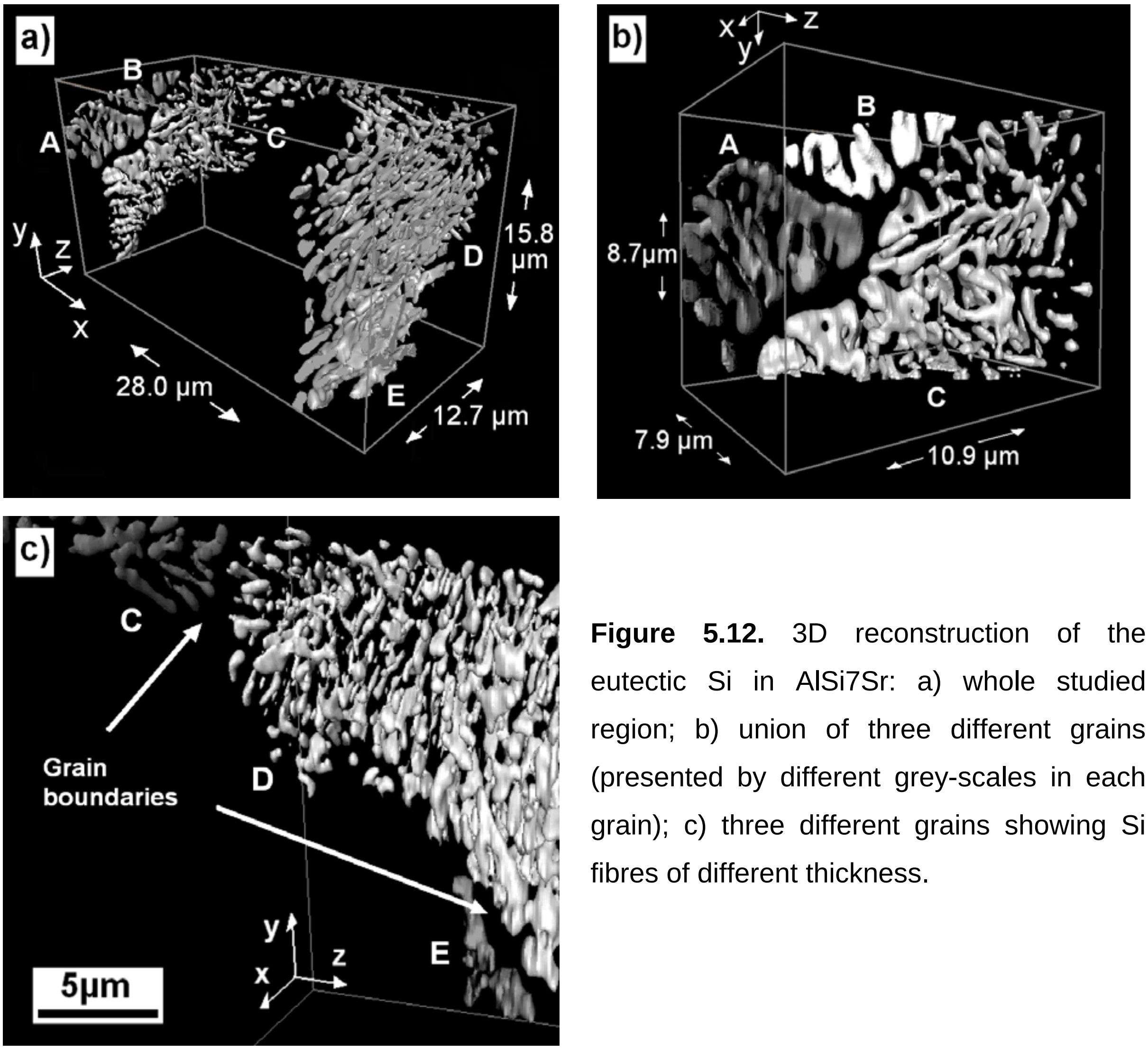

**Figure 5.12.** 3D reconstruction of the eutectic Si in AlSi7Sr: a) whole studied region; b) union of three different grains (presented by different grey-scales in each grain); c) three different grains showing Si fibres of different thickness.

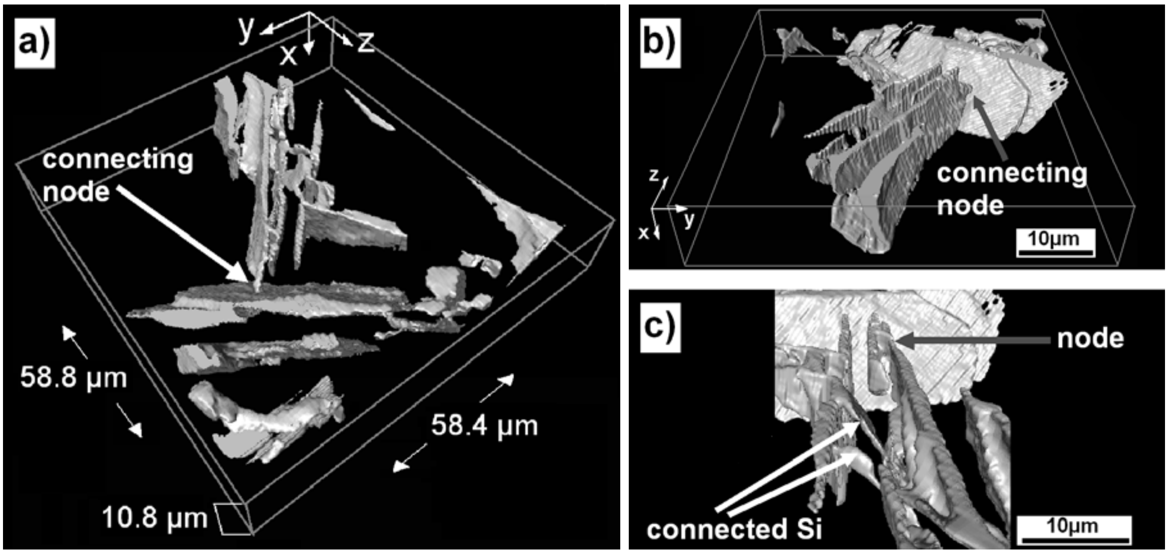

**Figure 5.13.** 3D reconstruction of lamellar Si in unmodified AlSi7 for a,b) the whole studied region at different observation angle and c) connecting nodes.

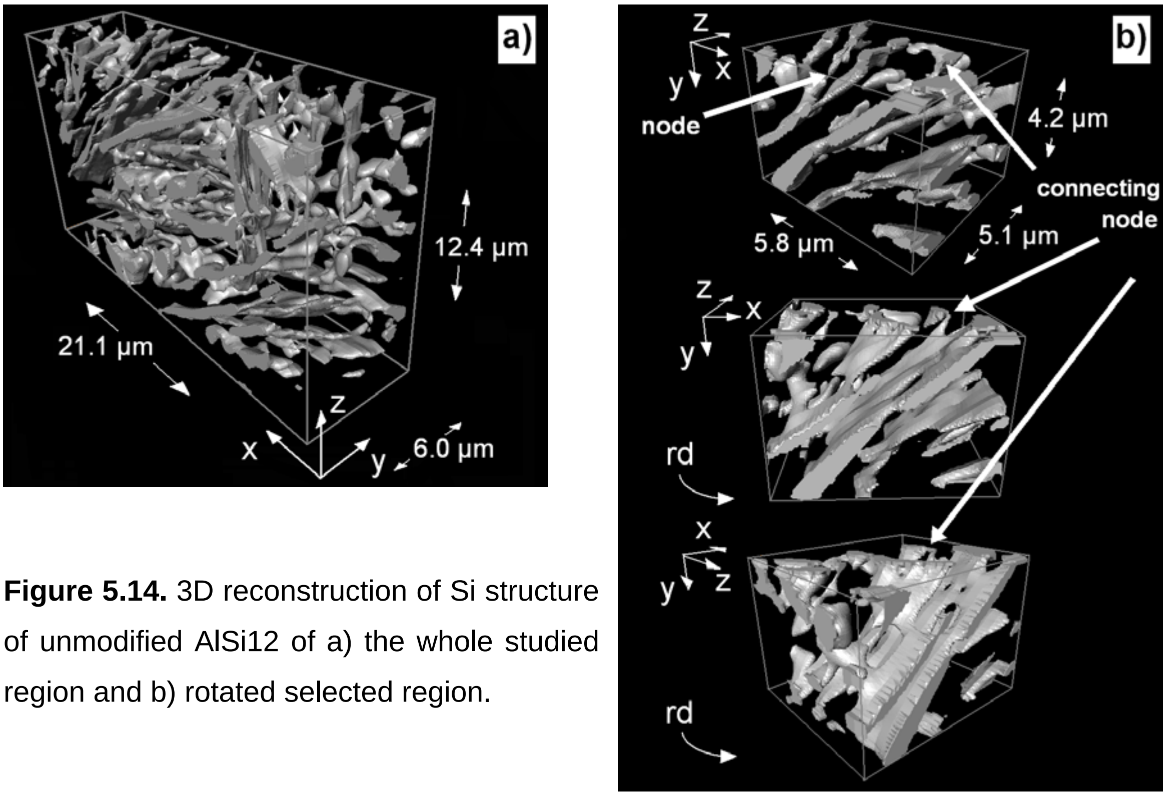

**Figure 5.14.** 3D reconstruction of Si structure of unmodified AlSi12 of a) the whole studied region and b) rotated selected region.

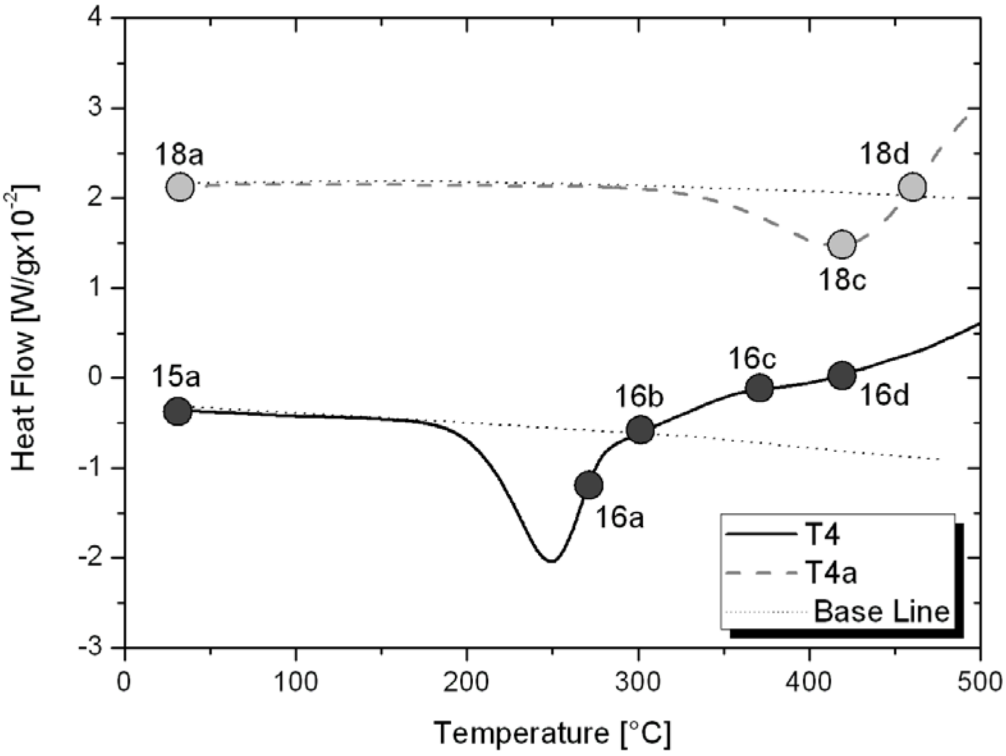

**Figure 5.15.** DSC runs of AlSi1.7 in T4 and T4a conditions (heating rate = 3K/min) with indication of the TEM images presented below.

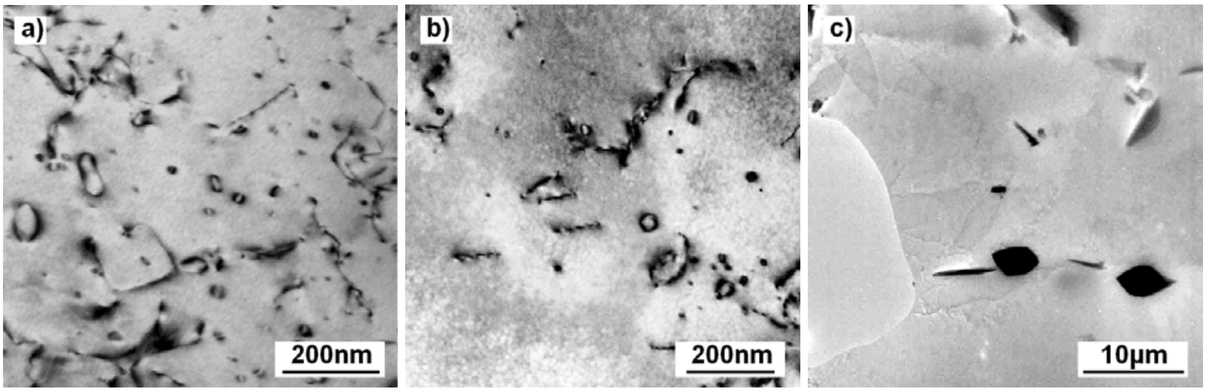

**Figure 5.16.** TEM micrographs of AlSi1.7 after a) ST (T4) and b) isothermal aging at 200°C/1h (T6a) showing dislocations and loops, and c) lamellae and inclusions of Si (T6a) close to grain boundaries.

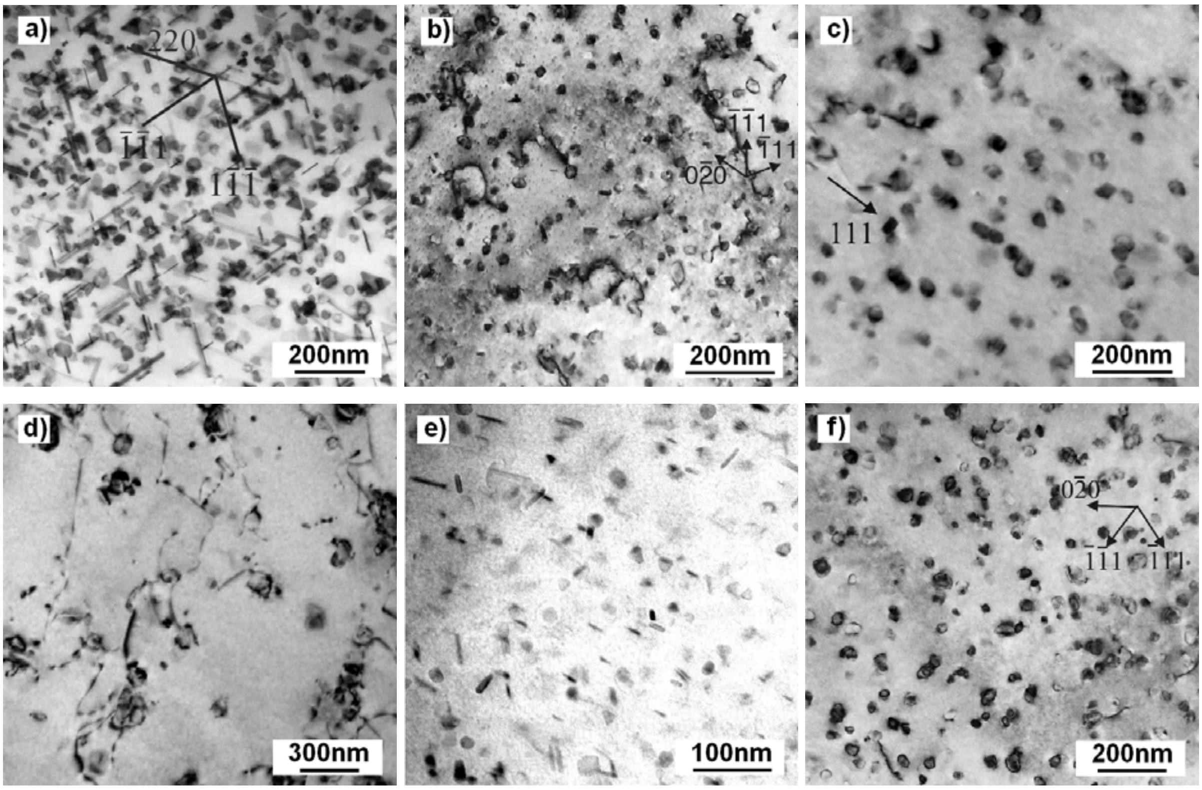

**Figure 5.17.** TEM micrographs of AlSi1.7 after continuous heating up to a) 270°C (T6*d), b) 300°C (T6*e), c) 370°C (T6*f) and d) 420°C (T6*g); and isothermal heating at e) 200°C/10h (T6b) and f) 300°C/1h (T6c). The orientation of crystallographic planes is indicated.

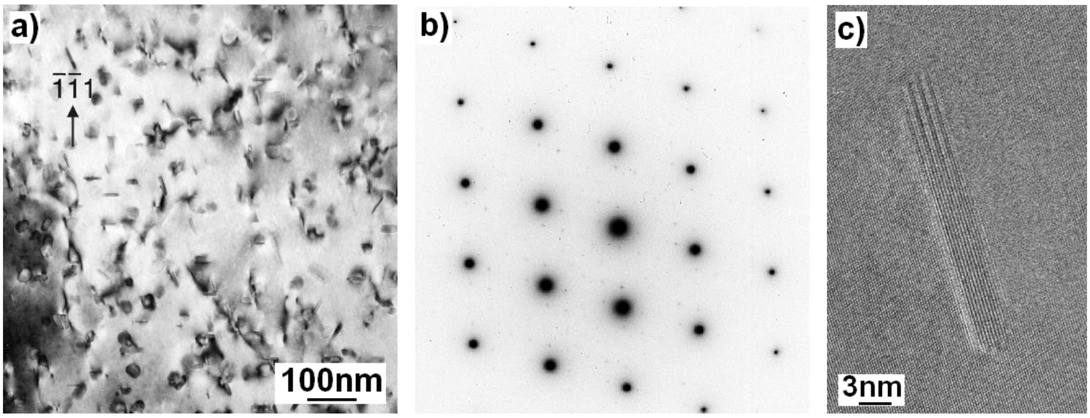

**Figure 5.18.** a) TEM image of AlSi1.7 in the T6*e condition with b) diffraction pattern, and c) high resolution TEM image of Si platelet.

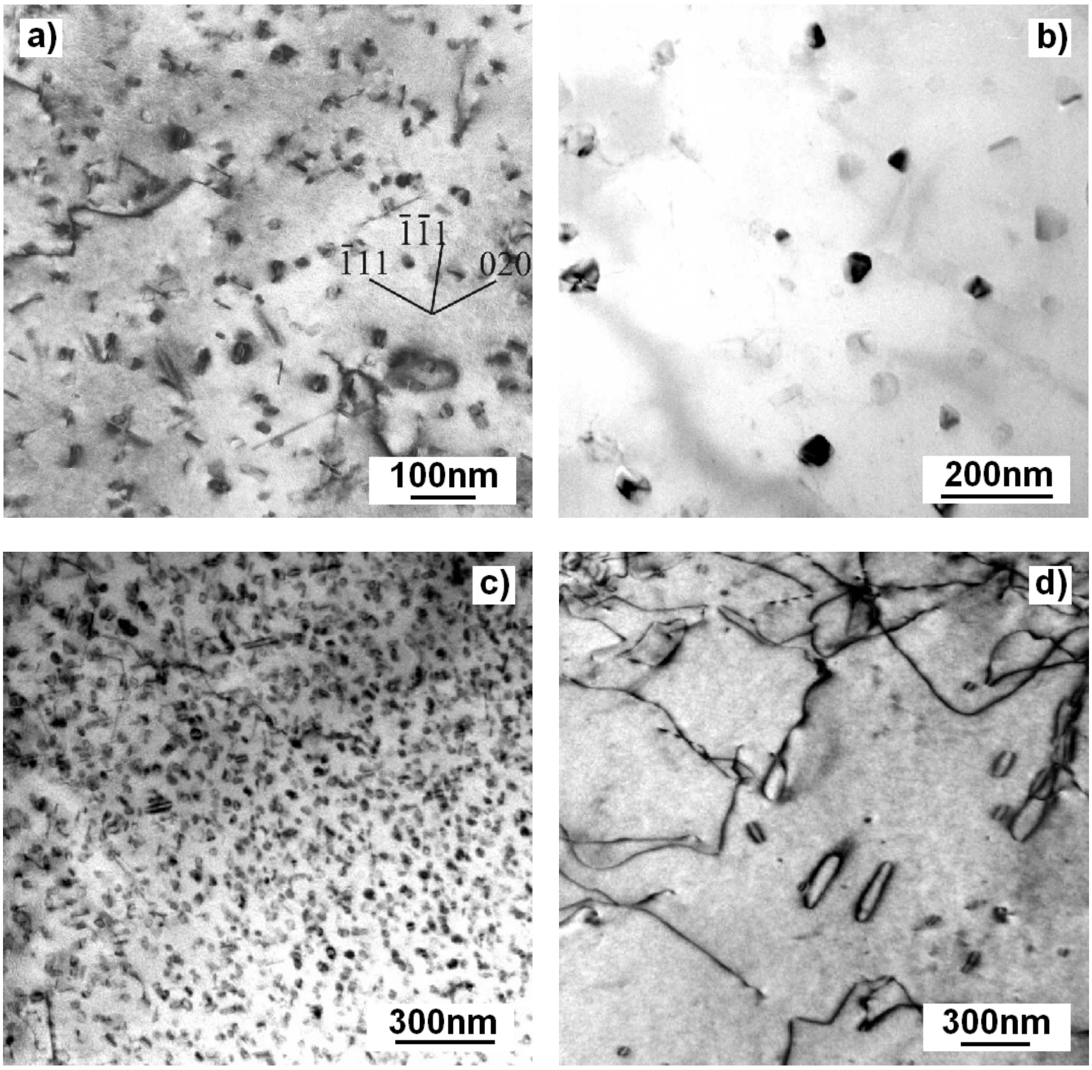

**Figure 5.19.** TEM micrographs of AlSi1.7 after slow cooling after ST at a) 20 (T4a) and b) 3K/min (T4b) and after heating of previous T4a condition up to c) 420 and d) 460°C.

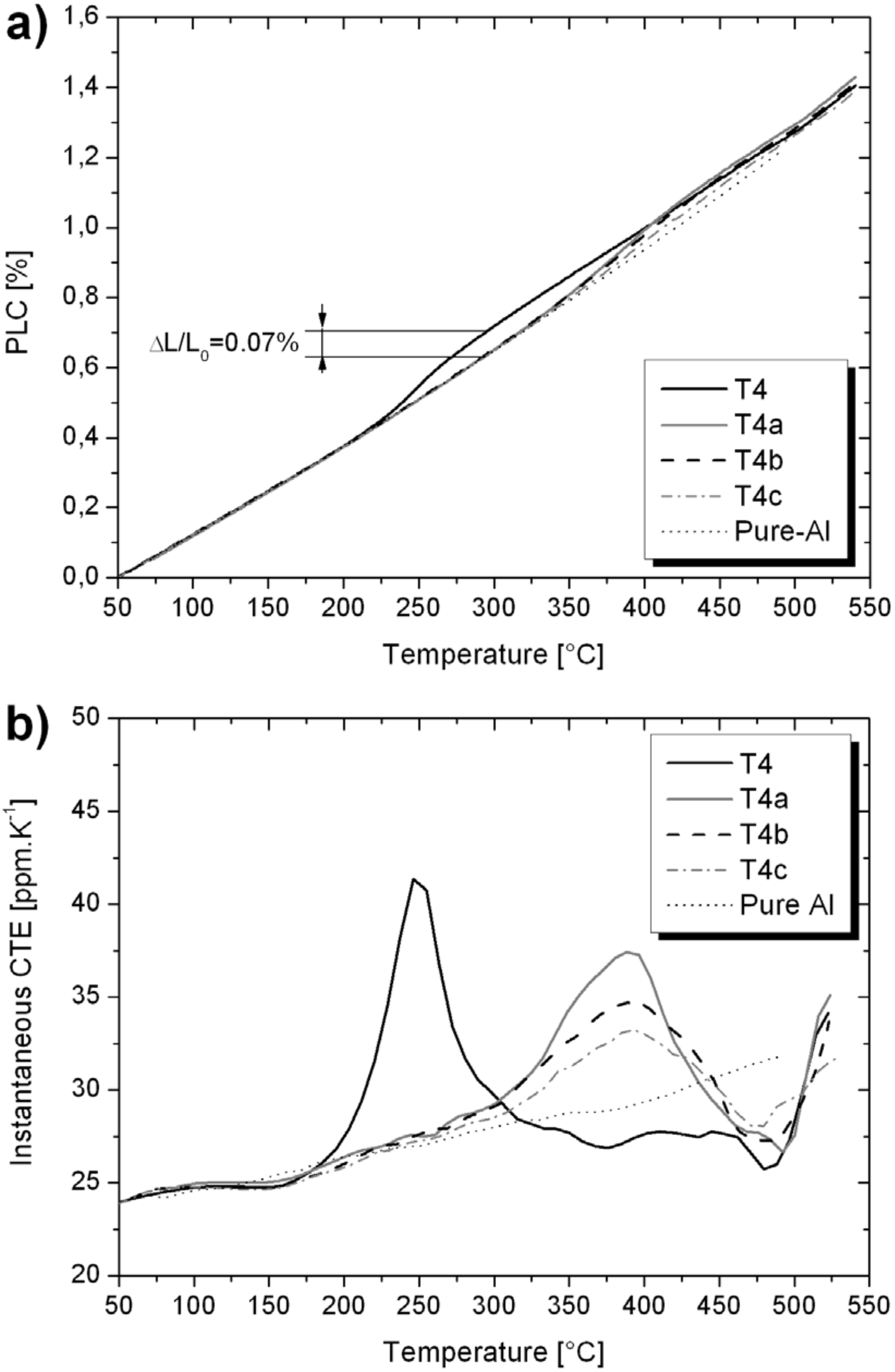

**Figure 5.20.** a) per cent linear change (PLC) and b) CTE of AlSi1.1 in T4 and after different cooling rates from ST (20, 3 and 1K/min).

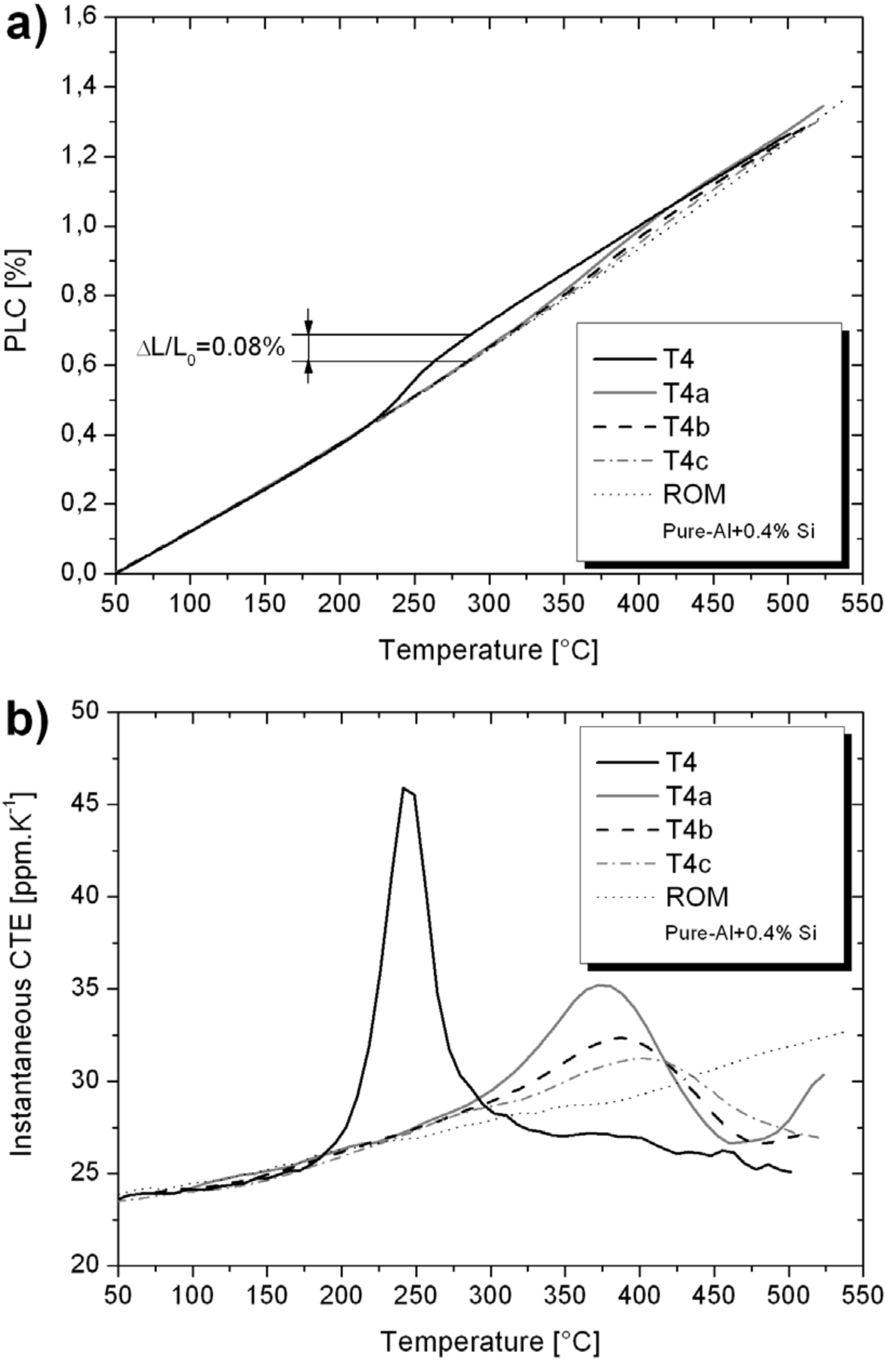

**Figure 5.21.** a) per cent linear change (PLC) and b) CTE of AlSi1.7 in T4 and after different cooling rates from ST (20, 3 and 1K/min).

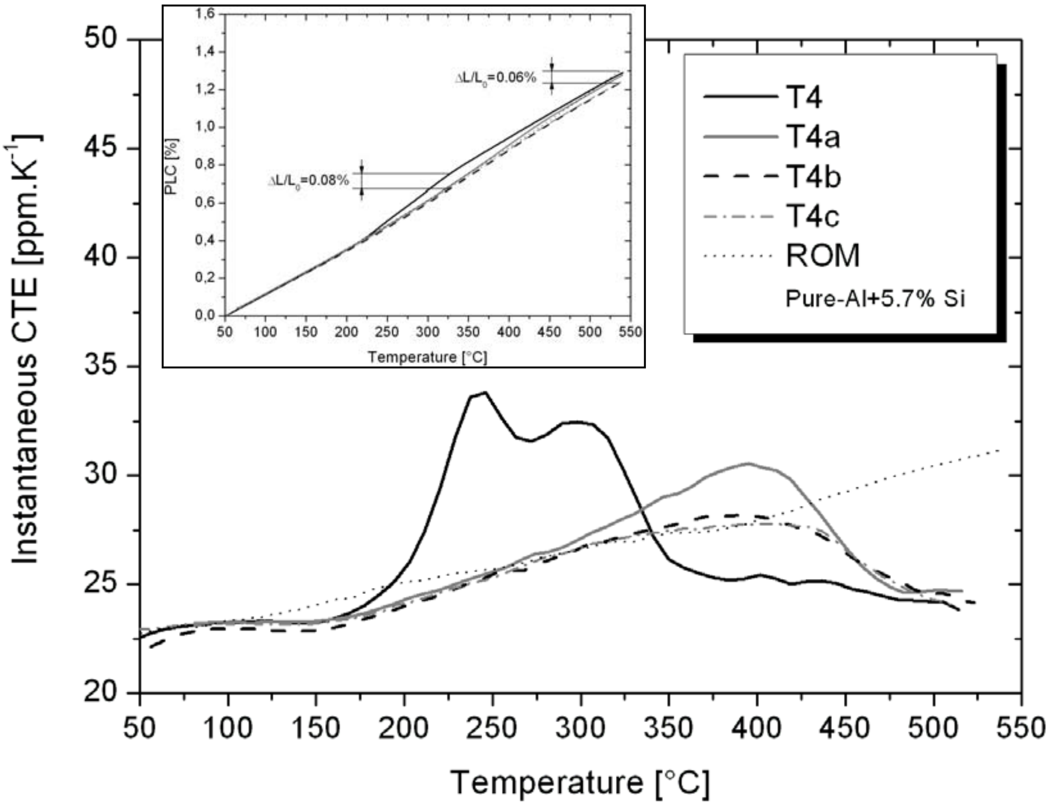

**Figure 5.22.** CTE and PLC (see detail) of AlSi7 alloy in T4 after different cooling rates from ST (20, 3 and 1K/min).

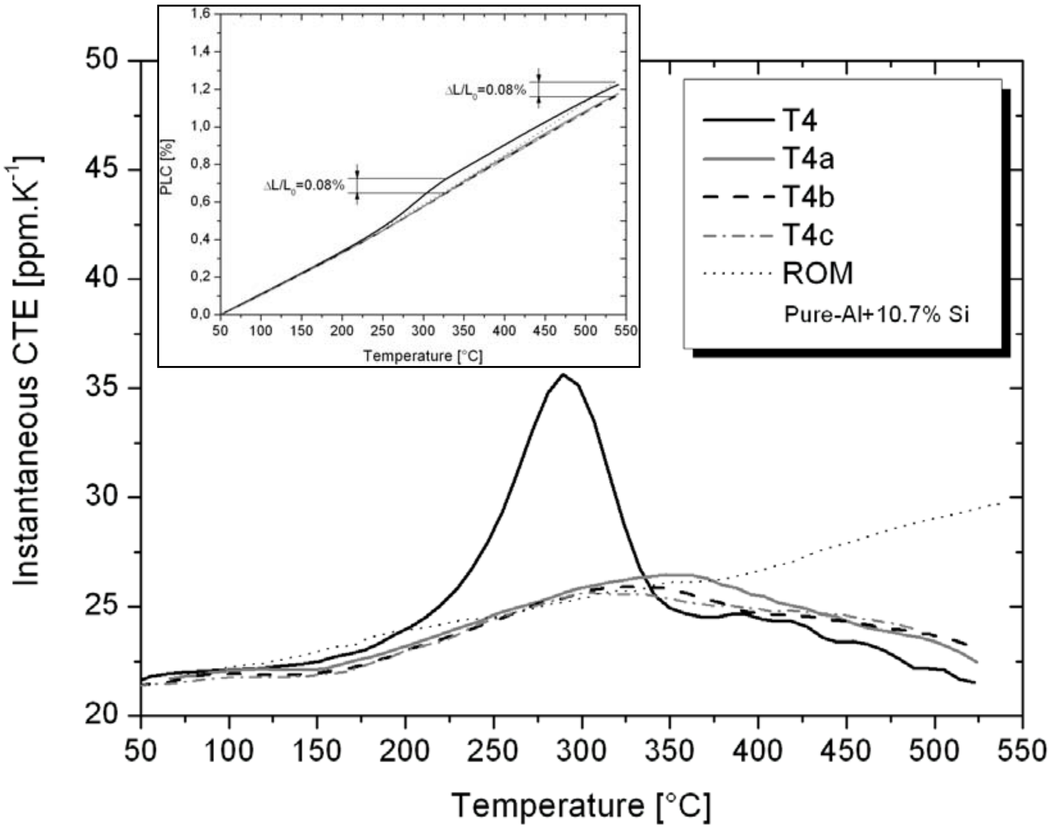

**Figure 5.23.** CTE and PLC (see detail) of AlSi12 alloy in T4 after different cooling rates from ST (20, 3 and 1K/min).

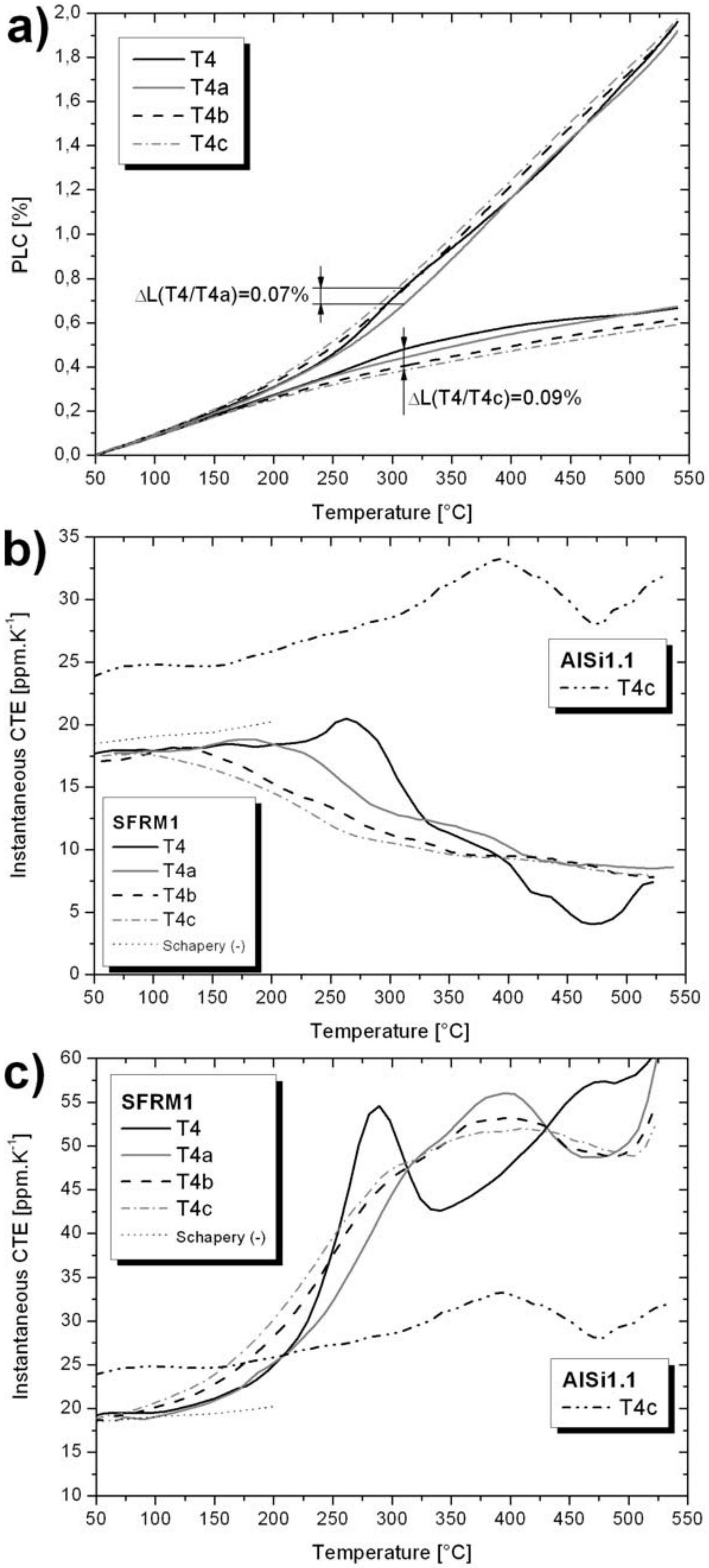

**Figure 5.24.** a) PLC in transverse and in fibre plane directions and b) CTE(T) in transverse and c) in plane directions of AlSi1.1/$Al_2O_3$/20s after different thermal conditions.

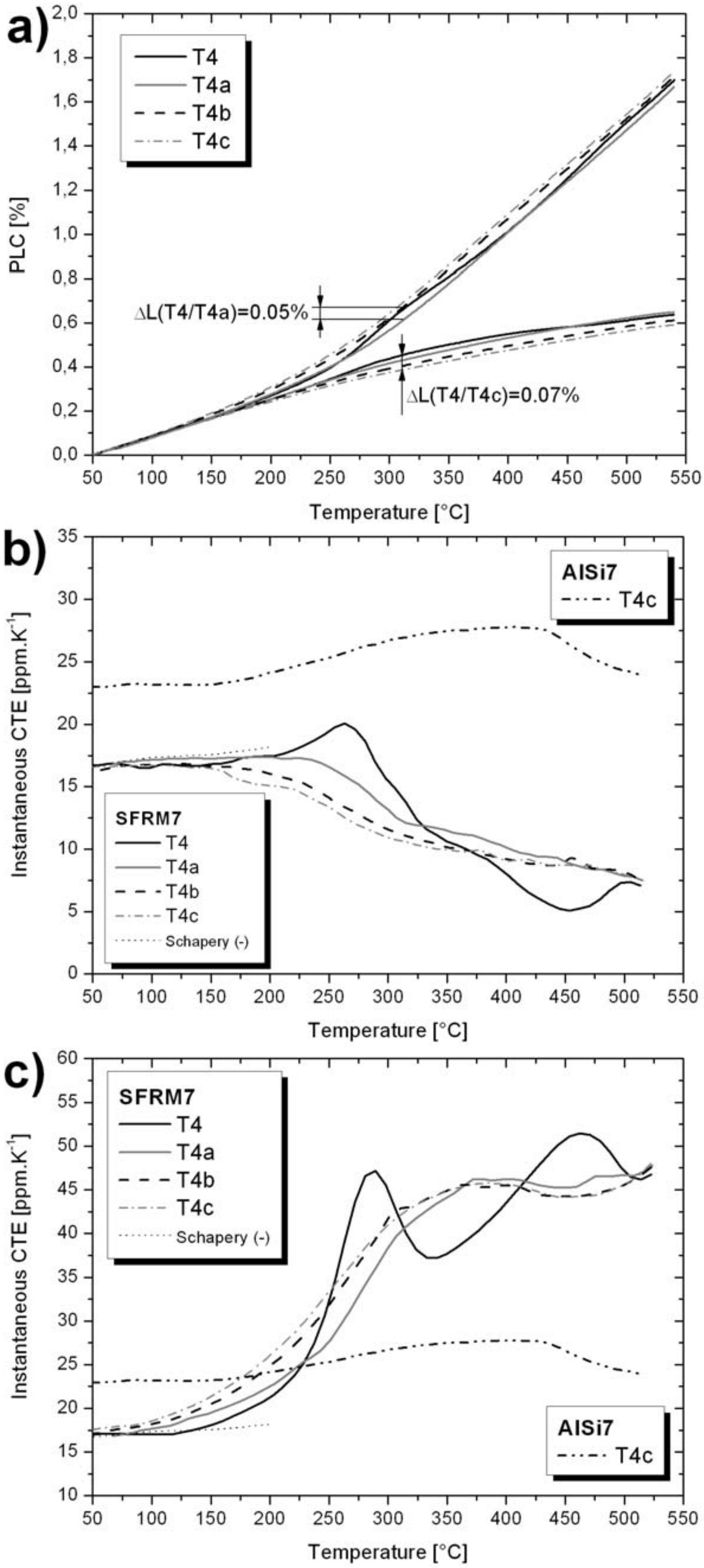

**Figure 5.25.** a) PLC in transverse and in fibre plane directions and b) CTE(T) in transverse and c) in plane directions of AlSi7/$Al_2O_3$/20s (v1) after different thermal conditions.

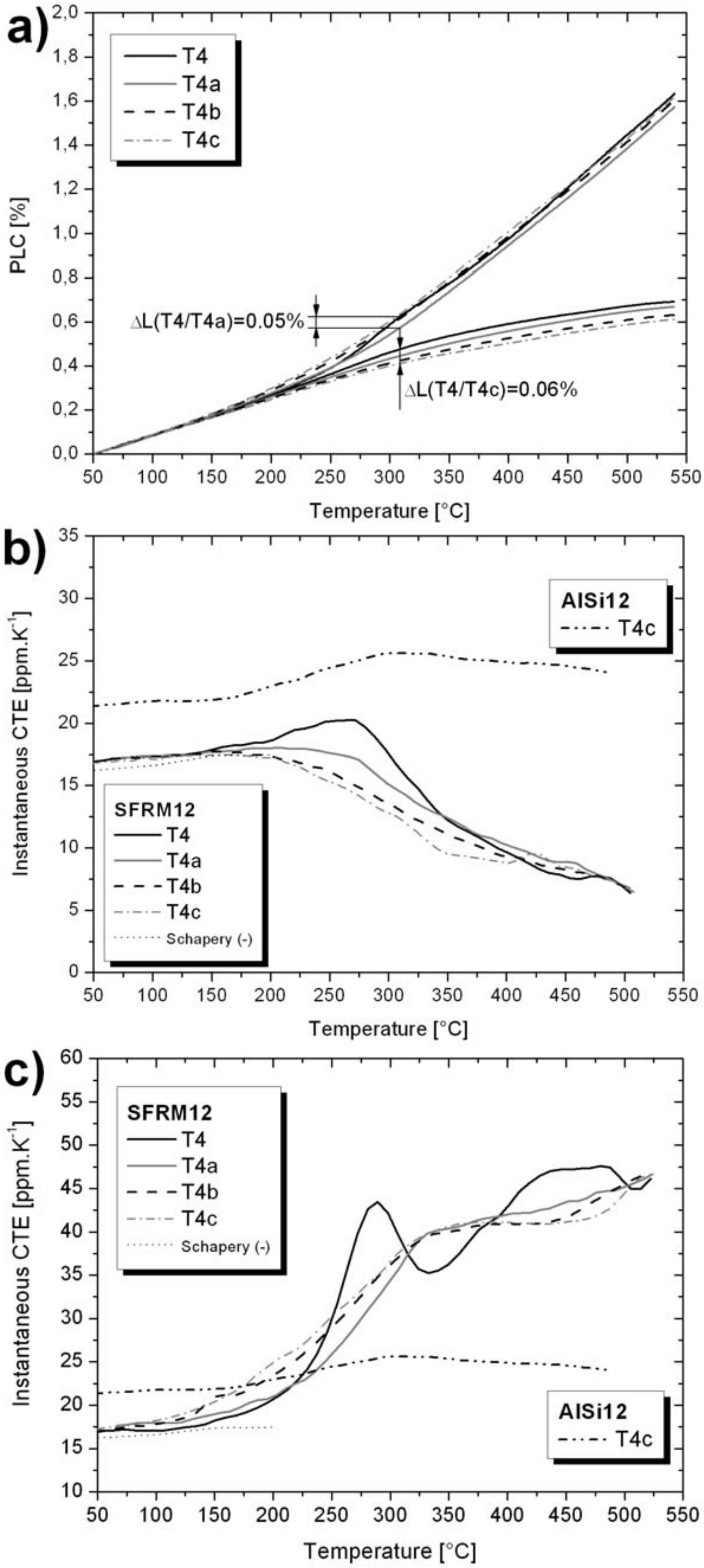

**Figure 5.26.** a) PLC in transverse and in fibre plane directions and b) CTE(T) in transverse and c) in plane directions of AlSi12/$Al_2O_3$/20s after different thermal conditions.

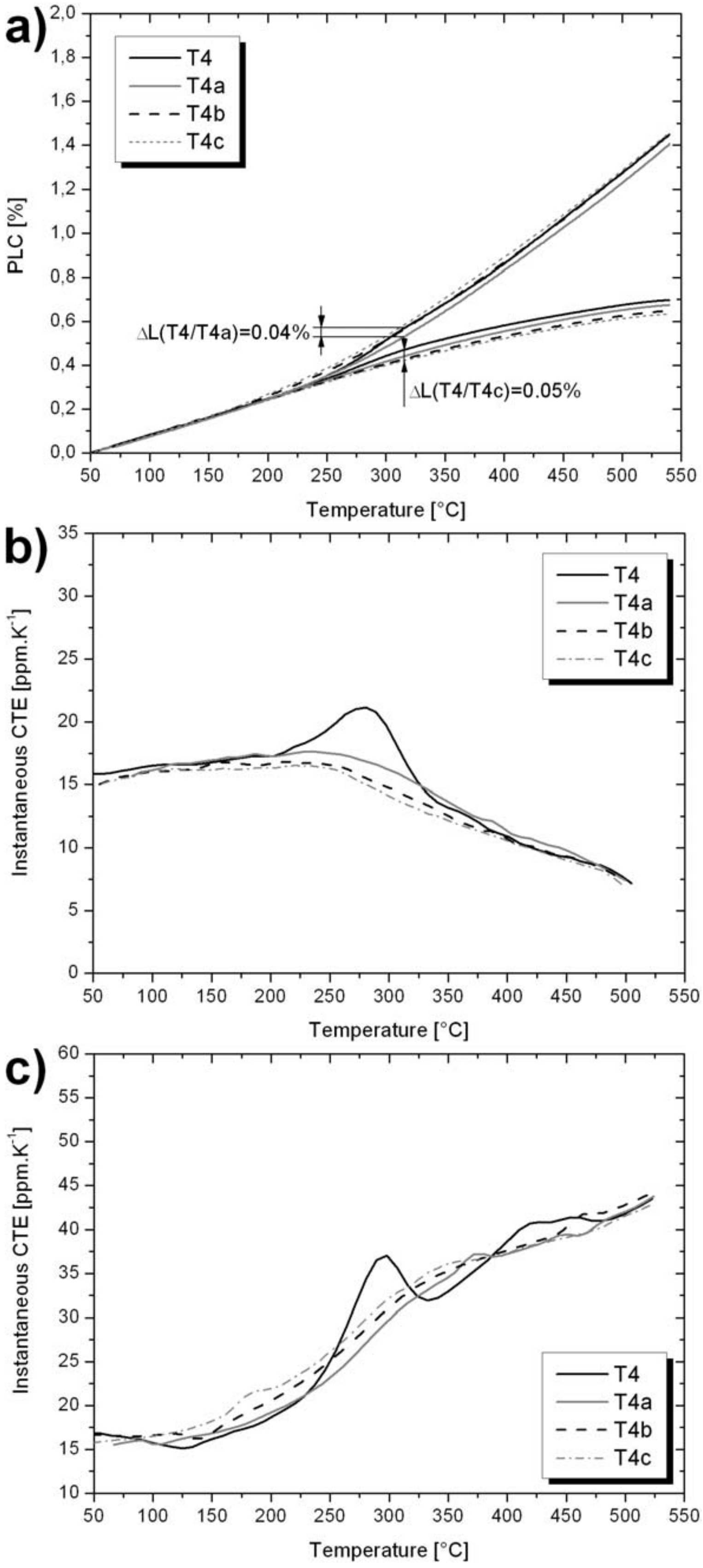

**Figure 5.27.** a) PLC in transverse and in fibre plane directions and b) CTE(T) in transverse and c) in plane directions of AlSi18/$Al_2O_3$/20s after different thermal conditions.

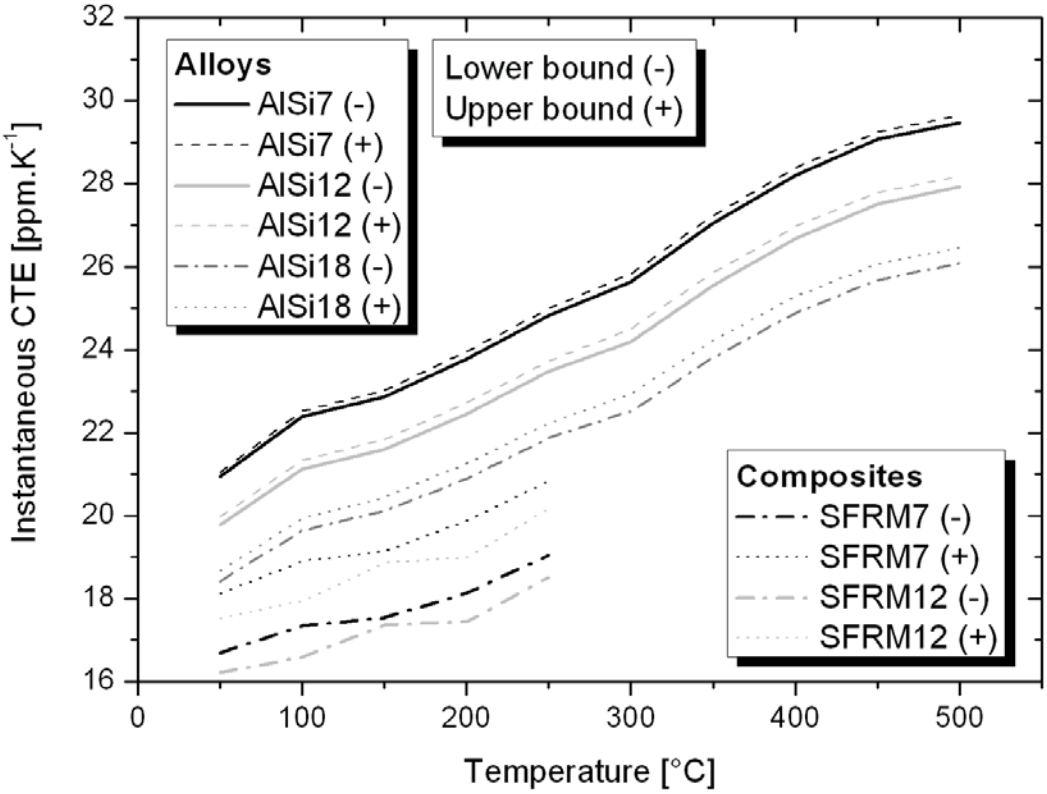

**Figure 5.28.** Modeled instantaneous CTE(T) by Schapery model showing upper and lower bounds for AlSi7-12-18 alloys and AlSi7-12/$Al_2O_3$/20s composite materials.

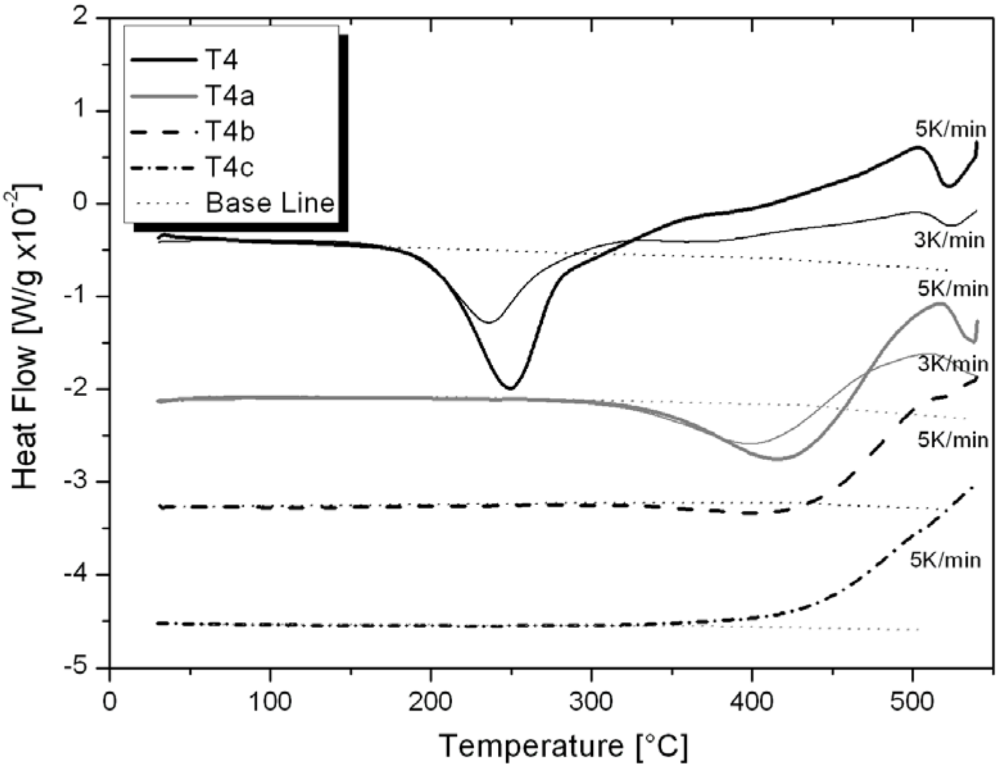

**Figure 5.29.** DSC runs of an AlSi1.7 alloy in T4 and after slow cooling from ST at 20 (T4a), 3 (T4b) and 1K/min (T4c) with base line compensation (heating rate 3 and 5K/min).

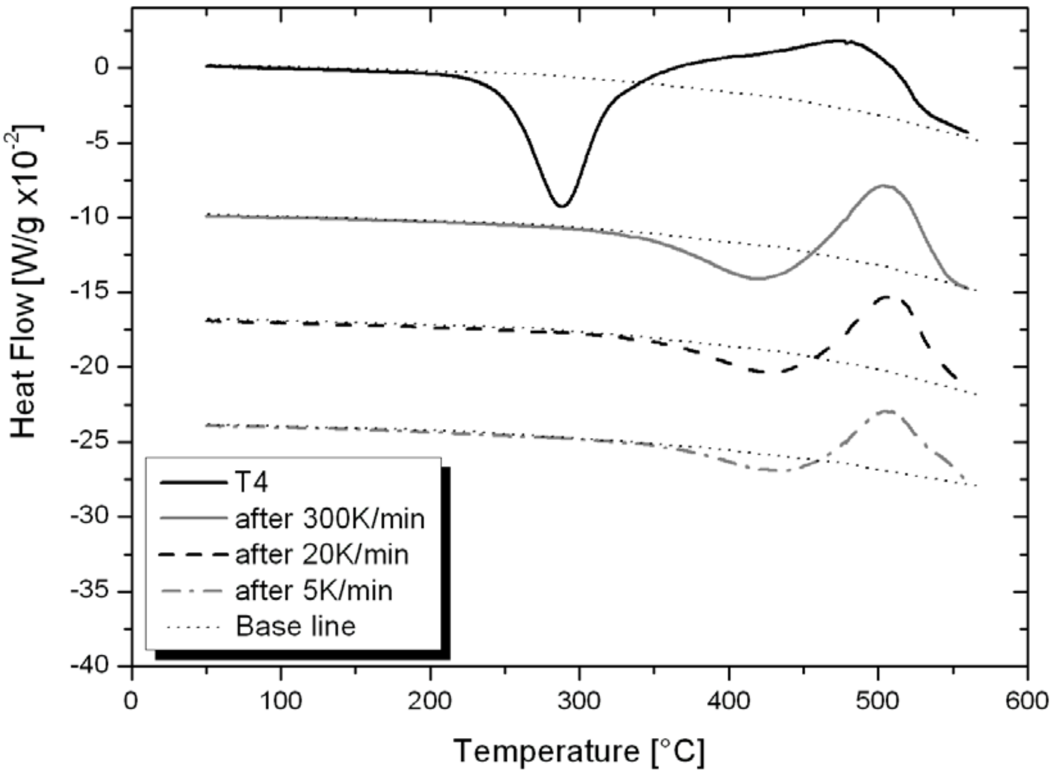

**Figure 5.30.** DSC runs of an AlSi1.1 alloy in T4 and after slow cooling from ST at 300 (T4e), 20 (T4b) and 5K/min (T4d) (heating rate 20K/min) with base line compensation.

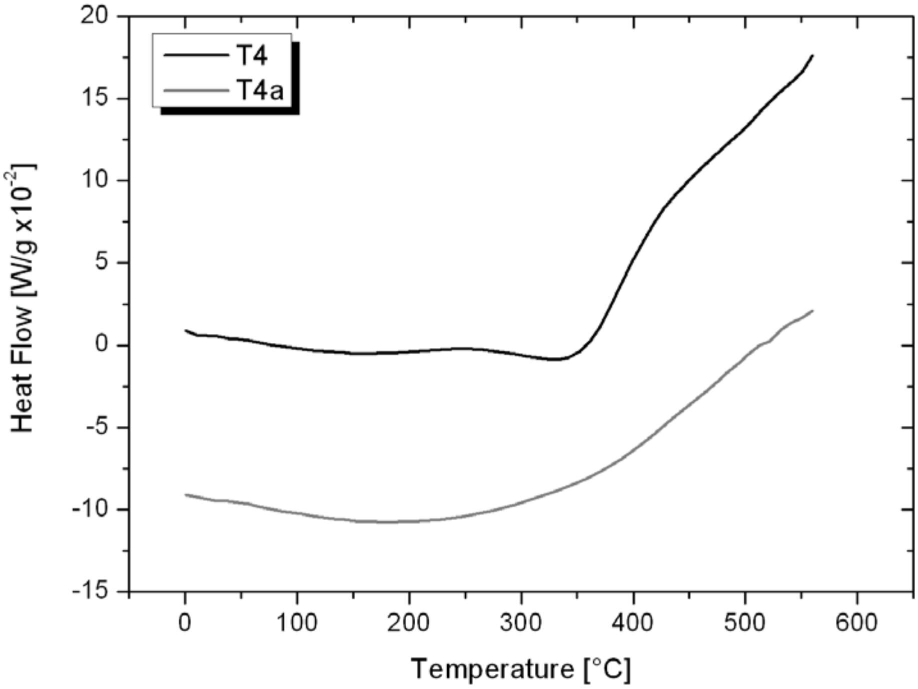

**Figure 5.31.** DSC runs of an AlSi12 alloy in T4 and T4a conditions (heating rate 20K/min) without base line compensation.

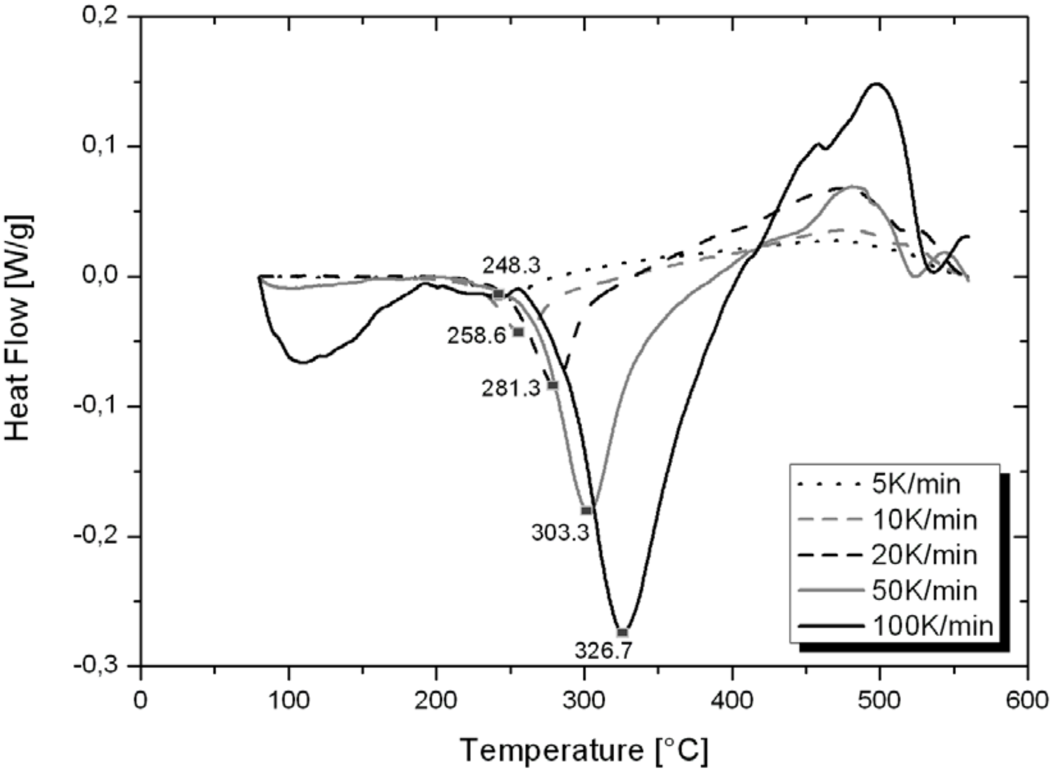

**Figure 5.32.** DSC runs of an AlSi1.1 alloy in T4 at different heating rates (peak temperatures are indicated).

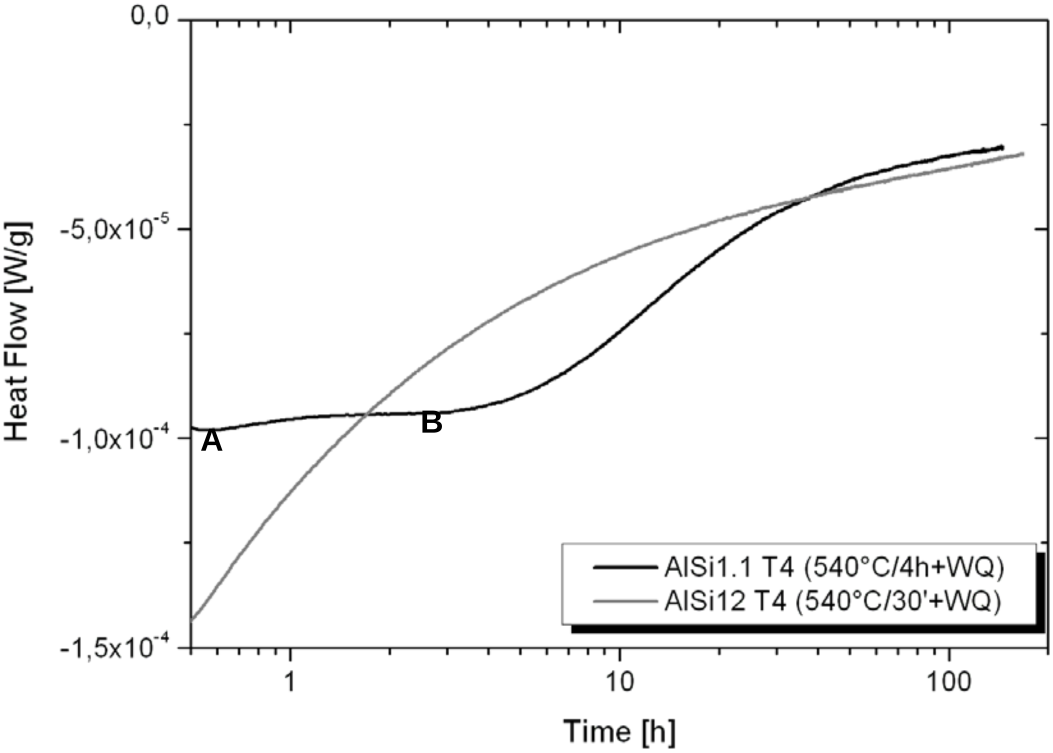

**Figure 5.33.** Isothermal DSC runs of AlSi1.1 and AlSi12 in the T4 conditions.

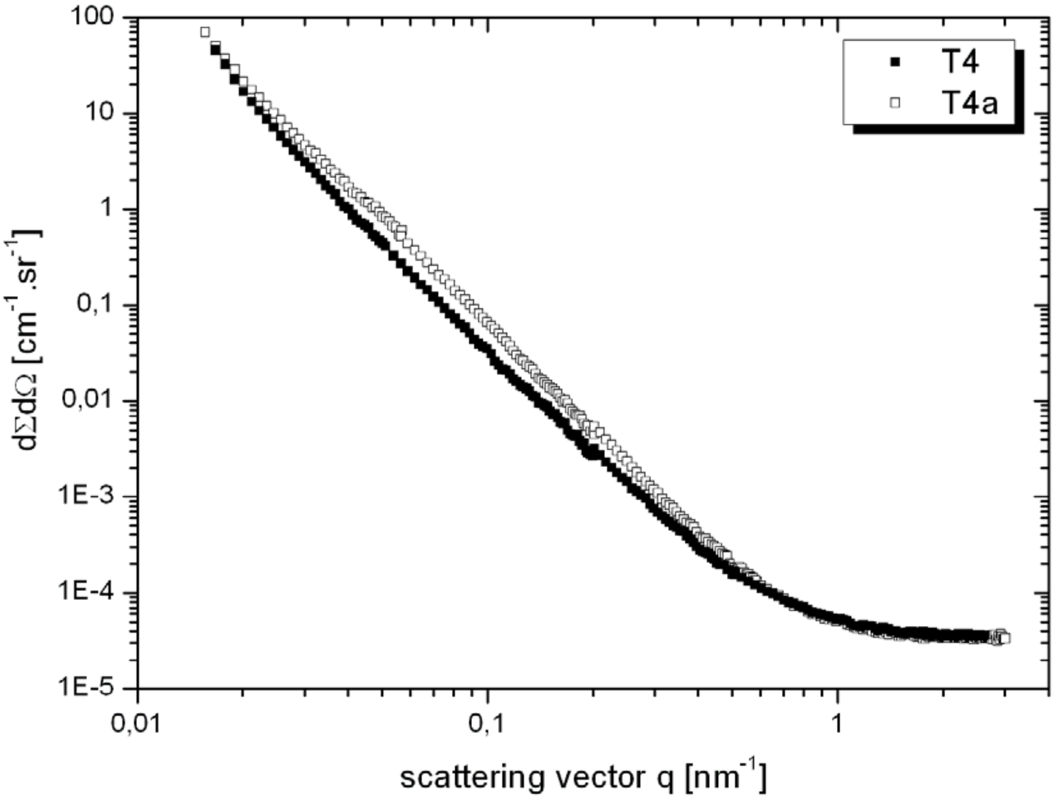

**Figure 5.34.** Cross section vs. scattering vector in AlSi1.1 in T4 and T4a (slow cooled sample at 20K/min from ST)

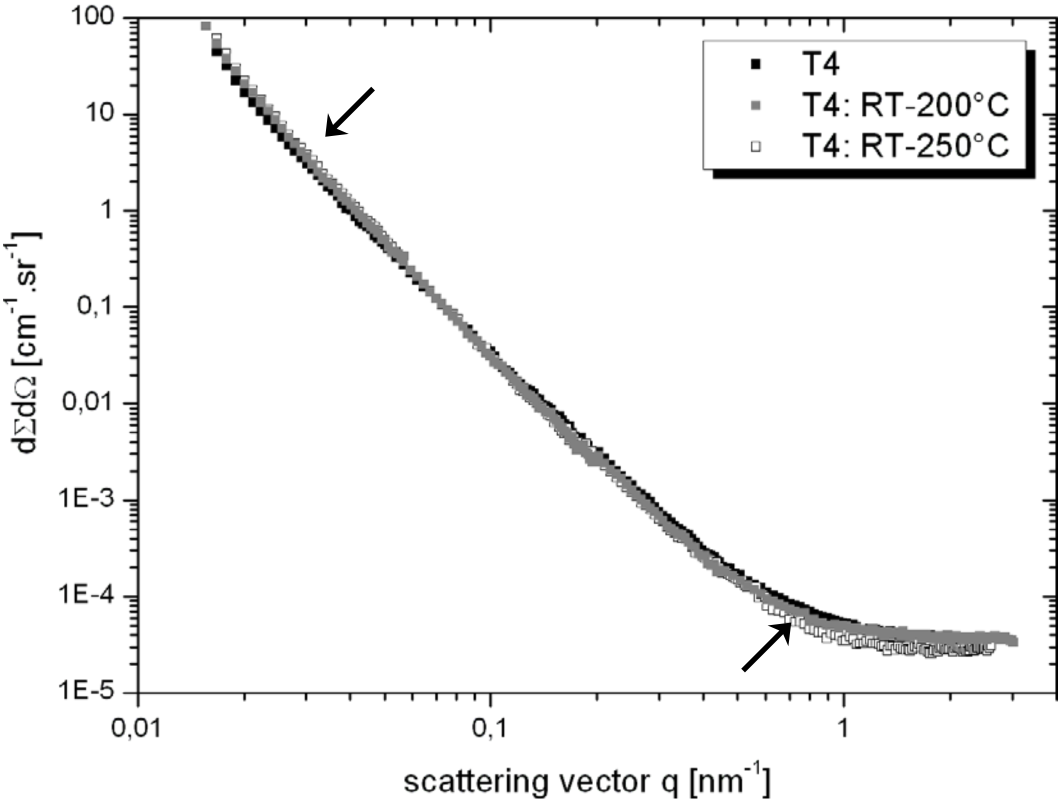

**Figure 5.35.** Cross section vs. scattering vector in AlSi1.1 in T4, T6*b and T6*c

(T4 + RT→3K/min→200 and 250°C, respectively).

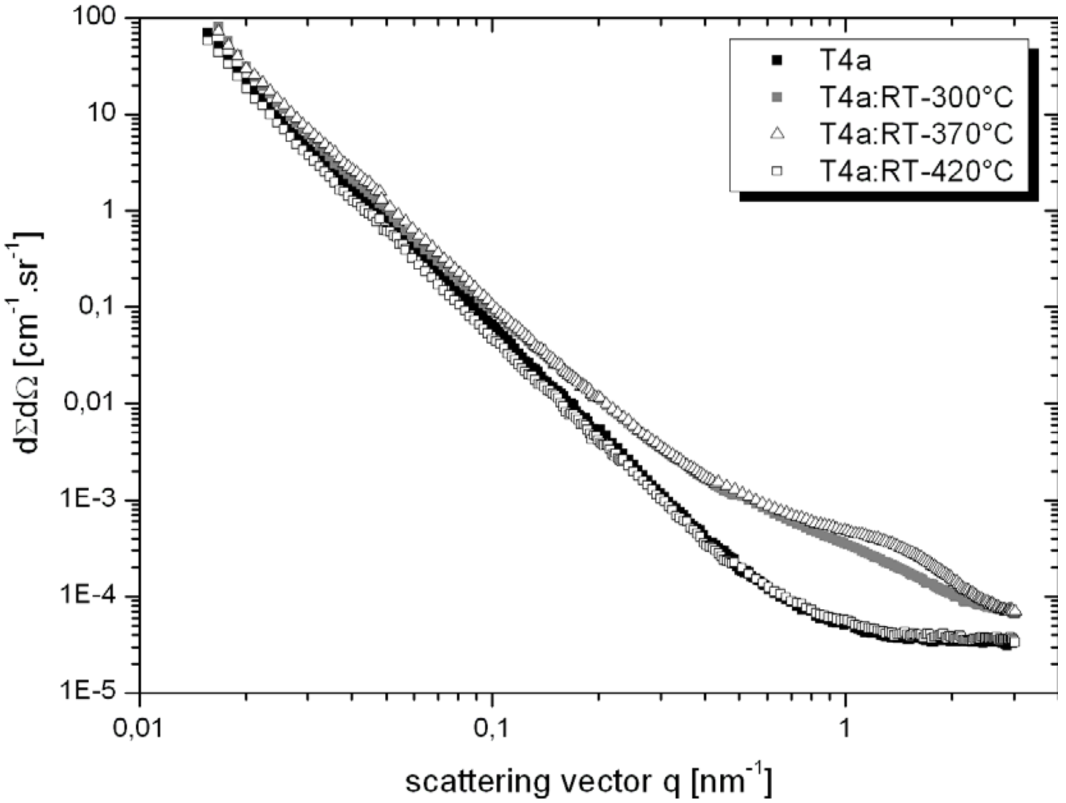

**Figure 5.36.** Cross section vs. scattering vector in AlSi1.1 in T4a and posterior heating to 300, 370 and 420°C (T7*e, T7*f and T7*g, respectively).

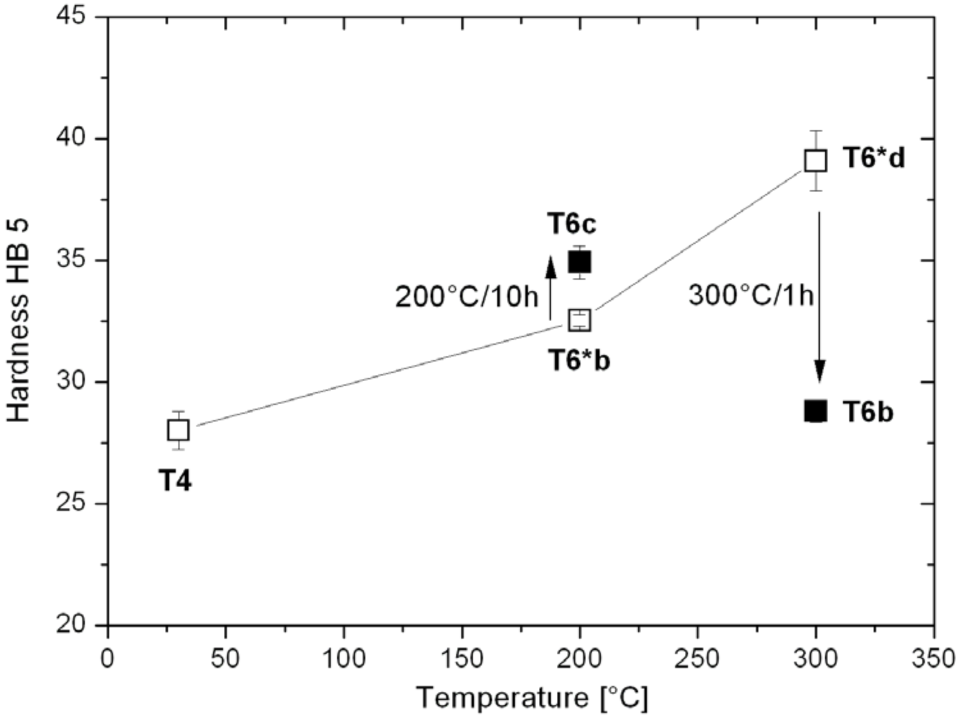

**Figure 5.37.** Brinell hardness results of AlSi1.1 alloy after different thermal conditions

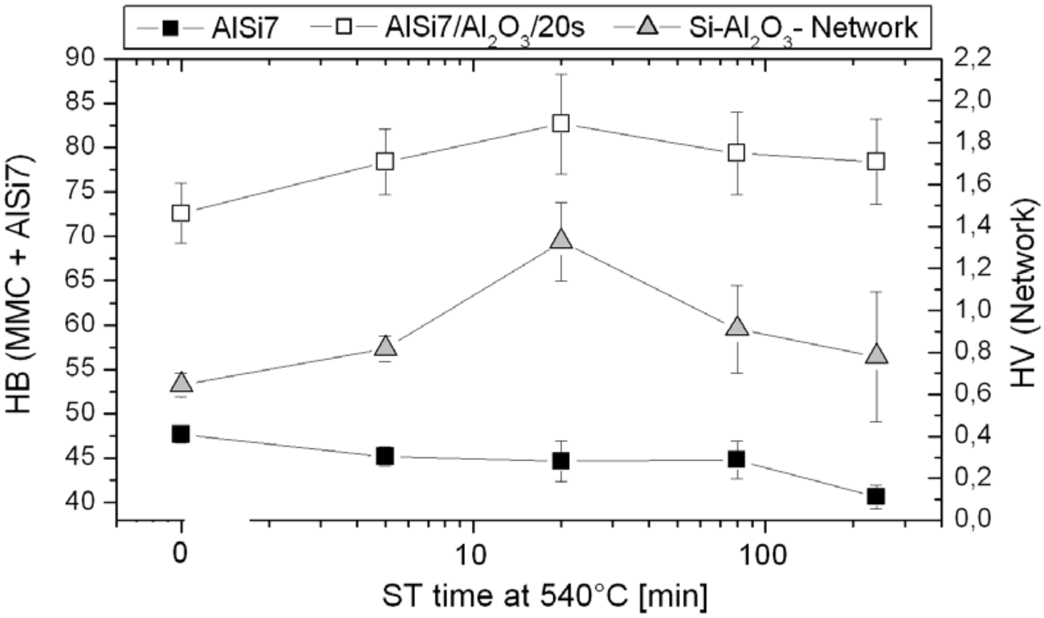

**Figure 5.38.** Hardness test results for different solution treatment times by HB 1/10/10 for the AlSi7 alloy, AlSi7/$Al_2O_3$/20s (v1) composite and by HV 0.1/10 for the corresponding extracted Si/$Al_2O_3$ network.

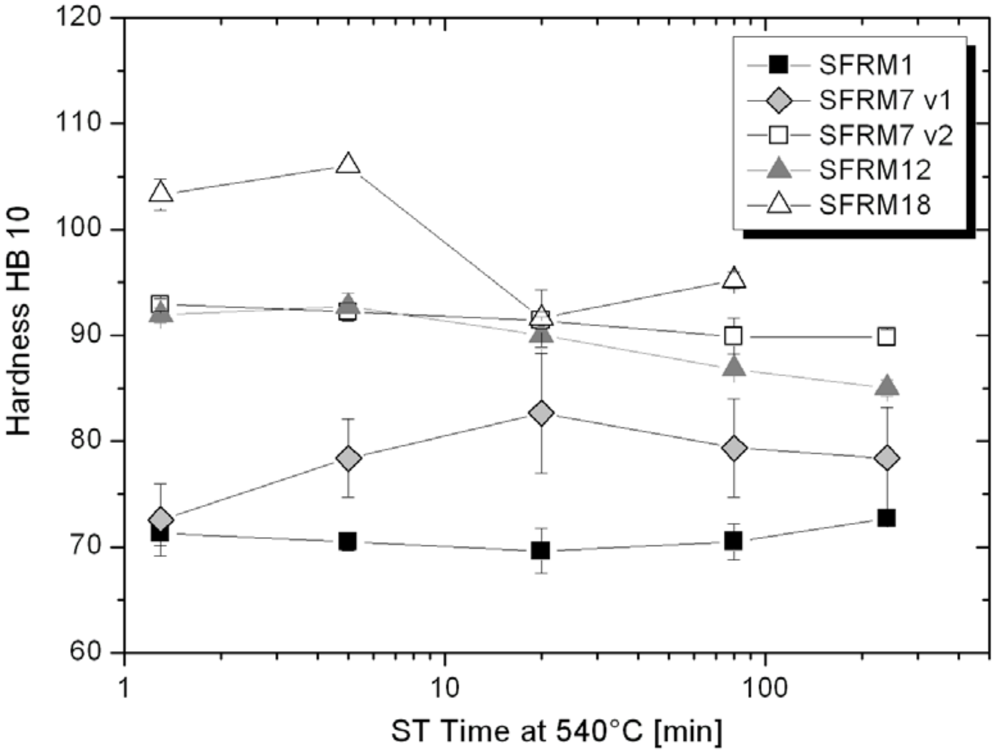

**Figure 5.39.** Hardness Brinell results of investigated SFRM1, SFRM7v2, SFRM12 and SFRM18 at different solution treatment times at 540°C.

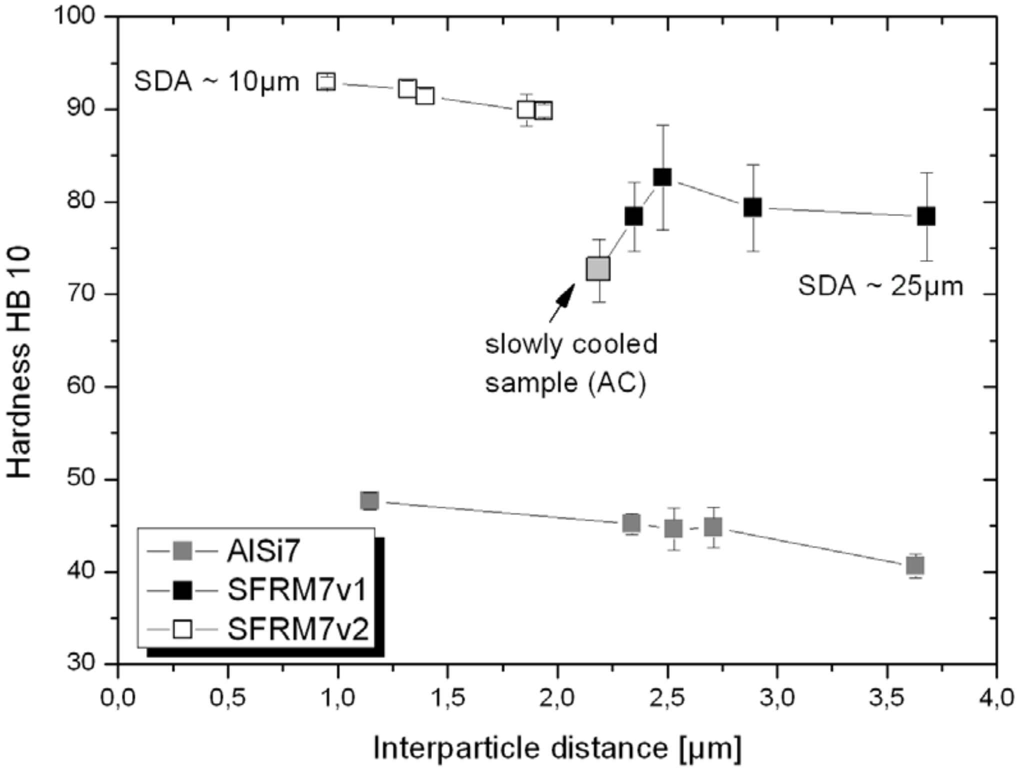

**Figure 5.40.** Hardness Brinell results of investigated AlSi7 alloy and, 1st and 2nd versions of SFRM7 composite material vs. measured Si interparticle distance.

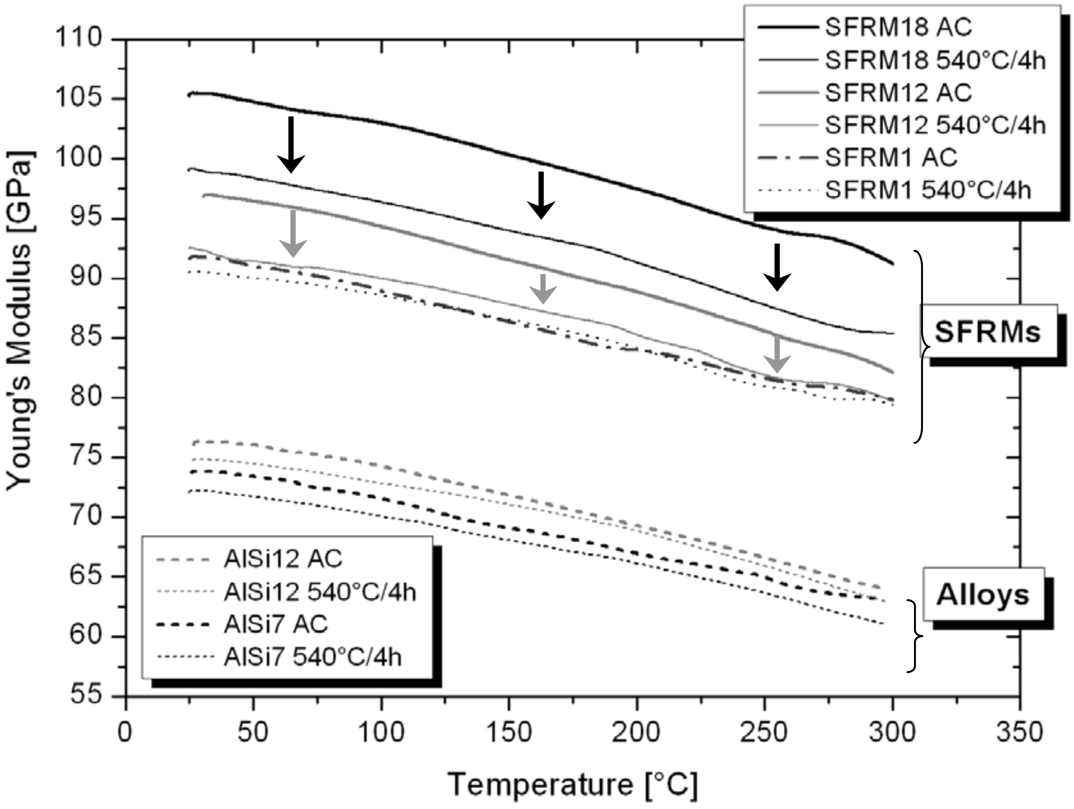

**Figure 5.41.** Values of E modulus in the in fibre plane direction as a function of temperature for SFRM1, 12 and 18 composites and AlSi7, 12 alloys in as cast (AC) and T4 conditions.

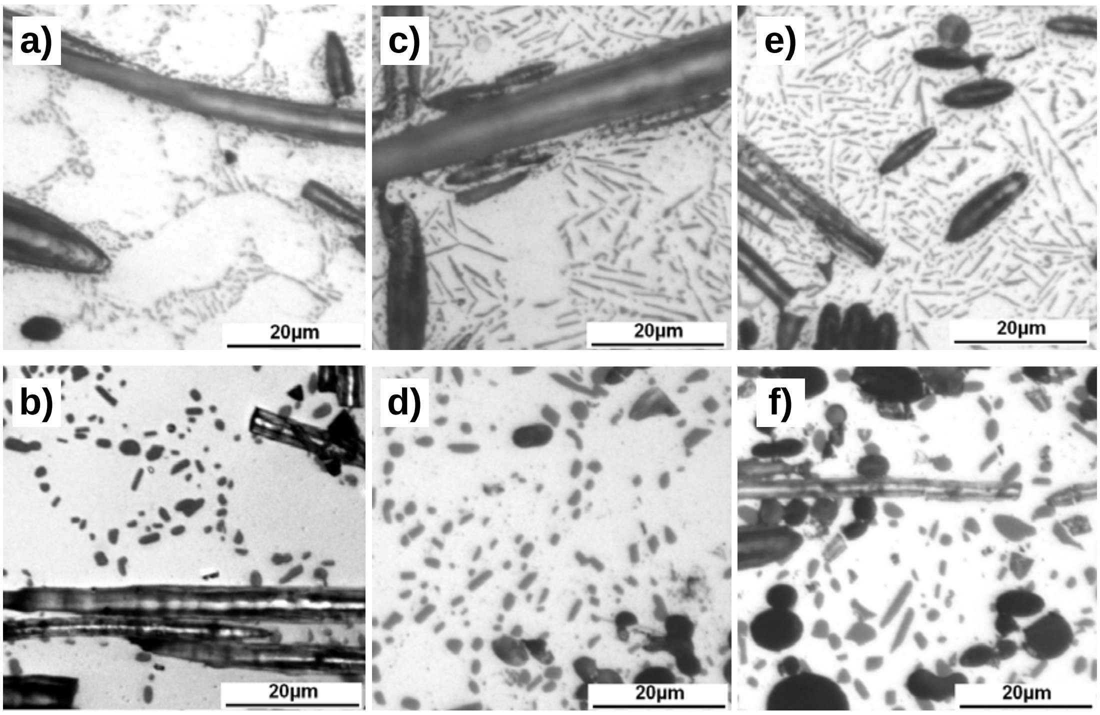

**Figure 5.42.** Light optical microscope images of composite materials for the estimation of microstructural parameters: a,b) AlSi7/$Al_2O_3$/20s, c,d) AlSi12/$Al_2O_3$/20s and e,f) AlSi18/$Al_2O_3$/20s, in as cast and after 540°C/4h, respectively

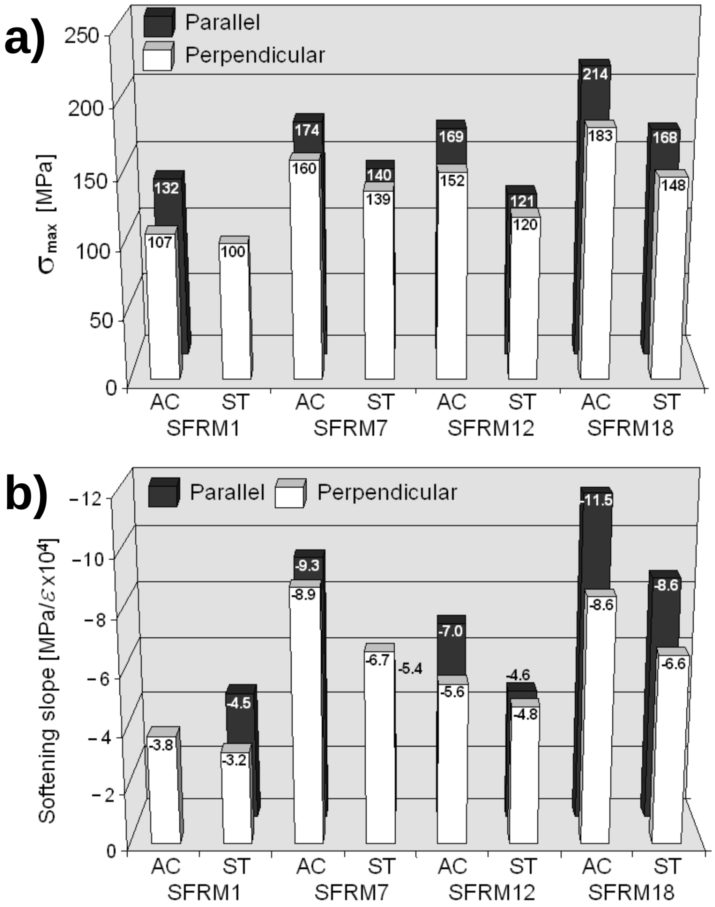

**Figure 5.43.** Summarized information of compression test carried out in the different composite materials. a) $\sigma_{max}$ and b) softening slopes are presented for // and ⊥ samples.

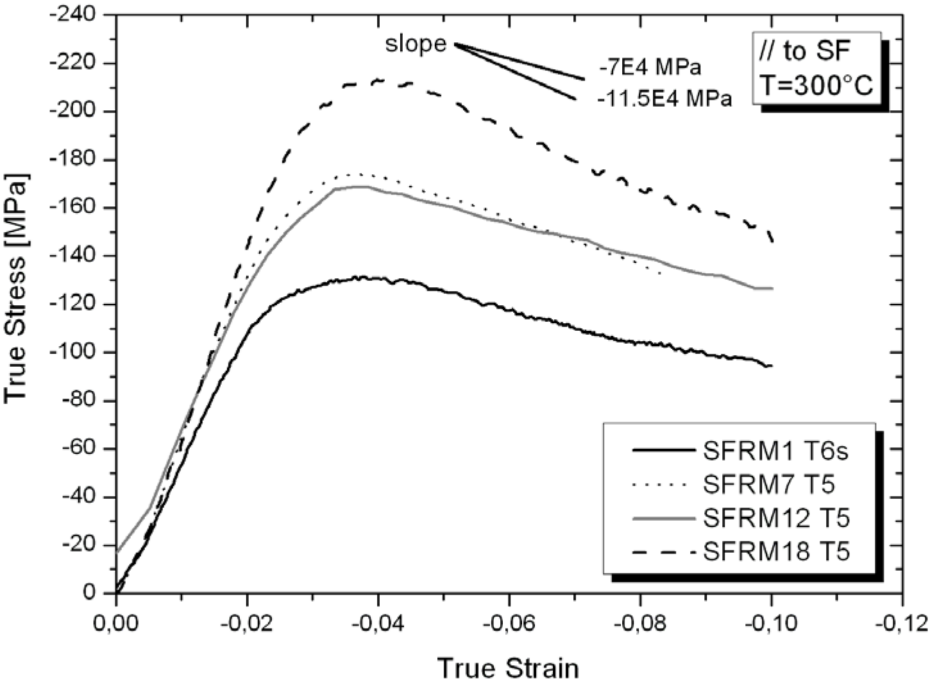

**Figure 5.44.** True Stress vs. True Strain in SFRM1, 7, 12 and 18 composites oriented parallel to fibre plane after dimensional stabilization (T5 condition).

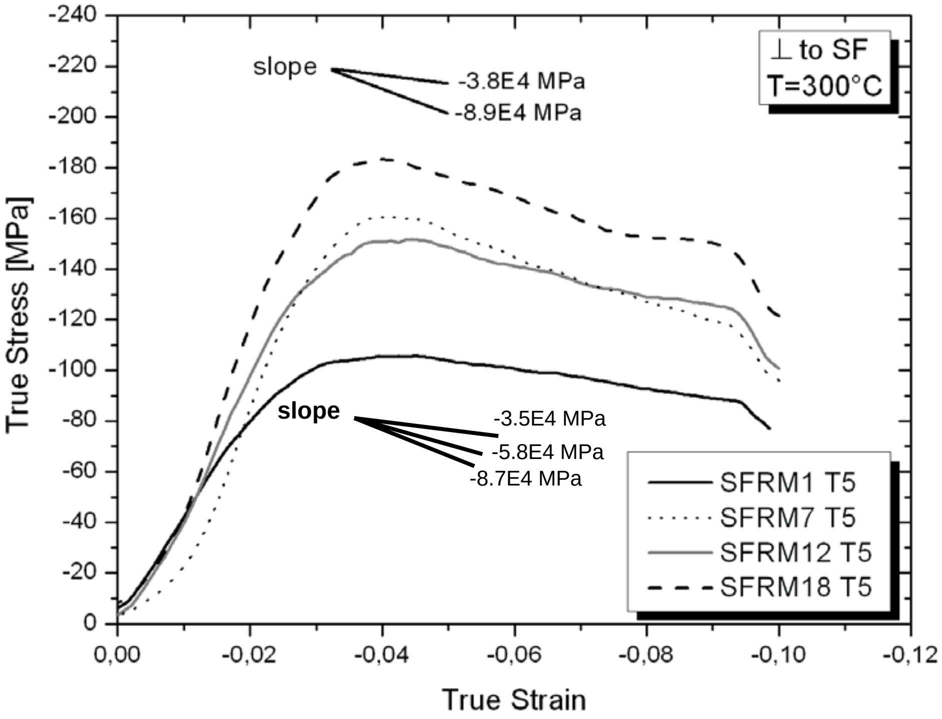

**Figure 5.45.** True Stress vs. True Strain in SFRM1, 7, 12 and 18 composites oriented perpendicular to fibre plane after dimensional stabilization (T5 condition).

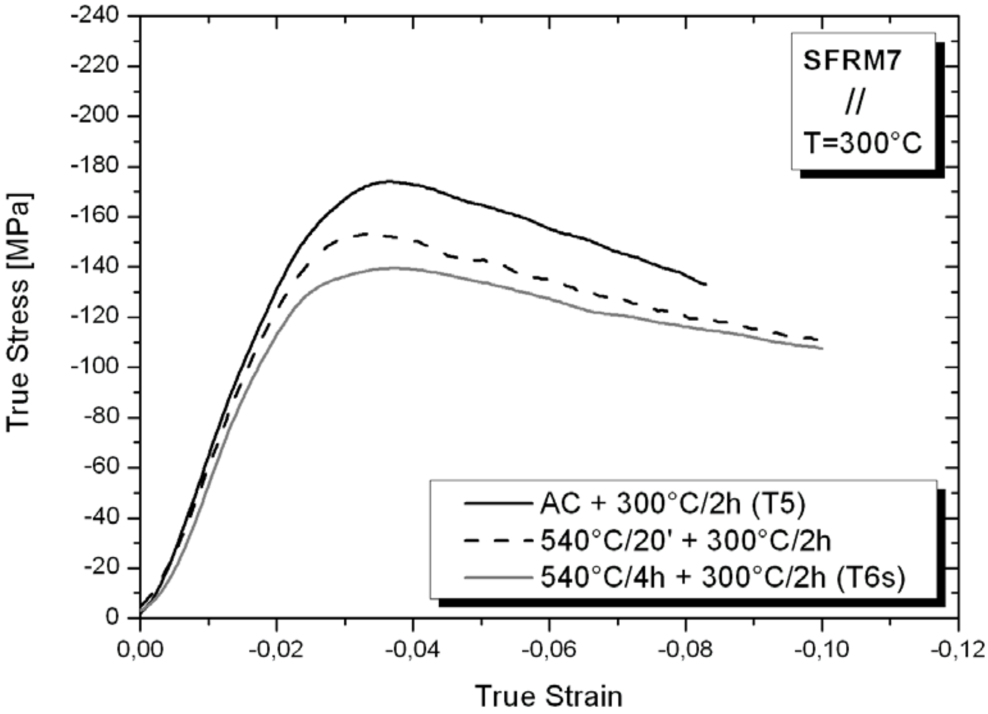

**Figure 5.46.** True Stress vs. True Strain in SFRM7 composite oriented parallel to fibre plane of dimensional stabilized conditions.

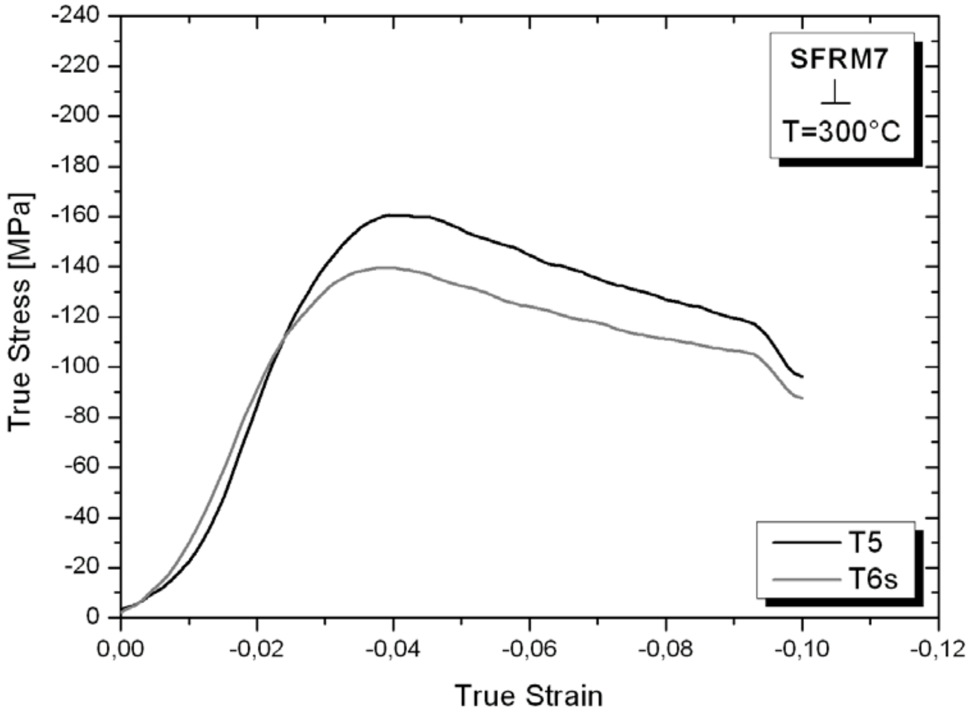

**Figure 5.47.** True Stress vs. True Strain in SFRM7 composite oriented perpendicular to fibre plane after dimensional stabilization.

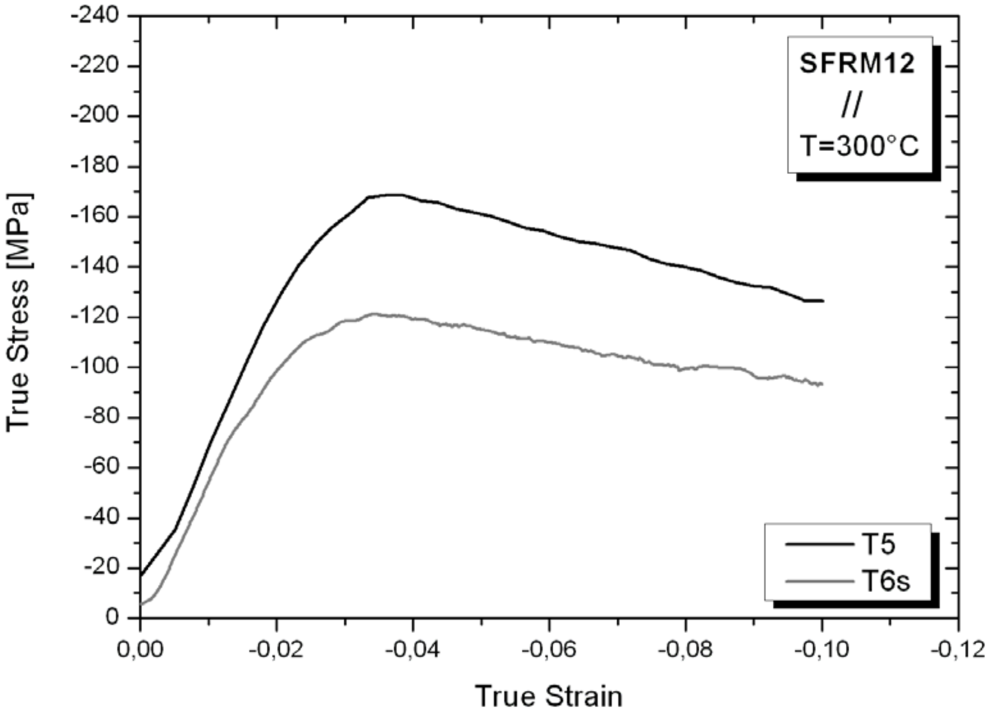

**Figure 5.48.** True Stress vs. True Strain in SFRM12 composite oriented parallel to fibre plane after dimensional stabilization.

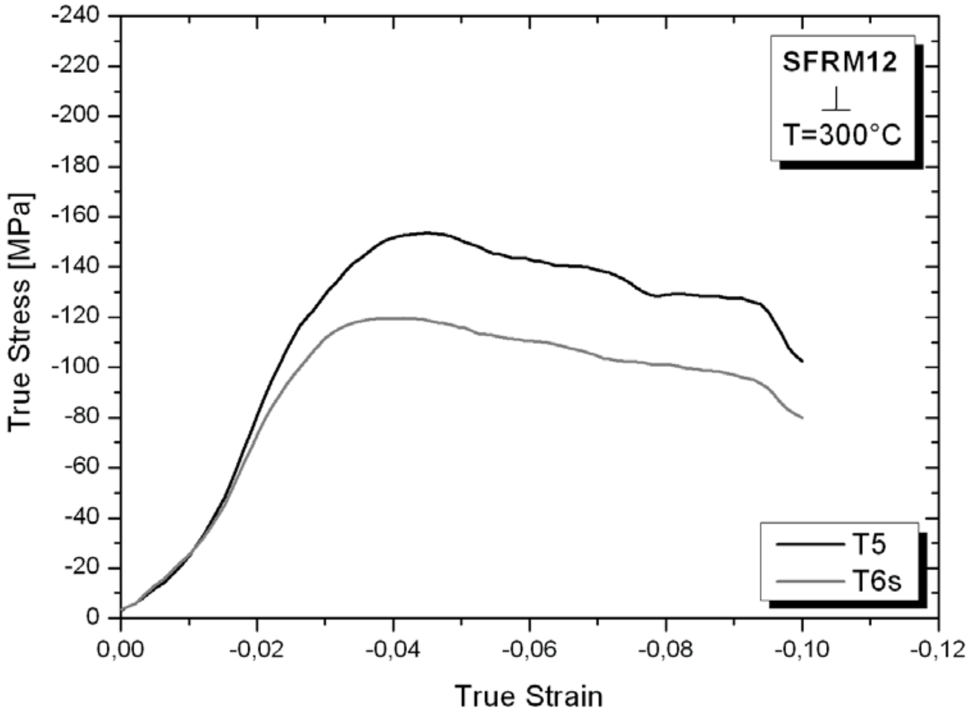

**Figure 5.49.** True Stress vs. True Strain in SFRM12 composite oriented perpendicular to fibre plane after dimensional stabilization.

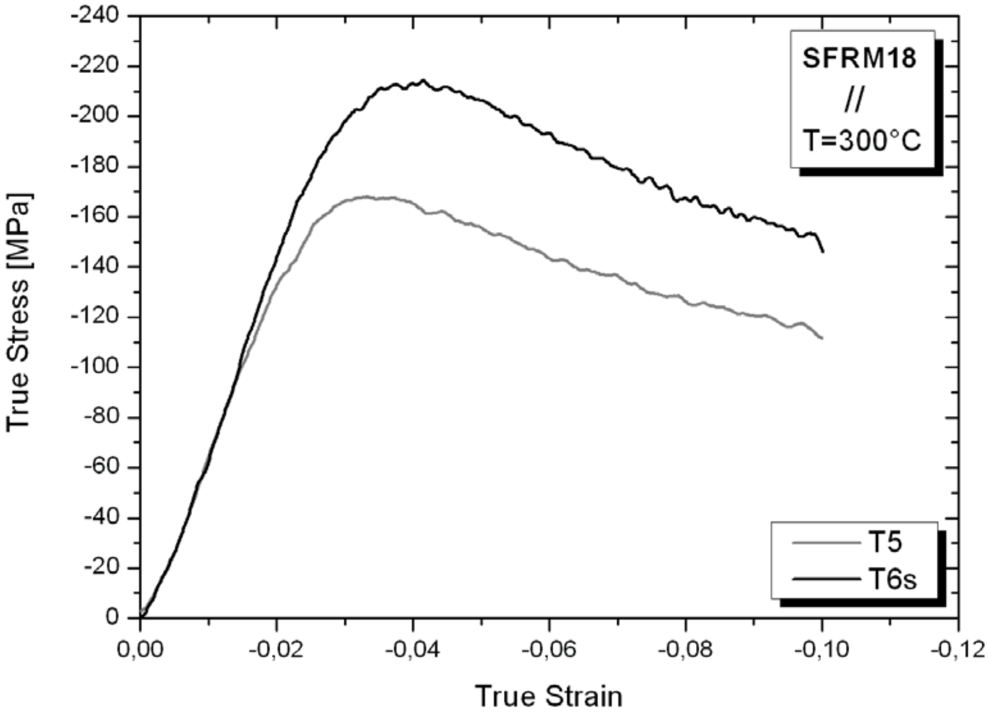

**Figure 5.50.** True Stress vs. True Strain in SFRM18 composite oriented parallel to fibre plane after dimensional stabilization.

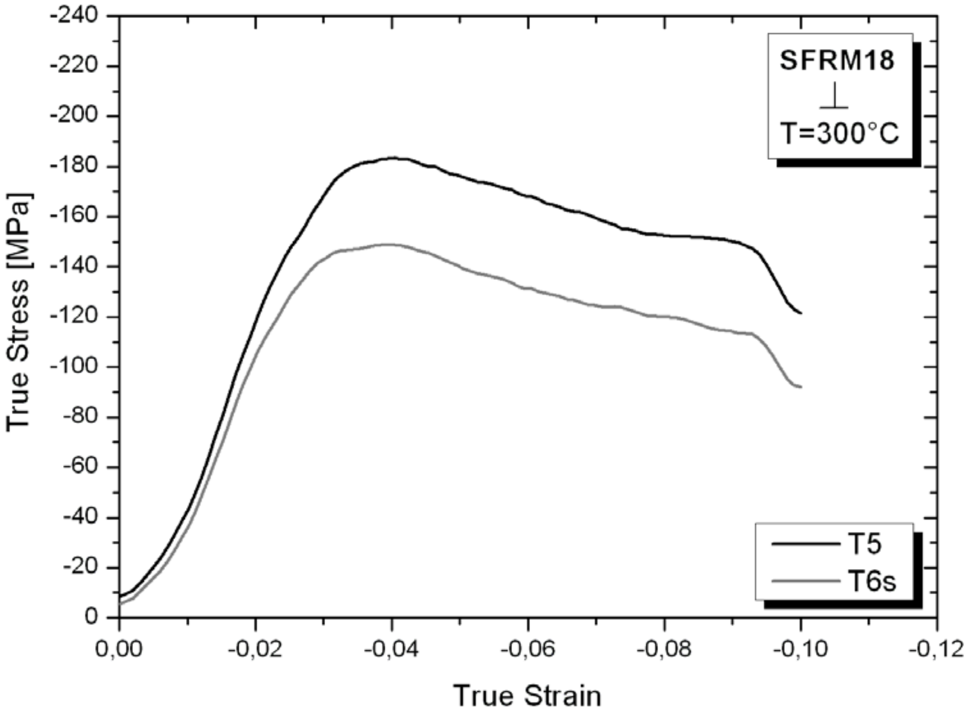

**Figure 5.51.** True Stress vs. True Strain in SFRM18 composite oriented perpendicular to fibre plane after dimensional stabilization.

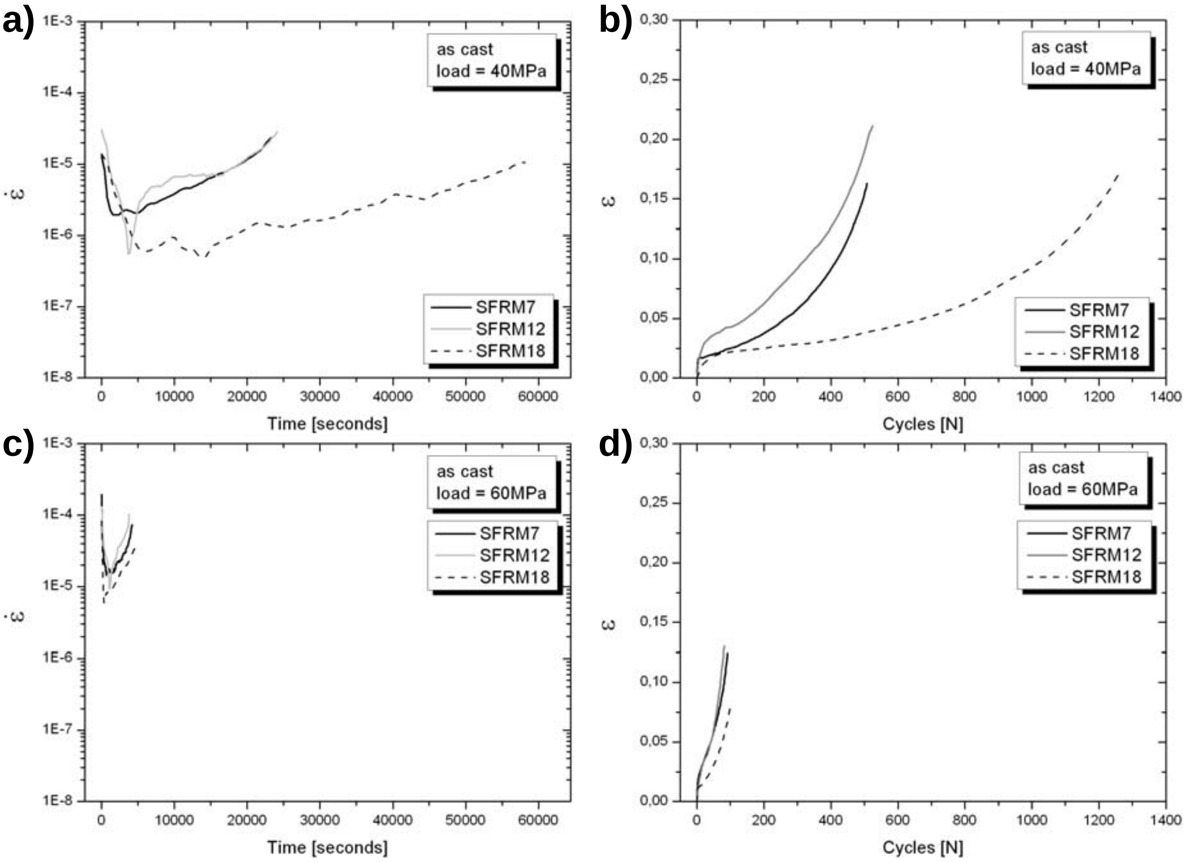

**Figure 5.52.** True strain and strain rate during thermal cycling tests of the different SFRMs in as-cast under a,b) 40MPa and c,d) 60MPa.

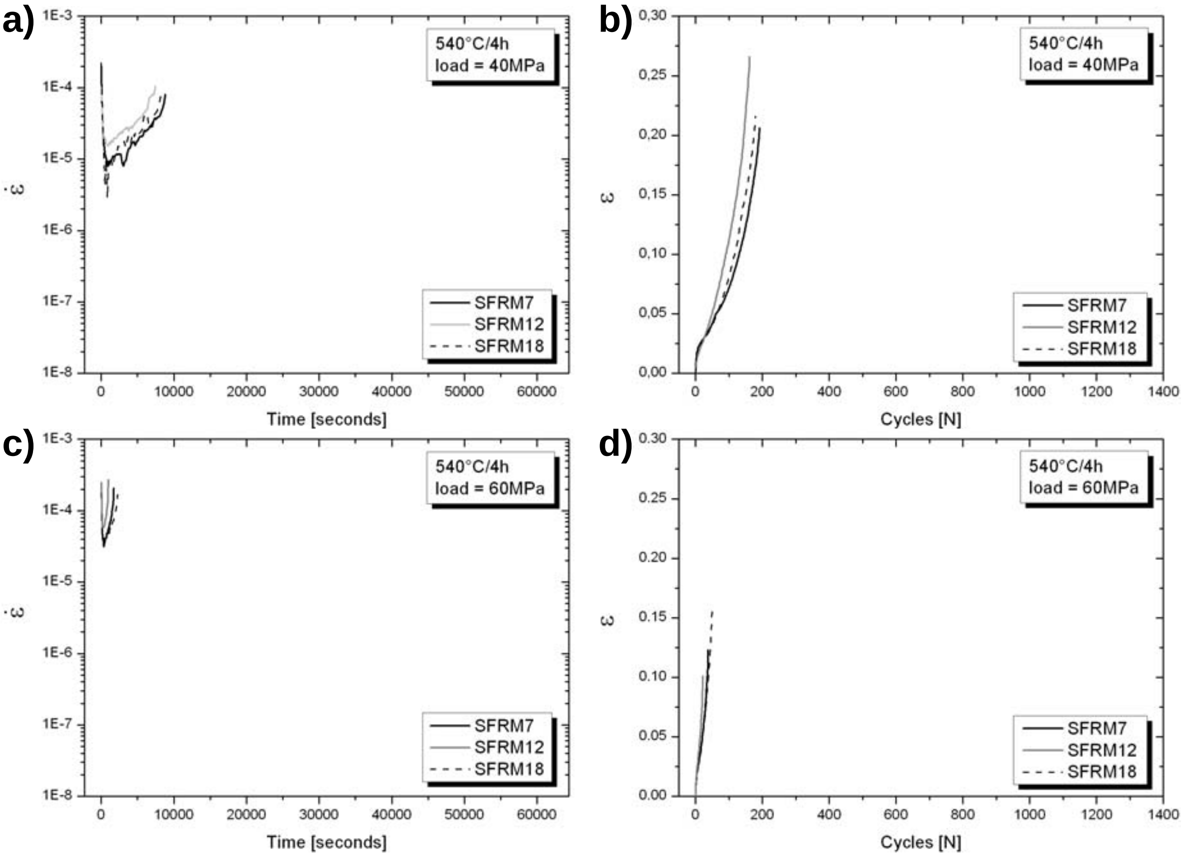

**Figure 5.53.** True strain and strain rate during thermal cycling tests of the different SFRMs after solution treatment (540°C/4h) under a,b) 40MPa and c,d) 60MPa.

# Chapter 6
# Discussion of Results

## 6.1 Influence of Si content and short fibre reinforcement on the thermal expansion

Figure 6.1a shows the thermal expansion of the different AlSi alloys, pure-Al and AlSi7/$Al_2O_3$/20s composite material after slow cooling at 1K/min from solution treatment temperature (T4c). All these are reversible for dilatometric cycles at 3K/min without remaining change in the specimens' length. The alloys expand more or less linearly, but at a lower rate with increasing Si content due to the lower CTE of Si (Si: 2.5–4ppm/K, Al: 23-34ppm/K between 25-530°C [Shackelford, 1994]). The thermal expansion of AlSi1.1 T4c is close to that of pure Al. The addition of 12 wt.% Si reduces the linear expansion of Al from RT to 500°C by 0.2% following Schapery/ROM.

The percent length change of short fibre reinforced AlSi7 samples in both parallel and perpendicular directions are equal from room temperature up to 180°C. The addition of 20%vol. of alumina fibres decreases considerably the CTE of the unreinforced alloys by ~30% in this temperature range. For higher temperatures, the reinforcement orientation plays an important role on the CTE of the composite materials: while the planar CTE is strongly reduced, the transverse CTE increases sharply with the temperature (by a factor of 2) and becomes even larger than that of the unreinforced alloys. When the matrix flows plastically, the contraction along the planar fibre direction is accompanied by a transverse expansion due to the incompressibility of the matrix [Nassini, 2001]. As long as the volume-averaged internal stresses within the matrix remained in the elastic range, the overall thermal strains of composites varied almost linearly with temperature when the CTE complies with the thermoelastic models of Schapery. When the plastic yielding of matrix begins, the PLC-temperature curves deviate from linearity due to the contribution of the matrix plastic deformation to the overall thermal strain.

Like in AlSi7/$Al_2O_3$/20s, the percent length change of parallel and perpendicular fibre orientation samples seems to be equal up to a certain temperature which increases with the Si content (110, 130, 140 and 180°C for AlSi1.1/$Al_2O_3$/20s, AlSi7/$Al_2O_3$/20s, AlSi12/$Al_2O_3$/20s and AlSi18/$Al_2O_3$/20s, respectively). The addition of Si may increase the connectivity between the alumina fibres, and furthermore that between the random fibre planes.

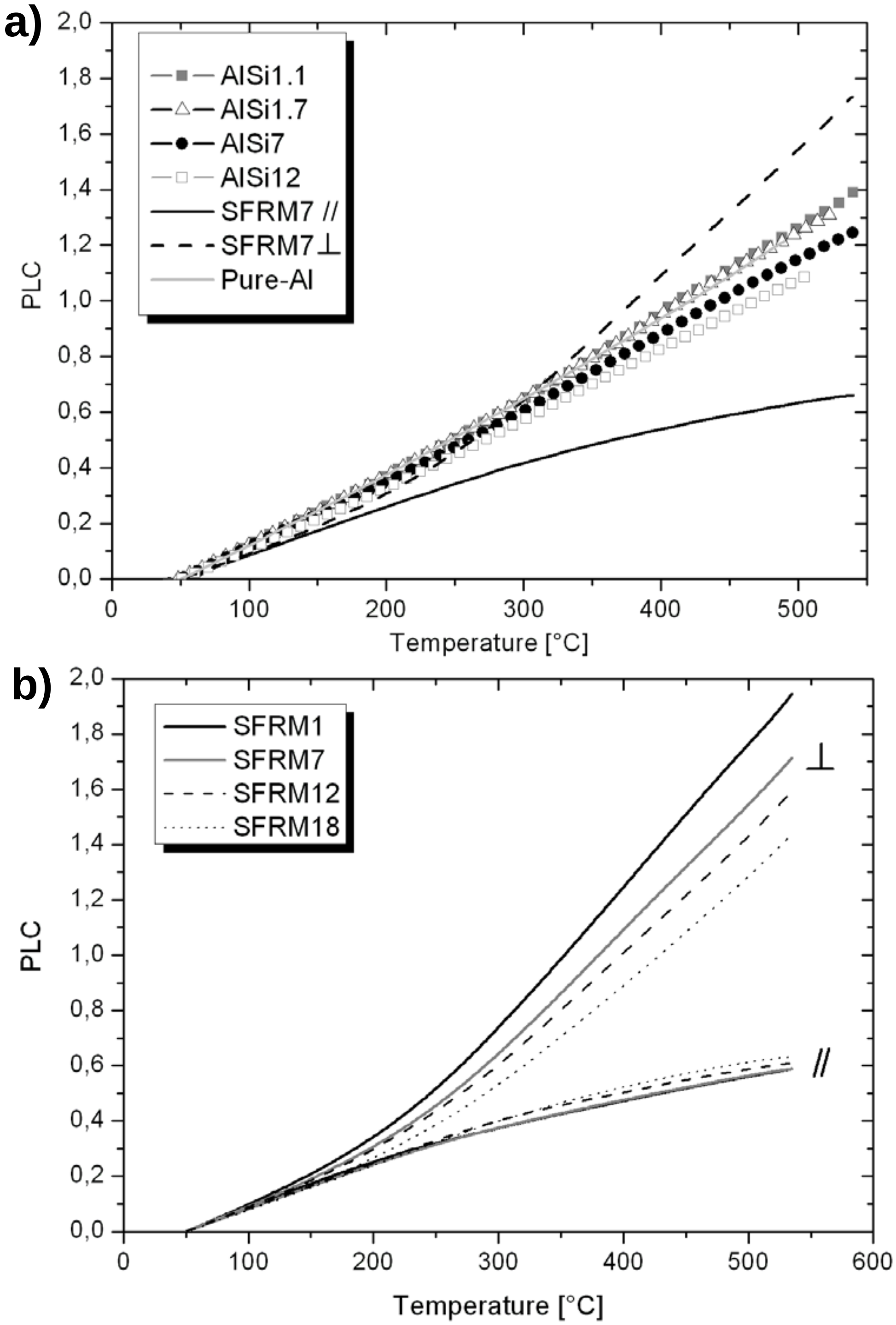

**Figure 6.1.** Influence of a) Si content on the thermal expansion of Al-Si alloys and of fibre orientation in AlSi7/$Al_2O_3$/20s (in plane || and transverse ⊥) after slow cooling (T4c=1K/min)

from ST temperature, b) PLC of studied composite materials in T4c in both fibre plane and perpendicular samples.

The theoretical CTE of the AlSi7/$Al_2O_3$/20s material (Figure 6.2) was calculated according to the quoted thermo-elastic models using the experimental CTE of the matrix according T4c and that of $Al_2O_3$ from [Bauccio, 1994]. The experimental in plane and transverse CTE of the SFRM follow the thermo-elastic model reasonably well up to 100°C. In this temperature range tensile stresses built up in the matrix during cooling, are relieved again during heating. The internal stresses produced by the mismatch between $Al_2O_3$-fibres and AlSi7 [Nassini, 2001] invert from tension into compression during heating somewhere around 150°C, while the yield stress of the matrix drops facilitating relaxation. The visco-plastic deformation of the matrix causes the in plane CTE to drop below the thermo-elastic models according to Schapery and Turner (the later assumes a percolating architecture of the $Al_2O_3$ phase). The CTE of the AlSi7/$Al_2O_3$/20s composite in the planar direction approaches that of alumina fibres, which is interpreted as a consequence of the percolating $Al_2O_3$-Si network. The reinforcement compresses the expanding Al matrix in the fibre plane at temperatures >150°C, which may creep into the transverse direction and into pre-existing pores. The later was observed for Al/SiC/70p composites [Huber, 2003]. Around 500°C, the CTE is given by the Saffil-Si reinforced architecture.

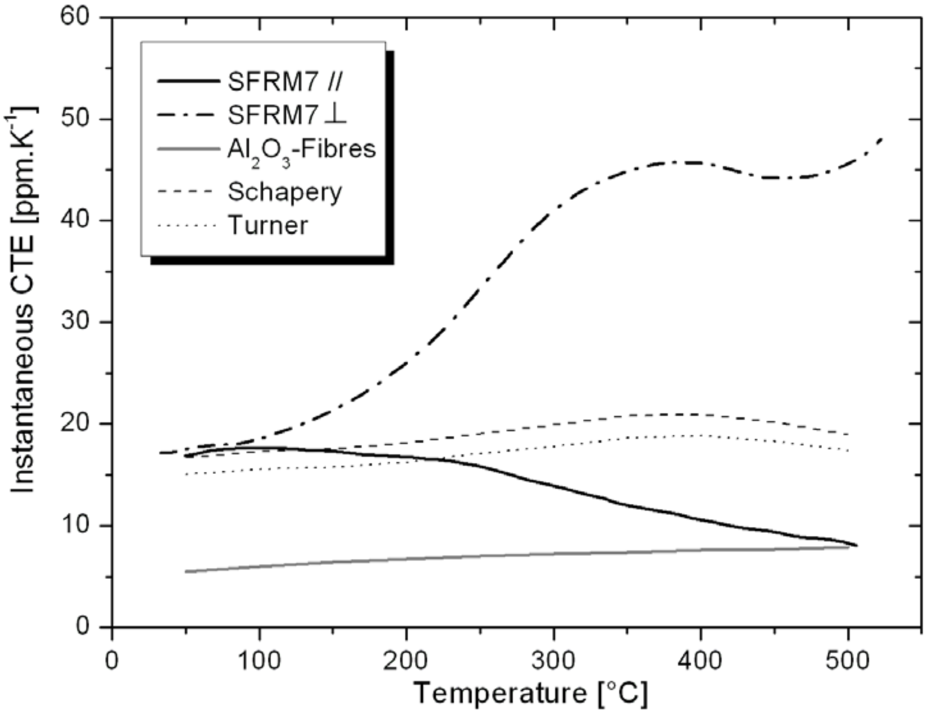

**Figure 6.2.** Instantaneous CTE of AlSi7/$Al_2O_3$/20s in fibre plane and perpendicular in the T4c condition (cooled at 1K/min from ST ) in comparison with elastic models.

## 6.2 Si precipitation in unreinforced and reinforced Al-Si-alloys

### 6.2.1 Influence on the thermal expansion of Al-Si-alloys

DSC tests performed on AlSi1.1 and AlSi1.7 are in perfect agreement with [Hälldahl, 1993; Starink, 1998].The exothermic peak observed in DSC run between 155 and 330°C for AlSi1.7 in T4 (Figure 6.3), is clearly correlated with the dramatically expansion of the alloy observed at the same temperature interval during dilatometric measurements (for both dilatometry and DSC tests performed at 3K/min). Here, the expansion of pure-Al can be taken as base line for comparison with DSC runs. TEM investigation reveals that the measured exothermic formation corresponds to the precipitation of incoherent globular Si and Si platelets, having higher atomic volume (diamond-Si) compared to that of the substitional Al-Si fcc structure.

After the observed exothermic peak, Si platelets seem to dissolve by continuous heating probably due to their higher area (but much smaller in volume than globular Si) and instability. This endothermic effect is correlated with the reduction on the CTE for re-dissolving diamond-Si precipitates into the fcc-cell.

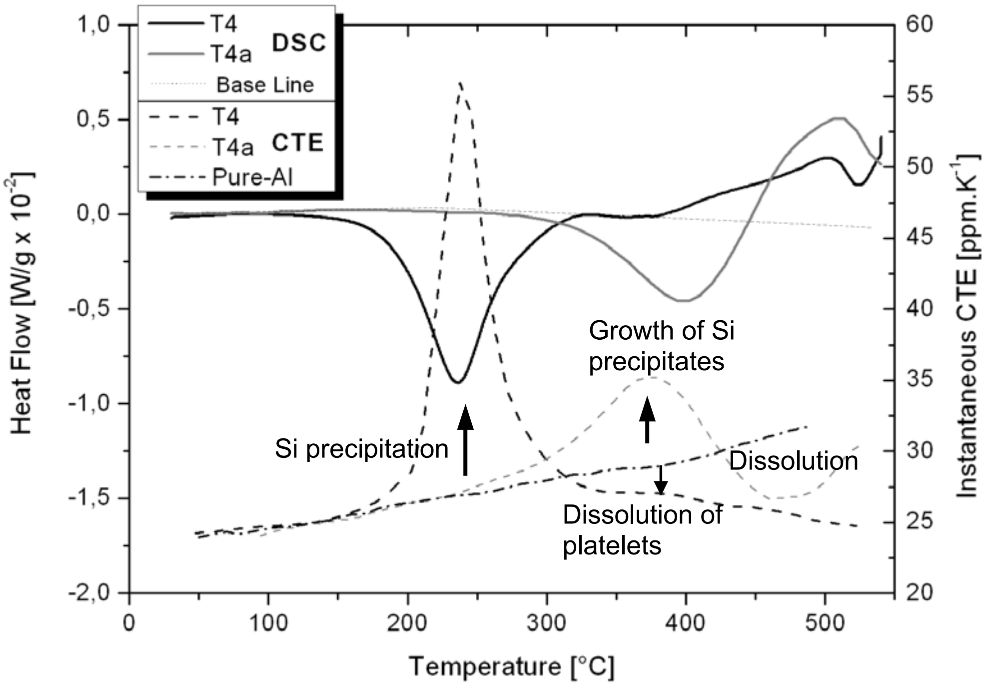

**Figure 6.3.** Instantaneous CTE and heat flow of AlSi1.7 alloy in T4 and T4a (slow cooled at 20K/min from solution treatment)

After slow cooling at 20 and 3K/min from solution treatment, the formation of Si-globular precipitates between 10-30 and 40-80nm is observed, respectively. The exothermic and endothermic effects are shifted to higher temperatures (with respect to water-quenched samples) by decreasing the cooling rate from ST. TEM investigations of AlSi1.7 samples in T4a and heated to the end of the exothermic peak, depict the formation of Si-globular precipitates in a higher concentration than before. After that, the dissolution of these precipitates is observed in both DSC runs and TEM images. Like in the alloy in T4, both exothermic and endothermic effects are in perfect agreement with the calculated expansion and reduction of the CTE, observed at the same temperature interval.

The exothermic and endothermic peaks are displaced to higher temperatures by decreasing the cooling rate from solution treatment for both AlSi1.1 and AlSi1.7 alloys. This difference is more noticeable between water quenched samples and slow cooled ones (300-1K/min). The exothermic energies (i.e. for DSC runs in AlSi1.1 samples measured at 20K/min) decreases with decreasing the cooling rate from solution treatment due to less precipitation of Si (Table 6.1). On the other hand the endothermic energies of slowly cooled samples (300, 20, 5K/min) do not show a high influence of the cooling rate and seems to be related to the dissolution of mostly globular Si precipitates. Contrarily to that, an important difference on the endothermic energies measured during DSC runs of water quenched AlSi1.1 is observed amounting a factor of ~1.8 compared to that of the T4e, T4a and T4d conditions, which is probably due to the additional dissolution of Si plates formed after heating of T4 sample which corresponds to the higher exothermic peak.

| Initial thermal condition | Exothermic Energies. [abs W/g.K] | Endothermic energies [abs W/g.K] |
|---|---|---|
| T4 | ~4.3 | ~4.7 |
| T4e (300K/min) | ~1.8 | ~2.8 |
| T4a (20K/min) | ~1.2 | ~2.6 |
| T4d (5K/min) | ~0.9 | ~2.4 |

**Table 6.1.** Calculated exothermic and endothermic energies in AlSi1.1 from calorimetric curves measured at 20K/min.

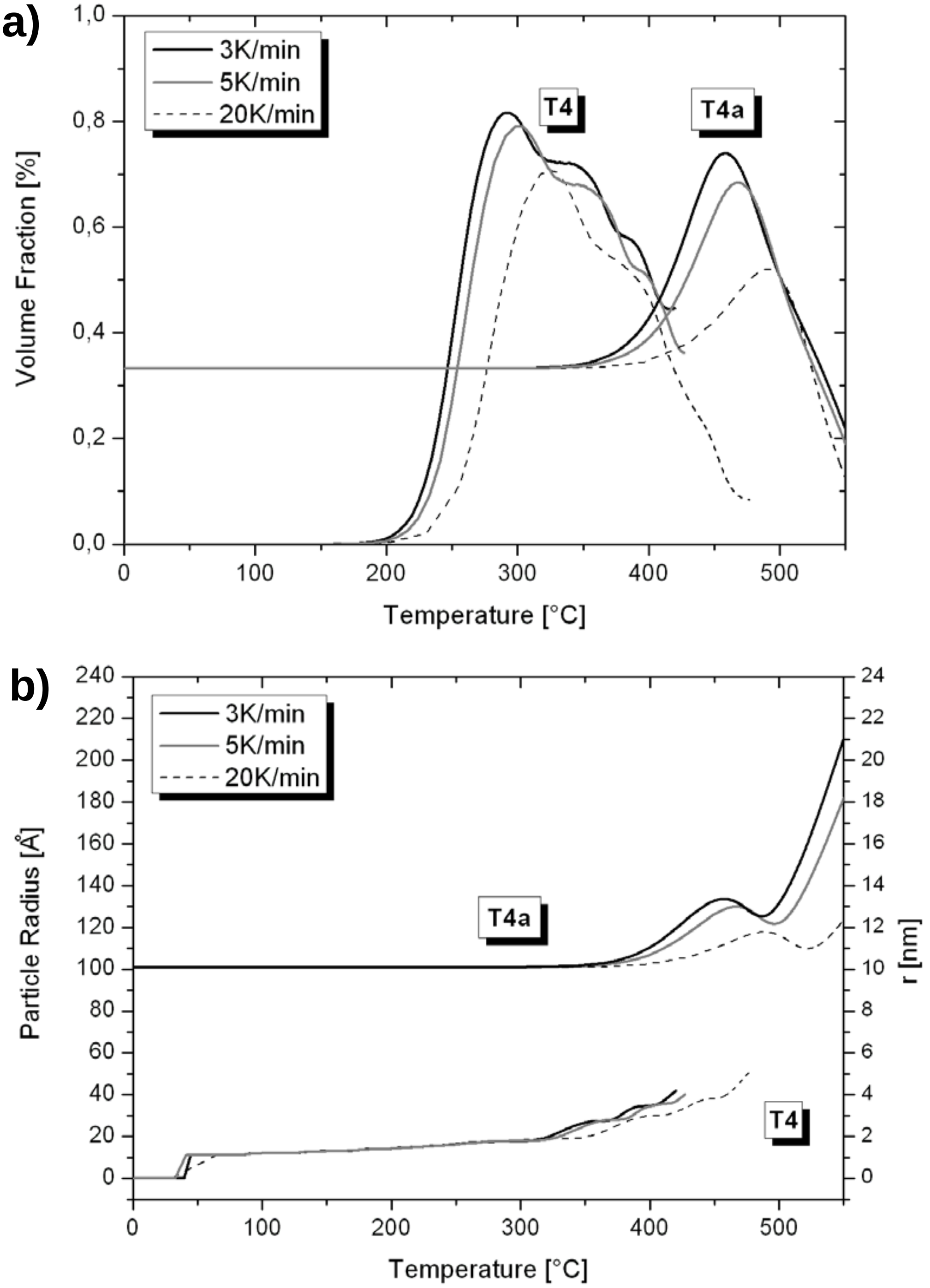

**Figure 6.4.** Modelling of the evolution of the a) volume fraction and b) mean radius of the Si-precipitates in AlSi1.1 during linear heating at 3, 5 and 20Kmin in the T4 and T4a conditions.

These observations can be explained by the modelling of the Si volume fraction and size of Si precipitates (Figure 6.4) performed in AlSi1.1 at different heating rates. The material does not show precipitates in T4; therefore nucleation should be the governing process for the precipitation of Si in water-quenched samples. The modelled volume fraction in T4 increases rapidly up to ~0.81, 0.79 and 0.71%

between ~200-293, 303 and 323°C at 3, 5 and 20K/min, respectively (Figure 6.4a). Until here, the particle radius remains between 1.4-1.8nm for all the studied heating rates. After that, continuous dissolution of Si precipitates reducing volume fraction is observed. Between 320-370°C for heating rates of 3 and 5K/min, and 360-400°C at 20K/min, growth of Si precipitates attenuates the reduction of the volume fraction. Here the radius of some coarser particles exceeds the corresponding critical radius at a defined temperature.

During modelling of the T4a condition, an initial diameter of 20nm was selected according to TEM images of AlSi1.7 samples at this thermal condition. Si precipitates coarsen at relatively higher temperatures than in T4 from 340, 360 and 383°C for samples heated at 3, 5 and 20K/min, respectively. At the same temperature interval the volume fraction increases up to 0.74, 0.68 and 0.52%, respectively. After that, a dramatic reduction of the volume fraction is observed up to the end of the tested temperature interval. Since at higher temperatures the volume fraction of Si precipitates exhibits a relatively low value, the corresponding modelled particle radius represents the value of a few particles in the alloy.

According to this explanation, the main conclusion is that the difference in temperature of the peaks observed during calorimetric tests is due to size effects as well as the reduction of the driving force produced by the less supersaturated Si in T4a-e samples. Supersaturation of vacancies in the T4 condition may also increase the diffusivity of Si with respect to slowly cooled conditions. It is important to note that the model calculates the average radius of precipitates from a calculated distribution. Therefore, the in-plane size of Si platelets does not correspond with the measured radius of Si platelets observed by TEM.

By means of metallographic observation the average volume of the globular Si precipitates ($4/3\pi r^3$) in the T6*e condition (T4+slowly heated up to 300°C + $H_2O$) is estimated at ~4316nm³ (with a distribution between 1204-9634nm³) while the calculated value of Si platelets ($\sqrt{3}/2\phi^2 t$) is only 1484nm³ (between 780-1990nm³). The calculated equivalent radius of the precipitates is estimated between 6.6-13 and 5.7-7.8 for Si globular and platelet precipitates, respectively. Therefore, the observed dissolution of Si platelets before globular ones may be correlated to the less stable state of the first ones by reaching the critical radius. The estimated critical radius at this temperature can be estimated by $r^* = (2\gamma v_{at})/(kT\ln(X/X_{eq}))$ [Nicolas, 2003] showing values of 2.1, 2.6 and 3.4nm at 270, 300 and 370°C, respectively. Although at 300°C it is observed a critical radius of only 2.6nm (obtained from the calculated parameters of the model employed in this work), this calculation shows to be sensible to the interfacial energy $\gamma$ and the solute fraction $X$, and therefore the values can vary considerably.

The later dissolution of the Si precipitates in slowly cooled samples may be correlated with the more stable precipitates also at high temperature. Here the calculated critical radius increases considerably from 4.7nm at 420°C to 10.0, 15.6nm at 450 and 470°C, respectively.

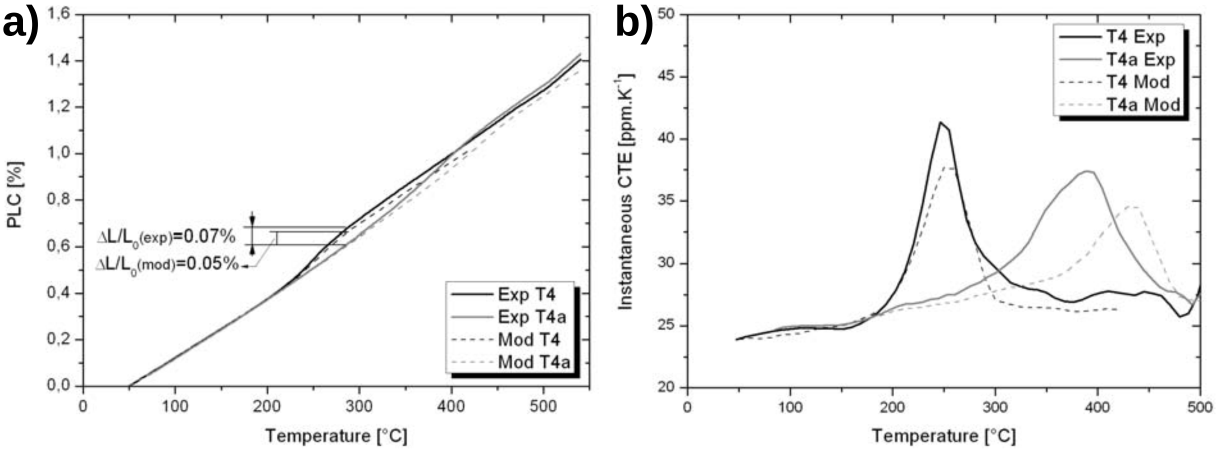

**Figure 6.5.** Modelling of a) thermal expansion and b) instantaneous CTE of AlSi1.1 in T4 and T4a conditions in comparison with experimental data.

The effect of the Si precipitation and dissolution is correlated with the thermal expansion of all the studied Al-Si-alloys as a function of the previous history of the sample. The instantaneous CTE of AlSi1.1 and AlSi1.7 seems to be sensible to cooling rate from 540°C to RT during solution treatment for all T4, T4a, T4b conditions, showing precipitation peaks followed by the reduction of the CTE due to Si dissolution. On the other hand, samples in T4c condition present only reduction of the CTE at high temperature (>420°C). The last observation is confirmed by DSC runs of samples at this thermal condition were no exothermic effects were observed.

In case of the AlSi1.1 alloy, the expansion of samples in all studied thermal conditions is increased from about 460°C, where the CTE increases up to pure-Al values at 540°C. This behaviour is not observed for alloys containing more than

1.7wt.% of Si (which is approximately the solubility limit of Si at the eutectic temperature). This difference can be attributed to continuous dissolution of the Si inclusions and precipitates in AlSi>1.2 alloys (solubility of Si at 540°C = 1.2vol.%), while they are completely dissolved in the AlSi1.1 alloy at about 490-500°C.

Figure 6.5a depicts the modelled and experimental instantaneous thermal expansion (see 3.2.3) of AlSi1.1 in both T4 and T4a conditions. The model predicts an additional expansion of the alloy of about 0.05% (~30 lower than in the experimental PLC) in T5, which agrees in temperature with the measured one. This result can also be observed by the instantaneous CTE, observing both CTE peaks at about 250°C in modelled and experimental curves (Figure 6.5b). The modelled thermal expansion of the alloy in T4a shows somewhat different from the experimental one. Here, the PLC increases more slowly with increasing temperature. The modelled CTE presents a maximum of about 34.5ppm.$K^-1$ at about 433°C, while experimental data shows a CTE peak about 9% higher at a lower temperature (389°C).

By increasing the Si content, no differences between the instantaneous CTE of the samples in T4b and T4c; and T4a, T4b and T4c are observed in AlSi7 and AlSi12, respectively. Therefore, Si precipitation should take place during cooling of the alloy and could be activated by the larger Si inclusions.

Isothermal calorimetry of AlSi1.1 and AlSi12, both in the T4 condition (540°C/4h,30min, respectively) reveals that even at low temperatures (like 175°C), the kinetic of Si precipitation is still relatively fast. In fact a minimum can be observed in the AlSi1.1 specimen at about 1 hour. Moreover no minimum peak can be observed on the AlSi12-specimen, supporting the idea that nucleation is inhibited in this alloy due to the existence of large Si-particles even after solution treatment.

### 6.2.2 Influence on the hardness of Al-Si-alloys

Although the Al-Si alloys are not considered as an age-hardneable system, the precipitation of Si changes considerably the hardness of the AlSi1.7 alloy. The formation of small Si platelets enhanced the hardness of the tested AlSi1.7 alloy after heating of the alloy at 3K/min up to 300°C (40% higher than in T4). Also, relatively high levels of hardness (~16% compared to T4) are also found after artificial “aging” at 200°C during 10hours (T6b) provoked by the precipitation of small globular Si precipitates. On the other hand, the hardness of the alloy after 300°C/1h (T6a) becomes similar to that in the T4 condition after dissolution of the Si platelets and coarsening of globular precipitates. The precipitation of the platelets morphologies on the {111} glide planes yields strengthening, the globular don't.

### 6.2.3 Influence on the thermal expansion of SFRMs

All studied composite materials exhibit a CTE peak in T4 condition in the fibre plane as well as transverse at a temperature interval between 200-350°C, which is related with the precipitation of Si. Generally, the instantaneous CTE of composites increases with decreasing cooling rate from solution treatment temperature in samples with perpendicular fibre orientation, while the opposite behaviour is observed in parallel orientation ones.

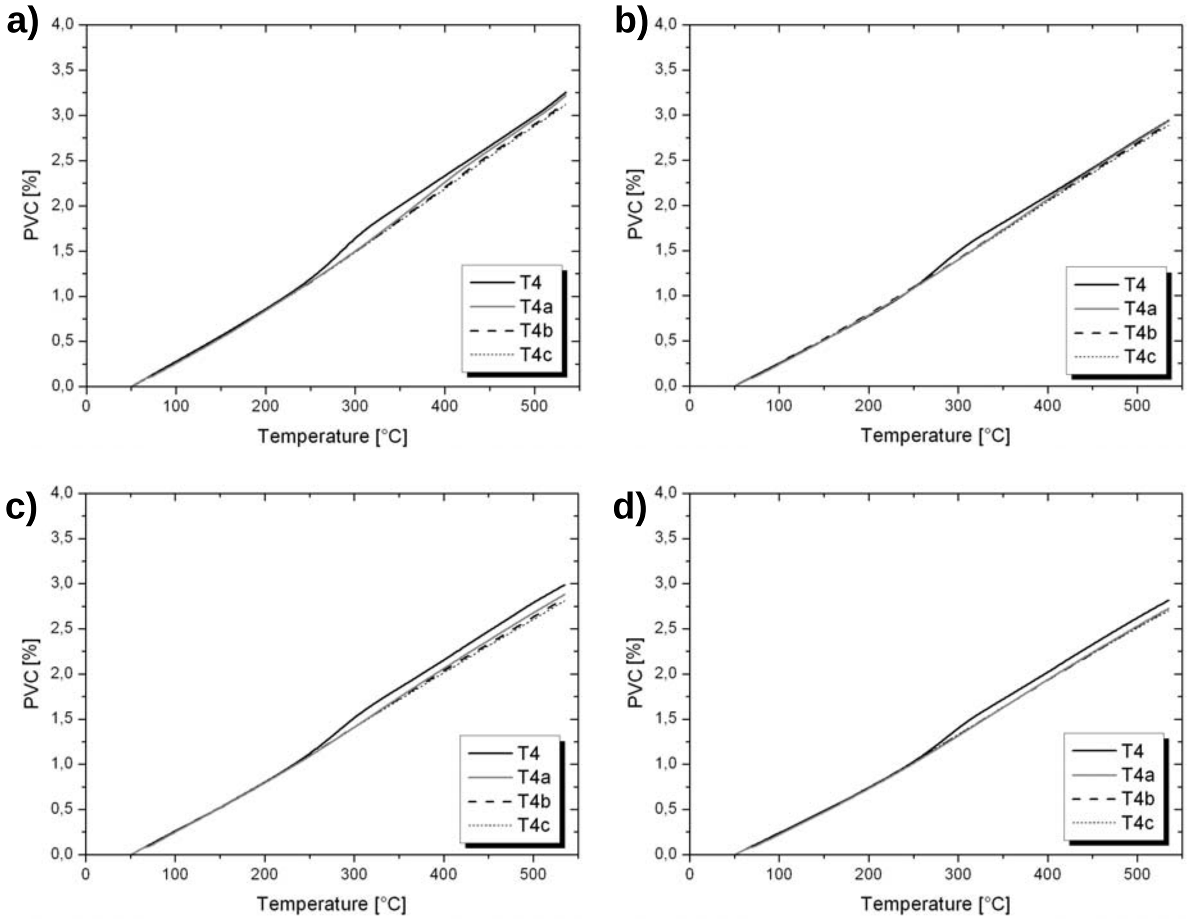

**Figure6.6.** Calculated percent-volume change in a) SFRM1, b) SFRM7, c) SFRM12 and d) SFRM18 after different cooling rates from ST.

A better understanding of the effect of Si precipitation and dissolution can be performed by the calculation of the percent volume change (PVC) of the composites by means of the addition of both thermal expansions in planar and transverse directions as: $PVC = PLC_{//} + 2PLC_{\perp}$. Furthermore, the derivative of the estimated volume change is comparable (in shape) to that of the instantaneous CTE.

The calculated volume percent change of composites in T4 (Figure 6.6) shows similar (in shape) to that of the PLC curves of the unreinforced alloys. The percent volume change of the AlSi1.1/$Al_2O_3$/20s composite material expands about 0.22% between 220 and 340°C, equivalent to a length change of 0.073% ($\alpha=\beta/3$ [Touloukian, 1975]) of an isotropic material. This value is comparable to that observed for its unreinforced alloy. Similar trends are observed for AlSi7-12-18/$Al_2O_3$/20s composites materials, amounting a little bit smaller PVC expansion of ~0.20% due the precipitation of Si.

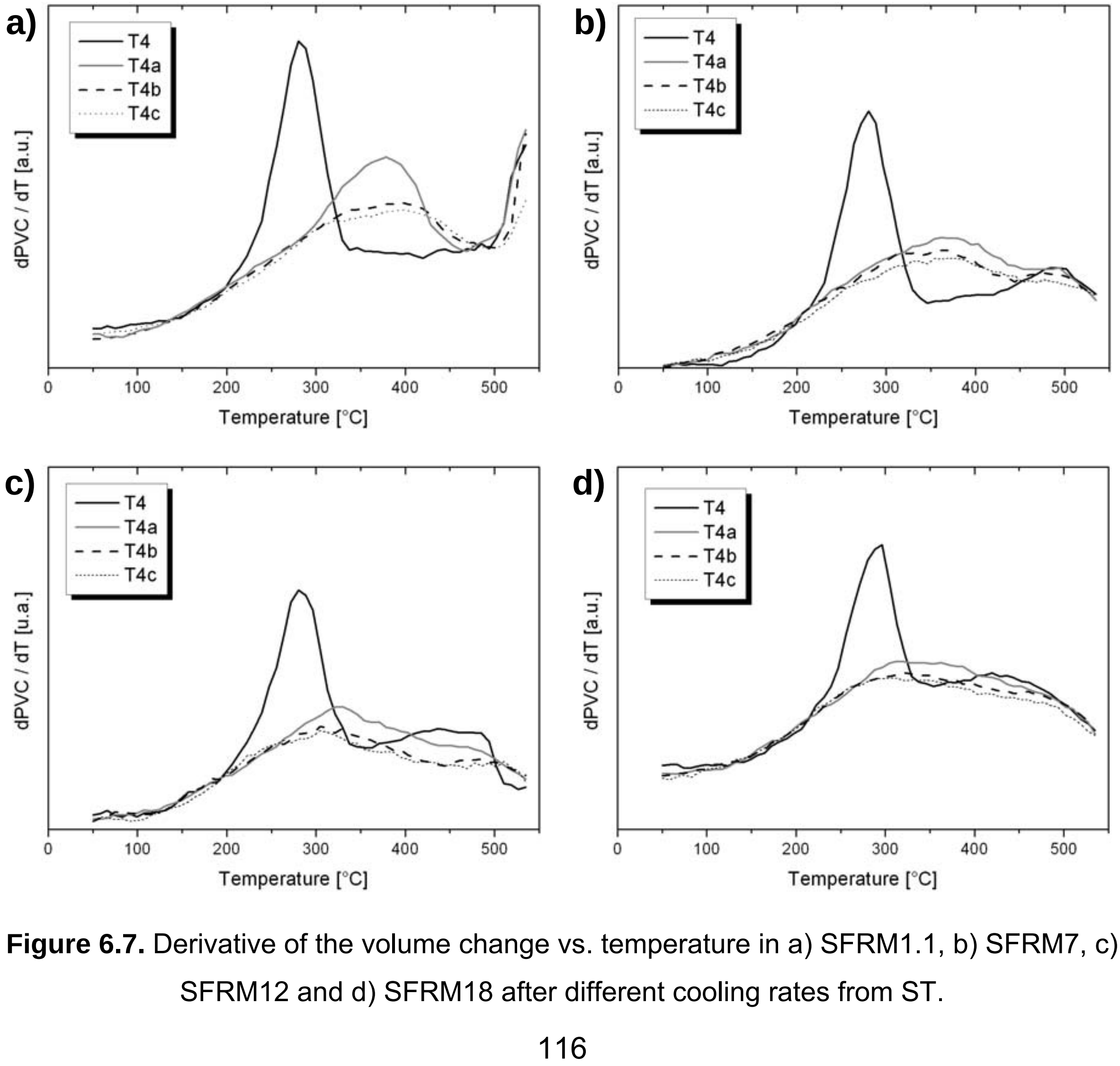

**Figure 6.7.** Derivative of the volume change vs. temperature in a) SFRM1.1, b) SFRM7, c) SFRM12 and d) SFRM18 after different cooling rates from ST.

The derivative of volume change curves is depicted in Figure 6.7. Calculations for the AlSi1.1/$Al_2O_3$/20s composite show similar to that of the instantaneous CTE of the unreinforced alloy, where an expansion peak is observed in the T4 and T4a conditions. The last one, is observed between 290 and 410°C. Contrarily to AlSi1.1, the composite material does not exhibit any expansion peak in the T4b condition where the introduction of 20%vol. of $Al_2O_3$ may produce easier diffusion paths for the precipitation of Si during cooling from ST. From 310°C in T4 and 410°C in T4a,b,c conditions, the PVC decreases due to the dissolution of Si. Comparable to the unreinforced alloy, the volume change of the composite increases from 500°C up to the end of the measured interval when approaching the temperature of the solubility limit of 1.1%Si. The derivative of samples of AlSi7-12-18/$Al_2O_3$/20s composites materials in the T4a, T4b and T4c conditions do not show any precipitation peak, indicating that precipitation of Si takes place during cooling after solution treatment.

## 6.3 Influence of the eutectic structure on the rigidity of SFRMs

The elastic modulus of the unreinforced AlSi alloys is increased about 25-28% by the addition of 20%vol. of $Al_2O_3$-fibres (in the fibre orientation plane). An important role of the Si content and its microstructure on the mechanical properties of composites materials is observed. For most of the composite materials, higher values (2-6%) of the Young's modulus in the as-cast condition compared with that of the solution treated samples are observed. Both as cast and solution treated conditions present augmentation of the elastic modulus with increasing the Si content (Figure 6.9). The unreinforced alloys present a reduction of ~2-3% in the E modulus after solution treatment for AlSi7 and AlSi12 alloys.

This behaviour can be explained by means of the load transfer from the aluminium phase to the Si inclusions in both unreinforced alloys and composite materials. In as-cast, microstructural analysis of AlSi alloys with >7wt.% of Si reveals the formation of a Si skeleton formed of thin Si lamellae with relatively high aspect ratio compared to that of the spheroidizated Si particles of solution treated samples after 540°C/4h. Therefore, the load transfer to the Si phase is higher in the as-cast condition as it can be observed by means of the estimation of the E modulus of matrices using the shear lag model (Figure6.8). Since the addition of alumina fibres produces less undercooling in the composites, the microstructural parameters of the eutectic structure differ from that of the unreinforced alloys. Therefore, the modelled E modulus of the different matrices is not identical to that of the unreinforced alloys.

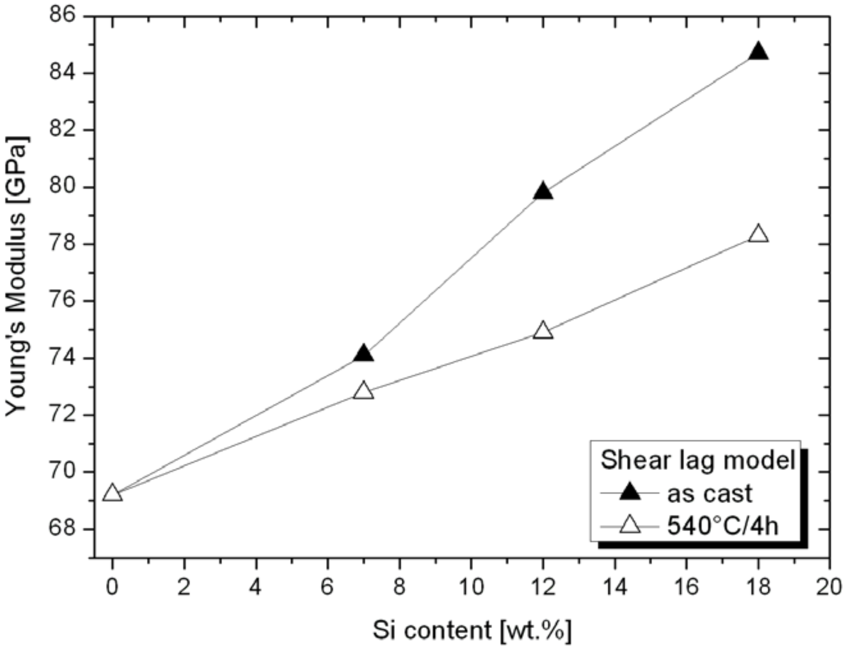

**Figure 6.8.** Modelled elastic modulus vs. Si content of AlSi1.1,7,12,18 matrices in as cast (T1) and after 540°C/4h (T4).

From this estimation, the Young's modulus of unreinforced as-cast matrices is 1.8, 6.5 and 8.2% higher than after solution treatment for the samples containing eutectic structures AlSi7, AlSi12 and AlSi18, respectively. This effect is transferred to the composite materials, were E values in as cast are observed to be about 1.3, 4.8 and 5.9% higher than solution treated samples for AlSi7/$Al_2O_3$/20s, AlSi12/$Al_2O_3$/20s and AlSi18/$Al_2O_3$/20s, respectively.

These results are in agreement with hardness measurements performed on the short fibre reinforced materials. Here, the Brinell hardness of AlSi18/$Al_2O_3$/20s decreases dramatically with solution treatment time, while that of the AlSi7/$Al_2O_3$/20s (v2) and AlSi12/$Al_2O_3$/20s composites decrease slowly. On the other hand, the solution treatment time did not play an important role on HB in AlSi1.1/$Al_2O_3$/20s since it does not contain eutectic structures.

Hardness measurements of the 1st version of AlSi7/$Al_2O_3$/20s material differ from that of the other studied composites. Here, a small hardening peak was observed after 20min of solution treatment at 540°C. The Vicker hardness of respectively deep etched samples is in agreement with the corresponding HB values of the composite material. During SEM observation Si bridging with the alumina fibres was only observed after 20min of ST and less in as cast, which may explain the observed behaviour.

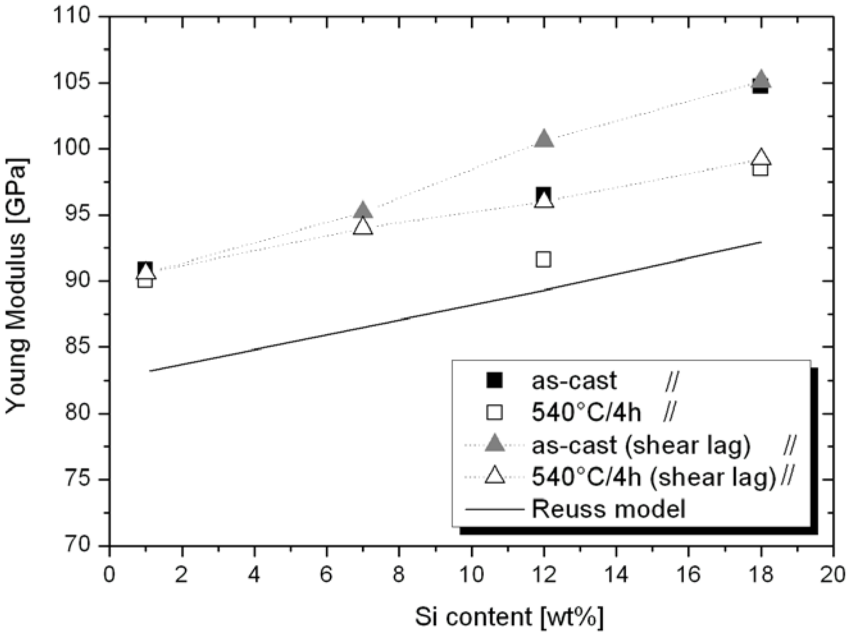

**Figure 6.9.** Modelled and experimental elastic modulus in the fibre plane vs. Si content of composite materials in as cast (T1) and after 540°C/4h (T4).

Brinnel hardness of as cast samples of AlSi7/$Al_2O_3$/20s v1 is 26% lower than its 2nd version. Contrarily to the second version, microstructural analysis of this material does not show a percolated Si-network in free fibre zones, where most of the Si inclusions are isolated in the matrix. AlSi7/$Al_2O_3$/20s v1 shows a high degree of spheroidization compared with the version 2, presenting cross section values of Si inclusions 2 times higher and shape factor 17% lower than its 2nd version. These results indicate that there was less undercooling of the eutectic during processing of the SFRM, where the ceramic reinforcement acts as heterogeneous nuclei and decreases the heat flow in the composite.

The described features explain as well the results of the compression tests performed on the composite materials. The maximal strengths achieved in the SFRMs of samples parallel and perpendicular to random fibre plane in as cast and 540°C/4h are depicted in Figure 6.10a as a function of the Si content. The $\sigma_{max}$ of composites in as cast are higher than those of ST samples for parallel and perpendicular fibre direction composites. The load transfer to the fibres is higher in samples parallel to random fibre distribution plane. Therefore, higher $\sigma_{max}$ values are observed in these samples. But this difference disappears after heat treatment confirming the role of the morphological changes of the eutectic Si.

Generally, the maximal strength of the composite increases with increasing the Si content, except for the AlSi12/$Al_2O_3$/20s material. As observed in Brinell hardness measurements, the strength of the material is lower than AlSi7/$Al_2O_3$/20s (v2) for the as cast and solution treated samples. The measured E modulus also presents a high deviation from the shear lag estimation with respect to AlSi1/$Al_2O_3$/20s and AlSi18/$Al_2O_3$/20s materials. Microstructural observation of deep etched samples shows coarser Si inclusions for AlSi18/$Al_2O_3$/20s than AlSi12/$Al_2O_3$/20s and AlSi7/$Al_2O_3$/20s (v2), respectively, but similar aspect ratio (which is the most important microstructural parameter of the reinforcement phase for the estimation of E by the shear lag model). Here, the thicker morphology and the denser distribution of the Si inclusions observed in AlSi12/$Al_2O_3$/20s (compared to AlSi7/$Al_2O_3$/20s v2) is not considered for modelling of E modulus. It is well known that refinement of the Si eutectics improves the mechanical properties of Al-Si-alloys [Haque, 1995; Kori, 2000]. Therefore, the thinner eutectic observed in AlSi7/$Al_2O_3$/20s (v2) could be responsible for increasing the Young's modulus and $\sigma_{max}$ of the composite compared to that of the AlSi12/$Al_2O_3$/20s composite, as well as observed defects in the infiltrated preform. In case AlSi18/$Al_2O_3$/20s, the role of big primary Si particles surrounding up to 10 $Al_2O_3$-fibres may produce an effect on the strength of the alumina-preform by connecting the Si fibres. This effect is also not contemplated by the model.

In all studied materials, the $\sigma_{max}$ values were registered at about 4% of true strain, where the strength starts to decrease. Since the reduction of the strength for all composites starts approximately at the same value, the corresponding effect should be related with the breakage of the reinforcement network. The softening rate of short fibre reinforced materials increases with increasing the Si content (Figure 6.10b), except in AlSi7/$Al_2O_3$/20s. The last one exhibits a softening comparable to that of AlSi18/$Al_2O_3$/20s. As cast samples parallel and perpendicular to fibre distribution plane present maximum values of softening slope, respectively, while solution treatment decreases the fragility of the reinforcement. A linear fit of the slope vs. Si wt.%-content was performed on AC and T4 samples of AlSi1/$Al_2O_3$/20s, AlSi12/$Al_2O_3$/20s and AlSi18/$Al_2O_3$/20s with parallel and perpendicular alignment to fibre random plane.

The softening in AlSi1.1/$Al_2O_3$/20s is produced by the fracture of the alumina fibres while in AlSi7-12-18/$Al_2O_3$/20s composites, the brittle Si phase plays an important role on the fracture propagation. The highest softening was achieved in the hypereutectic AlSi18-alloy reinforced with 20vol.% of $Al_2O_3$-fibres in as cast. Here, the coarse primary Si particles leads to adverse ductility and toughness [Valer Goñi, 1995; Flemings, 1991; Chiang, 2006] together with the breakage of the eutectic Si-$Al_2O_3$-network [Xian-qing, 2001]. The as cast AlSi7-12/$Al_2O_3$/20s composites present mostly an interconnected Si skeleton together with the alumina fibres. Therefore, crack propagation in the material occurs in the brittle network achieving higher softening than in AlSi1.1/$Al_2O_3$/20s. After solution treatment, spheroidization of Si reduces the softening slope of materials (because of the rounded particles [Lados, 2004]) and by the disintegration of the Si network.

The same treatment explained for samples parallel to the fibre distribution plane can be followed for perpendicular ones. Here, the softening slope is smaller but the relationship *softening slope/*$\sigma_{max}$ is comparable for both fibre distribution samples.

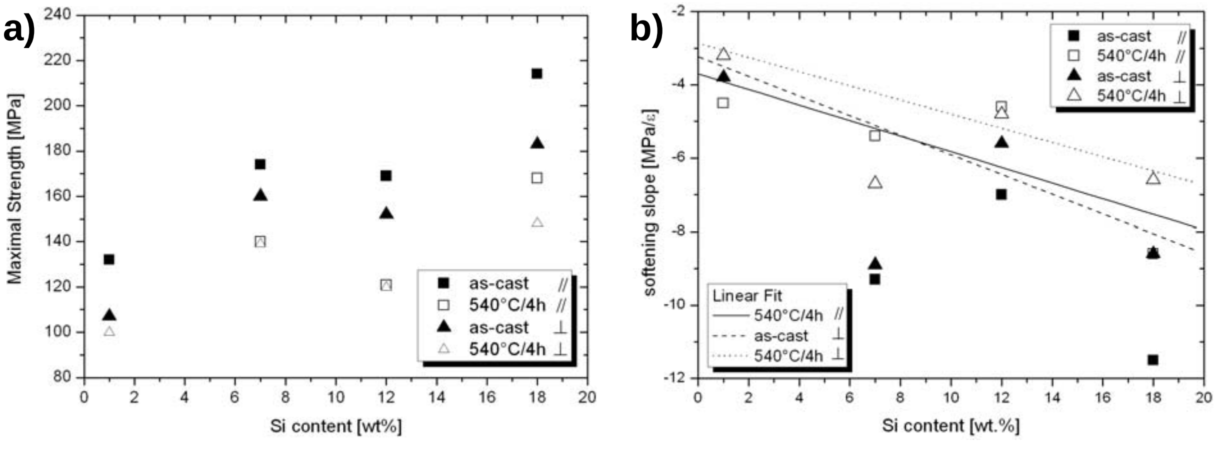

**Figure 6.10.** a) Maximal Strength and b) softening slope obtained from compression tests in AlSi1.1-7-12-18/$Al_2O_3$/20s composite materials in AC and 540°C/4h.

During thermal cycling, the thermal expansion mismatch produces large internal stresses in the composites materials upon a change in temperature. The temperature change ΔT of 250K is sufficient to bring the matrix beyond the yield point. The amplitude of variation of the thermal stresses in the composite matrix can be roughly approximated by $\Delta\sigma_M = E_M.\Delta\alpha.\Delta T$ (= 70GPa.20x$10^{-6}$$K^{-1}$.250K) = 350MPa, where $\Delta\alpha$ is the difference between the instantaneous CTE of matrix and alumina fibres. Furthermore, the applied stress has to be added producing a thermally activated plastic strain per thermal cycle [Daehn, 1988; Lasagni 2003].

The addition of 18wt.% of Si to the matrix increases the service life of the composite materials to a factor of 2 compared with AlSi7,12 matrices (in as cast). After solution treatment, the ductility of the studied composite materials is increased about 35-30%, at expenses of decreasing their service life by a factor of 3 for SFRM7, SFRM12 and 7 for SFRM18 at 40MPa. The same behaviour is observed at a test load of 60MPa, where the reduction in the service life is about 3-4 times.

The average minimal strain rate (calculated from thermal cycles) vs. the applied load in the composites AlSi7-12-18/$Al_2O_3$/20s is depicted in Figure 6.11. The lowest minimal creep rates are observed for AlSi18/$Al_2O_3$/20s and increase with decreasing the Si content (in as cast). The strain rate in the composite can be expressed by a simple power creep law expression, $\dot{\varepsilon} = k.\sigma_A^n$, obtaining high *n* values for AlSi12/$Al_2O_3$/20s and AlSi18/$Al_2O_3$/20s (7 and 6.3, respectively), while that of the AlSi7/$Al_2O_3$/20s (4.7) is 33 and 25% lower than SFRM12 and SFRM18, respectively. The minimal strain rate is noticeably increased in solution treated samples but yielding lower *n* values (between 3-5.2), which indicates a higher load carrying capacity of the Si fibre network in the as cast condition than after spheroidization. Figure 6.11 serves to indicatechanges in the high temperature behaviour, but the experimental data are not sufficient for an evaluation with respect to plasticity or creep mechanisms.

According to [Schnabl, 2003] n=6 would be expected but with smaller $\dot{\varepsilon}_{\min}$ (~$10^{-8}$s-$^1$). The results for the as cast condition indicate that the load transfer between the matrix and the reinforcement changes between the load levels.

The morphology of the eutectic Si forming an hybrid reinforcing network with the alumina-fibres does affect the mechanical properties. The Si lamellar bridges in the as cast condition of the SFRM are compared with the spheroidized morphologies in the solution treated conditions:

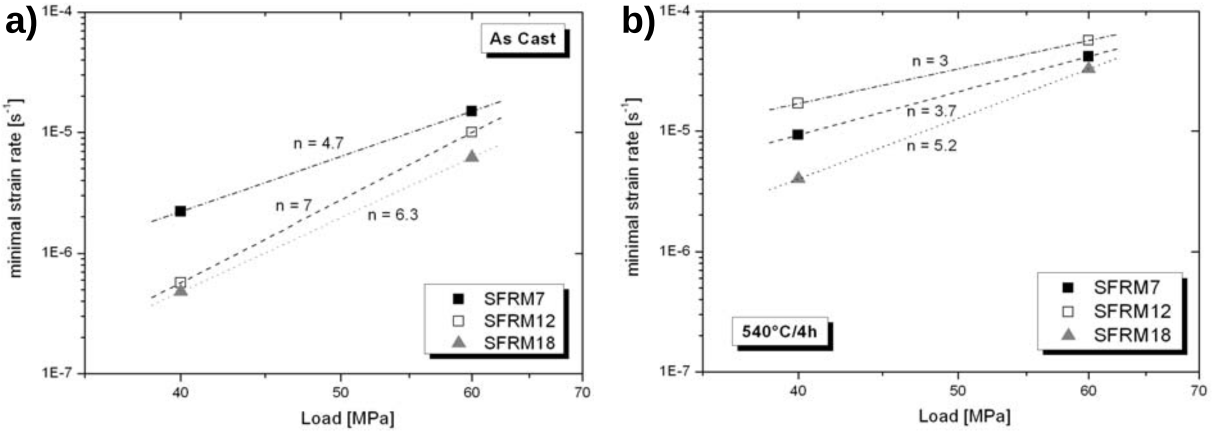

**Figure 6.11.** Experimental data for the minimal strain rate vs. applied stress (cycled between 50 and 300°C) in AlSi7-12-18/$Al_2O_3$/20s composites in: a) AC and b) after solution treatment.

| Property | Material | As cast | | 540°C/4h | | Δ | |
|---|---|---|---|---|---|---|---|
| | | // | ⊥ | // | ⊥ | // | ⊥ |
| E (25/300°C) [GPa] | SFRM1 | 91/80 | - | 91/80 | - | 0/0 | - |
| | SFRM12 | 97/82 | - | 93/80 | - | 5/2 | - |
| | SFRM18 | 106/91 | - | 99/85 | - | 7/6 | - |
| $\dot{\varepsilon}$ (40MPa) [s$^{-1}$] | SFRM7 | 2.0x10$^{-6}$ | - | 9.3x10$^{-6}$ | - | -7.3 x10$^{-6}$ | - |
| | SFRM12 | 5.7x10$^{-7}$ | - | 1.7x10$^{-5}$ | - | -1.6 x10$^{-5}$ | - |
| | SFRM18 | 4.8x10$^{-7}$ | - | 4.0x10$^{-6}$ | - | -3.5 x10$^{-6}$ | - |
| $\dot{\varepsilon}$ (60MPa) [s$^{-1}$] | SFRM7 | 1.5x10$^{-5}$ | - | 4.2x10$^{-5}$ | - | -2.7 x10$^{-5}$ | - |
| | SFRM12 | 1.0x10$^{-5}$ | - | 5.7x10$^{-5}$ | - | -4.7 x10$^{-5}$ | - |
| | SFRM18 | 6.2x10$^{-6}$ | - | 3.3x10$^{-5}$ | - | -2.7 x10$^{-5}$ | - |
| $\sigma_{0,2}$ (300°C) [MPa] | SFRM1 | 110 | 91 | - | 88 | - | 3 |
| | SFRM7 | 150 | 136 | 125 | 119 | 25 | 17 |
| | SFRM12 | 140 | 117 | 105 | 87 | 35 | 30 |
| | SFRM18 | 195 | 152 | 156 | 130 | 39 | 22 |
| $\sigma_{max}$ (300°C) [MPa] | SFRM1 | 132 | 107 | - | 100 | - | 7 |
| | SFRM7 | 174 | 160 | 140 | 139 | 34 | 21 |
| | SFRM12 | 169 | 152 | 121 | 120 | 48 | 32 |
| | SFRM18 | 214 | 183 | 168 | 148 | 46 | 35 |

**Table 6.2.** Summarized information of mechanical properties of studied composite materials

# Chapter 7
# Conclusions

## 7.1 Precipitation of Si

Fast quenching of Al-Si alloys causes Si-supersaturation. A following slow heating causes an additional linear expansion (compared with pure Al) of about 0.07-0.1%, i.e. 0.2 – 0.3 vol.%, for water quenched alloys and composite material due to Si precipitation if the Si content exceeds 1wt.%. If the Si content is less the effect is smaller, but if it is bigger it does not increase above the given values. The effect of Si precipitation can be isolated from in plane and transverse fibre distribution in SFRM by the estimation of the volume change of the composites and furthermore by its derivative (comparable in shape with the instantaneous CTE).

The precipitation peak observed in both, CTE and DSC curves, moves from 250°C in T4 to 420°C for alloys slowly cooled from solution treatment. In agreement with modelling of precipitated volume fraction performed in AlSi1.1, the retardation of Si precipitation is mainly due to nucleation effects for the slower cooled conditions. Precipitation starts during cooling. The driving force for precipitation during reheating is reduced (less concentration of Si in solid-solution) as well as diffusivity with respect to the T4 condition, where supersaturation of Si and vacancies exists. As a consequence, the expansion of the materials due to Si-precipitation decreases after slow cooling (1-20K/min) from solution treatment temperature, compared to the water quenched condition.

By increasing the Si content above maximal solubility, the expansion is further reduced due to the presence of eutectic Si by ~0.3ppm/wt.%Si around 100°C. The eutectic Si inhibits homogeneous nucleation of precipitates in the $\alpha$-phase of slowly cooled samples. Similarly as the fibres in the reinforced alloys. Saffil short fibres reduce the thermal expansion mostly in the plane of fiber orientation by ~0.35ppm/vol.% isotropically at RT, but increasingly anisotropic with increasing temperature. Above 300°C the in plane CTE approaches that of the reinforcement (6ppm.K$^{-1}$), while the transverse CTE remains constant at a level (35-54ppm.K$^{-1}$) of almost twice of that of the unreiforced matrix. While the matrix is in compression during heating, the reduced expansion along the planar direction is accompanied by a increased transverse expansion to conserve the volume of the matrix by creep effects.

The degree of Si in solid solution will affect the shape stability of any alloy or composite components. An example is presented in Figure 7.1, where the percent length change of water quenched AlSi7 alloy is depicted (heating and cooling rate: 3K/min). During cycling of the alloy the residual expansion is increased up to a maximum of ~0.1% in the 4th cycle (Figure 7.1a). On the other hand, if the alloy is heated during 2h at 300°C, no residual expansion is observed between cycles 2 and 6 (Figure 7.1b) achieving shape stabilization of faster cooled samples.

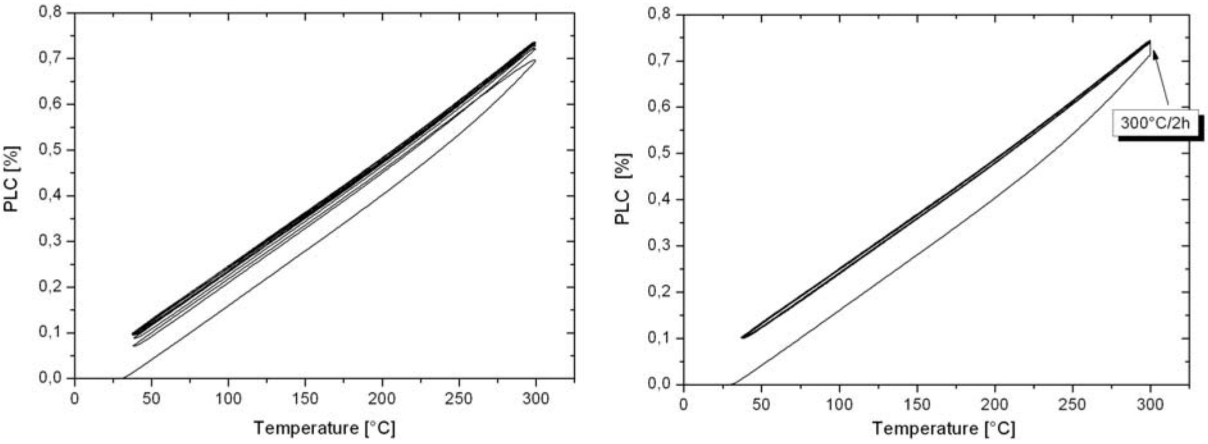

**Figure 7.1.** Thermal expansion of AlSi7 in T4 during a) continuous cycling and b) aged at 300°C/2h after heating of 1st cycle.

The formation of small Si platelets enhances the hardness of AlSi1.1 alloy to approximately 40% higher than in the solution treated condition. This effect disappears by the dissolution of the Si platelets and the formation and coarsening of globular Si precipitates during heating above 250°C. Stabilization at 200°C/2h would conserve the precipitation strengthening.

## 7.2 Influence of Si microstructure on AlSi-alloys and SFRMs

Fast solidification (after pressure die casting or squeeze casting) of AlSi-alloys with >7wt.% Si content produces a three-dimensional eutectic network. The 3D-representation and deep etched images of the studied unmodified AlSi-alloys present a lamellar Si morphology with interconnecting nodes. In case of AlSi7 alloy, regions with almost orthogonally orientated Si plates were observed. The addition of 170ppm

Sr produced full modification of the eutectic Si-structure into a fibrous morphology. The observed Si fibres seem to be mostly interconnected near the grain boundaries. The thickness of Si fibres and branches also increases towards the grain boundaries. During a short exposure to the solution treatment temperature, the Si-network is disintegrated by spheroidization and coarsening of Si particles with solution treatment time.

For the unmodified alloys and composite material, Si particles coarsen according to a $t^{\beta}$ law, with $\beta$=0.2–0.3. The initial coarsening rate is increased by the addition of Sr, (A ~ $t^{\beta}$, $\beta$~ 0.5) up to the maximum testing time of 4h due to the much finer dispersed Si structure in the as cast condition compared with coarser Si lamellae, in the unmodified alloys. The 107mm diameter casting of the AlSi7/$Al_2O_3$/20s composite material exhibits a coarser and more spheroidized structure than the faster solidified 20mm thich plate. This is due to the less undercooling of the thicker sample during solidification. Therefore, higher hardness values are observed in the cast plates of composite with a finer eutectic structure. The highest interconnectivity is found in the as cast state and depends on the cooling rate during casting.

The combination of $Al_2O_3$ short fibres and Al-Si alloys with more than 7wt.% Si results in the formation of a three-dimensional Si/$Al_2O_3$ structure. Higher values of the elastic modulus and maximum strength in as-cast are observed compared to that of the solution treated samples, where Si spheroidization affects the rigidity of the Si/$Al_2O_3$ structure by disintegrating the interconnection between the Si in the fibre free zones. In as cast, the load transfer to the Si phase is improved by, both, the percolating Si structure and the higher aspect ratio of inclusions. During solution treatment, the Si-network is disintegrated by spheroidization and coarsening of Si particles decreasing the mechanical properties of both unreinforced and reinforced alloys. The slower solidified SFRM does not show a clear softening, but the hardness level is 20% lower. In case of the AlSi18/$Al_2O_3$/20s composite material, the relatively big primary Si inclusions also increase the strength of the Si network and composite material by connecting several alumina fibres.

In all studied composites, maximum strength values are observed at about 4% of true strain during compression tests, indicating the beginning of fragmentation of the alumina fibres bellow the critical length. The $\sigma_{max}$ values of the composites increase with the Si content up to a factor of ~1.6 (between AlSi1/$Al_2O_3$/20s and

$AlSi18/Al_2O_3/20s$) for both as cast and solution treated samples. The softening of the SFRM at strains bigger than 4% is related to the Si content and morphology, presenting higher softening rates with strain for higher Si content, and as cast compared with solution treated samples.

During thermal cycling, the load transfer to the fibres is increasing with increasing temperature. The cooling produces high internal stresses in the composites due to the mismatch between their constituents, causing strain hardening between each cycle until fracture of the fibres. The composites in as cast condition present higher resistance to thermal cycling creep than solution treated samples. The reduction of the Si content decreases the number of cycles to failure and increases the minimal strain rate of the materials.

## References

[Ad. Comp. Mat., 1991] *Advanced Composite Materials*, Ed. By Navy Environmental Center, Virginia, 1991.

[Al association, 1990] *American National Standard Alloy and Temper Designation Systems for Aluminum*, Aluminum Association, Washington D.C., 1990.

[Alcan, 2003] http://www.alcan.com

[Anderson, 1962] R.G. Anderson, J.F.W. Bishop, *The Effect of Neutron Irradiation and Thermal Cycling on permanent deformations in Uranium under load*, in Symp. on Uranium and Graphite, London, Inst. of metals, pp. 17-23.

[Ashby, 1980] M. Ashby, D. R. H. Jones, *Engineering Materials 1 – An Introduction to their Properties and Applications*, Ed. by Pergamon international library: international series on materials science and technology, 1980.

[ASTM, 1995] *American Society for Testing and Materials 1995*, ASTM E, 1995, pp. 228-95.

[ASTM, 1999] *American Society for Testing and Materials 1999*, ASTM E, 1999, pp. 289-99

[Barron, 1998] T. H. K. Barron, *Cindas Data Series on Material Properties, Volume I-4 - Thermal Expansion of Solids*, Ed. by R. E. Taylor (Materials Park, OH: ASM International) Cha. 1, 1998.

[Bauccio, 1994] *ASM Engineered Materials Reference Book*, Second Edition, Michael Bauccio, Ed. ASM International, Materials Park, OH, 1994.

[Bekheet, 2002] N. E. Bekheet, R. M. Gadelrab, M. F. Salah, A. N. Abd El-Azim, Materials & Design, 23, 2, 2002, pp. 153-159.

[Birchall, 1988] J. Birchall, D. Stanley, M. Mockford, G. Pigott, P. Pinto, Journal of Materials Science Letters, 7, 1988, 350-352.

[Carreño-Morelli, 1998] E. Carreño-Morelli, T. Cutard, R. Schaller, C. Bonjour, Materials Science and Engineering A, 251, 1998, pp. 48-57.

[Chawla, 1987] K.K. Chawla, *Composite Materials – Science and Engineering*, Springer-Verlag, New York, 1987, pp. 189-191.

[Chiang, 2006] C.-H. Chiang, Chi Y.A. Tsao, Materials Science and Engineering, 2006, pp. 90-98.

[Clyne, 1993] T. Clyne, P. Whithers, *An introduction to Metal Matrix Composites*, Cambridge Solid State Science series, Cambridge, Cambridge University Press, 1993.

[Cox, 1953] H.L. Cox, Brit. Journal of Applyied Physics 3, 1953, pp. 73-79.

[Daehn, 1988] G.S. Daehn, T. Oyama, Acta Metallurgica, 22, 1988, pp. 1097-1102.

[Daehn, 1989] G.S. Daehn, G. González-Doncel, Metallic Transactions, 20A, 1989, pp. 2355-2368.

[Dahle, 2005] A.K. Dahle, K. Nogita, S.D. McDonald, C. Dinnis, L. Lu, Materials Science and Engineering A, 413-414 , 2005, pp. 243-248.

[Davis, 1993] *Aluminum and Aluminum Alloys*, ASM Speciality Handbook, Edited by J.R. Davis, Davis & Associates, 1993

[Degischer, 1997] Degischer H.P., Materials & Design, 18, 1997, pp. 221-226.

[Degischer, 1998] H.P. Degischer, P. Prader, H. Kilian, Defekte in Stranggepresstem, teilchenverstärktem Aluminium und die Streuung der Eigenschaften, DVM-Bericht 518 Bauteilversagen durch mikrodefekte, 1998, pp. 135-140.

[Derby, 1991] B. Derby, *Thermal Cycling of Metal Matrix Composites*, in Metal Matrix Composites – Processing Microstructure and Properties; 12th Risø Int. Symp., Risø, N.Hasen, D.J. Jensen, T.Leffers, H. Lilholt, T. Lorentzen, A.S. Pedersen, O.B. Pedersen, B. Ralph (eds.), Risø Nat. Lab., Dennmark, 1991, pp. 31-50.

[Deschamps, 1998] A. Deschamps, Y. Brécht, Materials Science and Engineering A, 251, 1998, pp. 200-207.

[DMA, 2000] DMA 2980™, *Operator's Manual*, TA Instruments, New Castle, DE, 2000.

[Dow, 1963] N.F. Dow, *Study of Stresses near Discontinuity in a Filament - Reinforced Composite Metal*, GE Co., Missile and Space Div., R635D61, 1963.

[Dudek, 1992] H. Dudek, R. Leucht, *Titanium Matrix Composites, in Advanced Aerospace Materials*, Ed. By H. Buhl, Springer Verlag, Berlin, 1992, 124-139.

[Edwards, 1998] G. A. Edwards, K. Stiller, G. L. Dunlop, M. J. Couper, Acta Materialia, 46-11, 1998, pp. 3893-3904.

[Elomari, 1995] S. Elomari, R. Boukhili, M.D. Skibo, J. Basounave, Journal of Material Science, 30, 1995, pp. 3037 – 3044.

[Elomari, 1997] S. Elomari, R. Boukhili, C. San Marchi, A. Mortensen, D.J. Lloyd, Journal of Material Science, 32, 1997, pp. 2131 - 2140.

[Falahati, 2001] A. Fahlahati, Kurzfaserverstärrkung für Schnellarbeitsstahl, PhD thesis, Vienna University of Technology, 2001.

[Flemings, 1991] M.C. Flemings, Metallic Transactions, 22A, 1991, pp.957-962.

[Furness, 1991] J.A.G. Furness, T.W. Clyne, *Thermal Cycling Creep of Short Fibre MMCs – Measurement and Modelling of the Strain Cycle*, in Metal Matrix Composites – Processing Microstructure and Properties; 12th Risø Int. Symp., Risø, N.Hasen, D.J. Jensen, T.Leffers, H. Lilholt, T. Lorentzen, A.S. Pedersen, O.B. Pedersen, B. Ralph (eds.), Risø Nat. Lab., Dennmark, 1991, pp. 349-354.

[García-Hinojosa, 2003] J.A. García-Hinojosa, C.R. González, G.M. González, Y. Houbaert, Journal of Materials Processing Technology 143-144, 2003, pp. 306–310.

[Giannuzzi, 2005] L. A. Giannuzzi, F. A. Stevie, *Introduction to Focused Ion Beams*, Ed. Springer, 2005.

[GKSS, 2000] http://www.gkss.de/

[Gomiero, 1994] P. Gomiero, A. Reeves, A. Pierre, F. Bley, F. Livet, H. Vichery. In: Proceedings of the 4th Conference in Aluminium Alloys: Their Physical and Mechanical Properties, Atlanta, GA, USA, 1, 1994, pp. 644-651.

[Hahn, 1991] T.A. Hahn, in *Metal Matrix Composites: Mechanisms and Properties* (Ed.: R.K. Everett, R.J. Arsenault), Academic Press, Boston, 1991, pp. 329 – 332.

[Hälldahl, 1993] L. Hälldahl. Thermochimica Acta, 214, 1993, pp. 33-40.

[Han, 1999] B. Han, S. Agnew, D. Dunad, Scripta Materialia, 40 ,1999, pp. 801-808.

[Haque, 1995] M.M. Haque, Journal of Materials Processing Technology, 55, 1995, pp. 193-198.

[Hashin, 1963] Z. Hashin, S. Shtrikman, Journal of Mechanics Physic Solids, 11, 1963, pp. 127 – 140.

[Hassel, 1991] R.L. Hassel, American Laboratory, Vol 1, 1991.

[Heinrich, 1998] K.F. Heinrich, D.F. Newbury, *American Society for Metals*, Vol. 10, 9th edition, ASM International editorial, USA, 1998, pp. 517-535.

[Henning, 1994] W. Henning, G. Neite, in: Metallische Verbundwerkstoffe, ed. by K.U. Keiner, DGM Informationsgesellschaft, Frankfurt, 1994, pp. 169-191.

[Holzer, 2004] L. Holzer, f. Indutnyi, PH. Gasser, B. Münch, M. Wegmann, Journal of Microscopy, 216, 2004, pp. 84.

[Hong, 1988] S.H. Hong, O.D. Sherby, A.P. Divecha, S.D. Karmarkar, B.A. MacDonald, Journal of Composite Materials, 22, 1988, pp. 447-452.

[Huang, 2005] Y.D. Huang, N. Hort, H. Dieringa, K.U. Kainer, Y. Liu, *Interfatial reaction in the short-fiber reinforced AlSi12CuMgNi piston alloy*, in Proceeding of the 15. Symposiums Verbundwerkstoffe und Werkstoffeverbunde, Kassel, Ed. M. Schlimmer, Editorial Werkstoff-Informationsgessellschaft mbH, Frankfurt, 2005, pp. 33-38.

[Huber, 2003] T. Huber, *Thermal Expansion of Al-alloys and Composites*, PhD Thesis, TU-Vienna, 2003.

[Kaczmar, 2000] J. Kaczmar, K. Pietrzak, W. Wlosinski, Journal of Materials Processing and Technology, 106, 2000, pp. 58-67.

[Kelly, 2000] A. Kelly, C. Zweben, *Comprehensive Composite Materials*, Vol. 3, Elsevier, 2000.

[Kerner, 1956] E.H. Kerner, *Proc. Phys. Soc.*, B69, 1956, pp. 808-813.

[King, 1998] J.A. King, *Materials Handbook for Hybrid Microelectronics*, Artech House, Norwood, MA, 1988.

[Kirby, 1992] R.K. Kirby, *Compendium of Thermophysical Property Measurement Methods* vol 2, ed K D Maglic, A Cezairliyan and V E Peletsky (New York: Plenum) ch. 19, 1992, pp 549–67.

[Kori, 2000] S.A. Kori, B.S. Murty, M. Chakraborty, Materials Science and Engineering A283, 2000, pp. 94-104.

[Kostoz, 1979] G. Kostoz, *Treatise on Materials Science and Technology*, in: G. Kostoz, H. Herman (Eds.), Neutron Scattering, vol. 15, Academic Press, 1979.

[Lados, 2004] D.A. Lados, D. Apelian, Materials Science and Engineering A, 385, 2004, pp.187-199.

[Lasagni, 2003] F. Lasagni*, Caracterización, Modelado y Estudio de la Deformación Local en Compuestos de Matriz de Aluminio reforzados con Fibras Cortas y Partículas de Alúmina*, Diploma Thesis, TU-Vienna/Universidad Nacional del Comahue, 2003

[Le Flour, 1987] J.C. Le Flour, R. Locicéro, Scripta Metallurgy, 21, 1987, pp. 1071-1076.

[Makhlouf, 2001] M.M. Makhlouf, H.V. Guthy, Journal of Light Metals, 1, 2001, pp. 199-218.

[mmc-asses, 2001] http://mmc-asses.tuwien.ac.at

[Mohamed, 1998] F. Mohamed, Scripta Materialia, 38, 1998, pp. 457-463.

[Mortensen, 1993] A. Mortensen, V. Michaud, M. Flemings, Pressure Infiltration Processing of Reinforced Aluminium, JOM, 1993, pp. 36-43.

[Mori, 2006] K. Mori, S. Maki, M. Ishiguro, International Journal of Machine Tools and Manufacture, 2006.

[Nassini, 2001] H.E. Nassini, M. Moreno, C. Gonzalez Oliver, Journal of Material Science, 36, 2001, pp. 2759-2772.

[Nicolas, 2003] M. Nicolas, A. Deschamps : Acta Materialia, 51, 2003, pp. 6077-6094.

[Nolte, 1997] M. Nolte, *Entwicklung einer Gieß- und Infiltrationtechnik zur Fertigung von Aluminium-Bauteilen mit selektiver Faserversärkung*, PhD Thesis, RWTH Aachen, Düsseldorf, 1997.

[Ogris, 2002a] E. Ogris, *Development of Al-Si-Mg Alloys for Semi-Solid Processing and Silicon Spheroidization Treatment (STT) for Al-Si Cast Alloys*, PhD Thesis, Swiss Federal Institute of Technology Zurich, 2002.

[Ogris, 2002b] E. Ogris, A. Wahlen, H. Lüchinger, P.J. Uggowitzer, Journal of Light Metals 2, 4, 2002, pp. 263-269.

[Olsson, 1995] M. Olsson, A.E. Giannakopoulos, S. Suresh, J. Mech. Phys. Solids, 43-10, 1995, pp. 1639-1671.

[Outwater, 1956] J.O. Outwater, Modern Plastics 33, 1956, pp. 56-65.

[Pacz, 1921] A. Pacz, U.S. Patent 1397900, 1921.

[Pech-Canul, 2000] M. Pech-Canul, R. Katz, M. Makhlouf, Journal of Processing Technology, 108, 1, 2000, pp. 68-77.

[Pickard, 1988] S.M. Pickard, B. Derby, *Thermal Cycle Creep of Al/SiC Particulate Composite, in Mechanical and Physical Behaviour*, 9th Risø Int. Symp. on Met. and Mat. Sci., Røskilde, S.I. Andersen, H. Lilholt ,O.B. Pedersen (eds.), Risø Nat. Lab., Dennmark, 1988, pp. 447-452.

[Poletti, 2003] C. Poletti, W. Marketz, H.P. Degischer, *Hot Formability of a Particle Reinforced Ti-Alloy*, in Proceeding: 10th World Conference of Titanium –Ti 2003, Hamburg.

[Polmear, 1995] I.J. Polmear, *Light alloys: Metallurgy of Light Metals*, Edited by Whiley, Printed in Great Britain, 1995.

[Prohazka, 2001] W. Prohazka, *"Thermisches Ausdehnungsverhalten von AlSiC",* Diploma thesis, Institute of Materials Science & Testing, Vienna University of Technology, 2001.

[Rabinovitch, 1983] M. Rabinovitch, J.F. Stohr, T. Khan, H. Bibring, *Directionally Solidified Composites for Applications at High Temperatures*, in handbook of Composites, vol.4 – Fabrication of Composites, A Kelly and S.T. Mileiko (eds.), Elsevier, Amsterdam, pp. 295-372.

[Rammerstorfer, 2000] F.G. Rammerstorfer, H.J. Böhm*, Lecture Notes of Composite Engineering*, ILFB, Vienna University of Technology**,** 2000, pp. 2 – 4.

[Requena, 2004] G. Requena, *Creep Beahaviour of Discontinuosly Reinforced Aluminium Alloys*, PhD Thesis, TU Vienna, 2004.

[Requena, 2006] G. Requena, H.P Degischer, Materials Science and Engineering: A, 420, 1, 2, 2006, pp. 265-275.

[Roberts, 1956] A.C. Roberts, A.H. Cottrel, Philosophical Magazine, 1, 1956, pp.711-717.

[Robson, 2001] J.D. Robson, P.B. Prangnell, Acta Materialia, 49, 2001, pp. 599-613.

[Rosen, 1960] B.W. Rosen, *Mechanics of Fibre Strengthening*, in Fibre Composite Materials, B.W. Rosen (ed.), ASM, Metals Park, Ohio, 1960.

[Schapery, 1968] R.A. Schapery, Journal of Composite Materials, 2, 1968, pp. 380.

[Schiroky, 1997] G.H. Schiroky, D.V. Miller, M.K. Aghajananian, A.S. Fareed, Key Engineering Materials, 127-131, 1997, pp. 141-152.

[Schnabl, 2003] A. Schnabl, H.P. Degischer, Zeitschrift für Metallkunde, 94, 6, 2003, pp. 743-748.

[Shackelford, 1994] J. Shackelford, W. Alexander, J.S. Park, *CRC Materials Science and Engineering Handbook*, Boca Ratón, Florida, CRC Press Inc., 1994.

[Srivatsan, 1995] T. Srivatsan, T. Sudarshant, E. Laverniaj, Progress in Materials Science, 39, 1995, pp. 317-409.

[Smithells, 1983] C.J. Smithells, *Metals Reference Book,* 6th ed., Ed. E.A. Brandes, pub. Butterworths, ch.11 Equilibrium Diagrams, 1983, pp. 29.

[Stampfl, 1996] J. Stampfl, S. Scherer, O. Kolednik, Applied Physics A, 63, 1996, pp. 145-151.

[Starink, 1998] M.J. Starink, A.M Zahra, Philosophical Magazine A, 77, 1, 1998, pp. 187-199.

[Thermocalc, 2004] http://www.thermocalc.com

[Thall, 1950] B.M Thall, B. Chalmers, Journal of Inst. Met, 77, 79, 1950.

[TMA, 1999] TMA 2940TM, *Operator's Manual*, TA Instruments, New Castle, DE, 1999.

[Tjong, 2000] S.C. Tjong, Z.Y. Ma, Materials Science and Engineering, 29, 2000, pp. 49-113.

[Touloukian, 1975] Y.S. Touloukian, R.K. Kirby, R.E. Taylor, P.D. Desai, *Thermophysical Properties of Matter, Volume 12—Thermal Expansion,* Metallic Elements and Alloys (New York:IFI–Plenum), 1975, pp. 11a.

[Turner, 1946] P.S. Turner, J. Re. Nat. Bu. Stan., 37, 1946, pp. 239 - 250.

[Valer Goñi, 1995] J. Valer Goñi, J.M. Rodriguez-Ibabe, J.J Urcola, Scripta Materialia, 34, 3, 1996, pp. 483-489.

[Vander Voort, 1984] G.F. Vander Voort, *Metallography, principles and practice*, MacGraw Hill, 1984.

[Vidal-Sétif, 1999] M. H. Vidal-Sétif, M. Lancin, C. Marhic, R. Valle, J. -L. Raviart, J. -C. Daux and M. Rabinovitch, Materials Science and Engineering A, 272, 2, 1999, pp 321-333.

[Wagner, 1991] R Wagner, R Kampmann : *Homogeneous second phase precipitation. Materials Science and Technology : a comprehensive treatment*, Vol. 5, Ed. by Haasen, VCH, Weinheim, 1991.

[World Aluminium, 2000] http://www.world-aluminium.org

[Wu, 1984] M.Y. Wu, O.D. Sherby, Scripta Met., 18, 1984, pp. 773-776.

[Xian-qing, 2001] Xian-qing Xie, Di Zahng, Tong-xiang Fan, T. Sakata, H. Mori, Toshihiro Okabe, Takashi Hirose, Material Letters, 2002, pp. 102-107.

[Yue, 1996] T. Yue, G. Chadwick, Journal of Materials Processing Technology, 58, 1996, pp. 302-307.

[Zeren, 2005] Muzaffer Zeren, Journal of Materials Processing Technology, 169-2, 2005, pp. 292-298.

[Zhang, 2003] Qiang Zhang, Gaohui Wu, Longtao Jiang, Guoqin Chen, Materials Chemistry and Physics, 82, 3, 2003, pp. 780-785.

[Zhigang, 2002] L. Zhigang, L. Young, M. Farghalli, Materials Science and Engineering A, 332, 2002, pp. 330-342.

# Fernando A. Lasagni

## LEBENSLAUF

| | |
|---|---|
| **Persönliche Daten:** | geboren in Cinco Saltos, Argentinien<br>27. August 1977<br>Staatsangehörigkeiten: Argentinien / Italien |

**Ausbildung:**

| | |
|---|---|
| Universität:<br>03.1997 – 02.2003 | Ingenieurwissenschaftliche Fakultät der Staatlichen Comahue Universität, Provinz Neuquén, Argentinien.<br>Titel: Dipl. Chemie Ingenieur.<br>Durchschnittsnote: 8,92/10<br>Diplomarbeit: *Characterization, modelling and study of the local strain in short fibre and particle reinforced Metal Matrix Composites*. Institut für Werkstoffkunde und Materialprüfung, TU-Wien, Österreich (06.2002 11.2002). |
| Gymnasium:<br>03.1991 – 12.1996 | CEM Nr. 95 „*Armando Novelli* “ Gymnasium, Provinz Río Negro. Argentinien.<br>Durchschnittsnote: 9,23/10<br>Abschluß als Absolvent der Chemietechnikerschule. |
| Grundschule:<br>03.1984 – 12.1990 | Grundschule Nr. 39 „*Alejandrina La Mon de Mac Auliffe*“, Cinco Saltos, Provinz Río Negro. Argentinien. |

| | |
|---|---|
| **Veröffentlichungen:** | 16 Konferenzberichte und Publikationen in wissenschaftlichen Zeitschriften und Büchern. |

| | |
|---|---|
| **Autorenschutzregister:** | 3 Softwares und Marken wurden in Südamerika und den USA angemeldet. |